ROYAUME DU MAROC
Université Mohammed V - RABAT -
جامعة محمد الخامس – الرباط –
Faculté des sciences
كلية العلوم

*CENTRE D'ETUDES DOCTORALES-SCIENCES ET TECHNOLOGIES*

N° d'ordre : 3897

# THÈSE

*En vue de l'obtention du :* ***DOCTORAT***

**Structure de recherche** : Équipe des sciences de la matière et du rayonnement.

**Discipline** : Physique.

**Spécialité** : Physique quantique.

***Présentée et soutenue le 17/02/2024***
***par :***

**Hicham AIT MANSOUR**

## *Quantum Dots Meet Quantum Information And Thermodynamics*

***Devant le JURY:***

| | | |
|---|---|---|
| **Hamid EZ-ZAHRAOUY** | PES, Faculté des Sciences, Université Mohammed V - Rabat | Président |
| **Adil BELHAJ** | PH, Faculté des Sciences, Université Mohammed V - Rabat | Rapporteur/Examinateur |
| **Abdeljalil RACHADI** | PH, Faculté des Sciences, Université Mohammed V - Rabat | Rapporteur/Examinateur |
| **Mostafa MANSOUR** | PH, Faculté des sciences Aïn Chock Casablanca. | Rapporteur/Examinateur |
| **Özgür MUSTECAPLIOGLU** | Professeur, Université Koç, Istanbul | Examinateur |
| **Zakaria MZAOUALI** | PA, The Institute of Theoretical and Applied Informatics - Gliwice | Invité |
| **Mustapha FAQIR** | PES, Université Internationale- Rabat | Co-Directeur de thèse |
| **Morad EL BAZ** | PES, Faculté des Sciences, Université Mohammed V - Rabat | Directeur de thèse |

**Année universitaire : 2023/2024**

# Dedication

*Dedicated to my wonderful wife, a source of support and inspiration. Your unwavering love and encouragement have guided me through the challenges of this thesis journey.*
*To my beloved family, your support and sacrifices fueled my motivation. This achievement is a shared triumph. Thank you all for being my pillars of strength.*

Love You All ... <3 <3 <3

# Acknowledgments

The work presented in this thesis was carried out in the Matter Science and Radiation Team (ESMaR), Department of Physics, Faculty of Sciences, Mohamed V University, Rabat, Morocco.

I would like to express my gratitude to everyone who contributed to the research and completion of this thesis. First and foremost, I extend my deepest appreciation to Prof. **Morad EL BAZ**, professor at the Faculty of Sciences of Rabat, for allowing me to conduct this research under his supervision. As my thesis advisor, he supported me throughout my thesis with his patience, motivation, enthusiasm for research, and his immense knowledge. I thank him for guiding me in the right direction whenever he thought I needed it. I owe the level of my PhD degree to his encouragement and efforts. Without his guidance and clear and enlightening instructions, this thesis would not have been completed or written. One could not wish for a better and friendlier supervisor.

In addition to my advisor, I would like to thank Prof. **Mustapha FAQIR** for his insightful comments and motivation and for allowing me to join his team at the International University in Rabat.

I would like to express my thanks to Mr. **Hamid EZ-ZAHRAOUY**, Professor at the Faculty of Sciences, Mohammed V University in Rabat, for honoring me with his presence as the chairman of the dissertation defense committee for my Doctorate. Additionally, I want to extend my heartfelt gratitude to him for his kindness and benevolence towards me.

I extend my profound gratitude to Prof. **Adil BELHAJ**, Prof. **Abdeljalil RACHADI**, and Prof. **Mostafa MANSOUR** for graciously accepting the role of rapporteurs for my thesis. Their distinguished expertise, unwavering support, and meticulous evaluation have significantly enriched the scholarly content and rigor of my research. I am deeply appreciative of their invaluable contributions, which have undoubtedly enhanced the scholarly merit of this endeavor.

I would like to express my thanks to Prof. **Özgür MÜSTECAPLIOĞLU**, professor at Université Koç in Istanbul for agreeing to be members of the jury and for evaluating my work. I am deeply grateful to all members of the jury for approving the manuscript and for being part of the defense of this thesis. I am indebted to them for their valuable comments on this thesis.

I would like also to express my thanks to Prof. **Zakaria MZAOUALI**, professor at Institute of Theoretical and Applied Informatics, Polish Academy of Sciences for gracing my thesis presentation with your invaluable insights and expertise. Your presence added immense value to the discussion and greatly enriched the academic exchange

Throughout this thesis, I had the opportunity to participate in several national and international scientific events that enabled me to present my scientific research and to discuss with many experts as well as young researchers in the quantum information theory and condensed matter physics field, which has improved the quality of my thesis. Special thanks go to the International Centre for Theoretical Physics (ICTP) in Trieste, Italy, for its hospitality during the scientific visit and for its financial support. Further sincere gratitude goes to **Andreas BUCHLEITNER**, **Dariusz CHRUSCINSKI**, **Karol ZYCZKOWSKI**, and **Paweł**

**HORODECKI** for the valuable discussions that helped me to enhance my research.

I want to thank Prof. **Fatima Zahra SIYOURI**, a member of the ESMaR team, Prof. **Khadija EL ANOUZ**, **Abderahim EL ALLATI**, professors at the Faculty of Sciences and Techniques of Al Hoceima, and all professors and senior staff members of the ESMaR team for creating a great research environment in the laboratory of theoretical physics. I would also like to thank my dear colleagues for the many wonderful memories from trips and events that we attended together. In particular, my wife **Fadwa EL AYACHI**, **Zakaria MZAOUALI**, **Oumayma EL BIR**, **Sanae ABAACH**, **Youssef Khouja**, and **Khadija EL HAWARY**.

# Résumé

Dans cette thèse, nous nous concentrons sur l'étude de la dynamique des corrélations quan- tiques au sein de deux qubits excitoniques intégrés dans deux boîtes quantiques semi-conductrices InAs couplées, interagissant indépendamment avec des réservoirs de déphasage. Nous ex- plorons leur comportement dans des environnements markoviens et non markoviens en fonc- tion du temps et de la température. De plus, nous analysons les effets d'un champ électrique externe sur ces corrélations ainsi que les effets liés à l'interaction de Förster. Nous étudions aussi le comportement du discord quantique global et de l'intrication dans deux boîtes quan- tiques doubles couplées composées de AlGaAs/GaAs en fonction de la température. Nous étudions également le comportement du discord quantique global et de l'intrication dans deux boites quantiques doubles couplés composés de AlGaAs/GaAs en fonction de la température. Nous utilisons chaque pair de boites quantiques comme un qubit, où l'électron peut occuper soit la boite à droite, soit la boite à gauche. L'objectif de notre enquête est de comprendre l'impact du décalage énergétique de chaque qubit et de l'énergie de couplage tunnel sur les corrélations quantiques. Enfin, l'objectif est d'utiliser les trois boites quantiques InAs comme substance de travail d'un moteur thermique quantique, permettant au moteur de fonctionner à des échelles très réduites, en présence d'un champ électrique, et du mécanisme de Forster, qui décrit le transfert d'énergie entre les boites quantiques et affecte ainsi le comportement du moteur. À cet égard, nous étudions le comportement du travail effectué par le moteur et l'intrication dans le système lorsque le paramètre de Forster varie.

**Mots-clés**: Boites quantiques, Intrication quantique, Thermodynamique, machine thermique, Fonction de Wigner, Discorde.

# Abstract

Quantum dots are considered among the most promising techniques for implementing various quantum information processing protocols. They have properties similar to those of single atoms, even though they are actually composed of multiple atoms. Their properties and the relative ease of their fabrication and manipulation mean that they have several interesting applications, not only in the field of quantum information, but also in areas such as the construction of quantum heat engines, or the manufacturing of high-resolution screens. In this thesis, we focus our attention on investigating the dynamics of quantum correlations within two excitonic qubits embedded in two coupled semiconductor InAs quantum dots independently interacting with dephasing reservoirs. Their behavior in both Markovian and non-Markovian environments is explored against dimensionless time and temperature. Moreover, the effects of the external electric field on these correlations as well as the effects related to the Förster interaction are extensively analyzed. Also, we will study the behavior of global quantum discord and entanglement in two coupled double quantum dots made of AlGaAs/GaAs as a function of temperature. We use each double quantum dot as a qubit, where the electron can occupy either the right or left dot. The goal of our investigation is to understand the impact of the energy offset of each qubit and the tunneling coupling energy on quantum correlations. Finally, is to use the three InAs quantum dots as a working substance of a quantum heat engine, which allows the engine to operate at very small scales, in the presence of an electric field, and the Forster mechanism, which describes the transfer of energy between quantum dots and affects thus the engine's behavior. In this regard, we study the behavior of the work performed by the engine and the entanglement in the system as the Forster parameter is varied.

We deem that the study performed in this thesis does represent a major step forward in the application of quantum dots in both quantum information processing and quantum thermodynamics fields.


**Keywords**: Quantum Dots, Quantum Entanglement, Thermodynamics, Heat Engines, Wigner Function, Discord.

# Résumé Détaillé

Les boites quantiques sont considérées comme parmi les techniques les plus prometteuses pour l'implémentation des différents protocoles de traitement de l'information quantique. Les boites quantiques (Quantum dots en anglais) ont des propriétés similaires à celles des atomes uniques, sachant qu'elles sont en réalité composées de plusieurs atomes. Ses propriétés et la facilité relative de leurs fabrication et manipulation font qu'elles ont plusieurs applications intéressantes, pas seulement dans le domaine de l'information quantique, mais aussi dans des domaines comme la construction de cellules photovoltaïques, ou la fabrication d'écran à haute résolution.

Dans le domaine de l'information quantique, une des ressources les plus fondamentales est l'intrication quantique. Les boites quantiques peuvent être utilisé pour générer cette ressource de deux manières différentes. Soit, sous la forme de photons intriqués émis par la même boite quantique, ou encore sous la forme d'une intrication de spin entre différentes boites quantiques. Des résultats préliminaires ont été obtenues suivant ces deux directions de recherche, mais concerne dans la plupart des cas, la génération d'intrication bipartite.

Le but de cette thèse est de prospecter sur les différentes façons de générer de l'intrication à ordre supérieur en utilisant les boites quantiques. Ainsi le premiers objectif de cette thèse est consacrés à la génération d'une intrication quantique bipartite entre deux boites quantiques InAs, et d'étudier leur comportement dans un system ouvert, leur comportement dans des environnements à la fois Markoviens et non Markoviens est exploré en fonction du temps sans dimension et de la température. De plus, les effets du champ électrique externe sur ces corrélations, ainsi que les effets liés à l'interaction Förster, sont analysés de manière approfondie. Nous montrons que le comportement non Markoviens des corrélations quantiques est toujours préservé sous la variation du champ électrique et de l'interaction Förster, indépendamment de l'influence significative de ces deux paramètres sur la quantité de corrélations quantiques. De plus, nous démontrons que la discorde quantique non nulle peut encore être observée pour des valeurs élevées de température et de temps sans dimension, contrairement à la concurrence qui disparaît dans ce régime.

Le deuxième objectif est d'étudier le comportement de la discorde quantique globale et de l'intrication dans deux pairs de boites quantiques couplés composés d'AlGaAs/GaAs en fonction de la température. Nous utilisons chaque pair de boites quantiques comme un qubit, où l'électron peut occuper soit la boite quantique droite, soit la boite quantique gauche. L'objectif dans cette partie de notre étude est de comprendre l'impact du décalage d'énergie de chaque qubit et de l'énergie de couplage de tunnel sur les corrélations quantiques. Nos résultats montrent que le décalage d'énergie et l'énergie de couplage de tunnel affectent significativement les variations de l'intrication de formation, de la discorde standard et de la discorde quantique globale.
Les différentes applications de ces intrications seront aussi étudiées dans le cadre de cette thèse, une application de ces boites quantiques est le troisième objectif de cette these, c'est d'utiliser les trois boites quantiques InAs comme substance de travail d'un moteur thermique quantique, permettant au moteur de fonctionner à des échelles très réduites, en présence d'un champ électrique, et du mécanisme de Forster qui décrit le transfert d'énergie entre les boites quantiques et affecte ainsi le comportement du moteur. À cet égard, nous étudions le comportement du travail effectué par le moteur et l'intrication dans le système lorsque le paramètre de Forster varie.
**Mots-clés**: Boites quantiques, Intrication quantique, Thermodynamique, machine thermique, Fonction de Wigner, Discorde.

## Publications whose material appears in this thesis:

- **H. Ait Mansour**, F. Siyouri, M. Faqir, M. El Baz: Quantum correlations dynamics in two coupled semiconductor InAs quantum dots. **Physica Scripta** 95(9), 095101 (2020)
- **H. Ait Mansour**, M. Faqir, M. El Baz: Global Quantum Discord and Entanglement in two Coupled Double Quantum Dots AlGaAs/GaAs. **International Journal of Theoretical Physics** 62(3), 58 (2023).
- **H. Ait Mansour**, M. Faqir, M. El Baz: InAs three quantum dots as working substance for quantum heat engines. **arXiv preprint arXiv** 2309.10958, 2023.

## Further publications:

- F. Siyouri, **H. Ait Mansour**: Robustness of Wigner function negativity under the exciton-exciton interaction effects inside two coupled semiconductor quantum dots. **Quantum Information Processing** 20, 1-10 (2021).
- **H. Ait Mansour**, F. Siyouri: Wigner function as a detector of entanglement in open two coupled InAs semiconductor quantum dots. **International Journal of Theoretical Physics.** 61 (4), 118 (2022).
- F. Siyouri, **H. Ait Mansour**, F. El Barichi: Studying quantum correlations dynamics in the phase space for continuous-variable Werner states and Bell-diagonal states. **International Journal of Geometric Methods in Modern Physics** 16 (07), 1950109 (2019).

# List of Figures

# List of Tables

# Contents

# Introduction

In the early 20th century, the world of physics was abuzz with attempts to understand the electronic properties of materials, leading to the emergence of condensed matter physics [6, 7, 8]. Quantum mechanics [9], developed in the 1920s and 1930s, began to offer insights into how electrons moved in solids. Visionaries like Felix Bloch crafted theories to explain electron movement through atomic lattices [10], laying the foundational knowledge of solid-state materials. However, while metals and insulators were somewhat understood, there was a class of materials whose electrical properties did not fit neatly into either category which is the semiconductors. By the 1930s, it became evident that these materials had a unique conductivity, sensitive to factors like temperature, light, and impurities. The mid-20th century was a transformative period for these mysterious materials. At the renowned Bell Labs, William Shockley et al [11], John Bardeen et al [12] unearthed the potential of semiconductors. They introduced a process called "doping," where specific impurities were added to semiconductors, dramatically altering their conductive properties. This gave birth to the p-n junction, a foundational concept behind nearly all semiconductor devices [13]. Silicon (Si) soon emerged as the darling of the semiconductor world in the late 1950s and 1960s. Its abundant availability and excellent electronic properties made it the material of choice. This era also witnessed the groundbreaking invention of integrated circuits, these circuits heralded the electronic devices revolution, promising a future where multiple transistors could reside on a single silicon chip. The drive towards miniaturization became relentless. With innovations like photolithography[14], which employs light to craft intricate patterns onto silicon wafers, the size of transistors shrank dramatically. Around this time, Intel's co-founder, Gordon Moore, observed that the number of transistors on a chip would approximately double every two years, an insight that became the iconic Moore's Law [15]. However, as these structures became tinier, the quantum world began to assert its influence. By the closing decades of the 20th century, quantum effects were no longer mere curiosities but central to semiconductor design. Quantum wells, wires, and dots emerged [16], with each structure confining electrons in one, two, or three dimensions respectively.

Quantum dots (QDs) exemplify the convergence of classical semiconductor theory and quantum mechanics. These nano-sized semiconductor particles, typically ranging from 2 to 10 nanometers in diameter, have fascinated researchers due to their distinctive quantum mechanical properties. Their size and shape bestow upon them a phenomenon known as quantum confinement, in which the motion of electrons and holes is limited in all three spatial dimensions. This confinement results in the quantization of the quantum dots' energy levels, leading to discrete energy states. Due to these atom-like energy configurations, they are sometimes referred to as "artificial atoms".

The exploration of quantum dots significantly advanced in the 1980s, initiated by the discoveries of Russian physicist Alexei Ekimov in 1981[17]. He first observed quantum dots in a glass matrix, paving the way for Louis E. Brus to further the research by developing colloidal semiconductor quantum dots in the mid-1980s[18]. Both physicists, honored with the Nobel Prize in Chemistry in 2023, highlighted a unique feature of quantum dots - their optical and electronic properties could be modified by merely adjusting their size. This was a departure from bulk materials, where color traits are primarily determined by the material

itself, showcasing that in quantum dots, the color attributes are dictated by size. Adjusting the size of these particles allows for the manipulation of the color of light they emit or absorb. The field saw a substantial leap in 1993 when Moungi Bawendi, another Nobel laureate of 2023, innovated the chemical production of quantum dots[19]. His method produced nearly flawless particles, elevating the standard of quality in the field. This breakthrough in precision broadened the scope of applications for quantum dots, offering better consistency and predictability. Due to these unique properties, quantum dots have garnered immense interest across various fields. Their optical characteristics make them immensely useful in display technologies [20, 21], leading to brighter, more vibrant colors in LED displays. Beyond consumer electronics, their applications extend to solar cells, where their tunability can be harnessed for better light absorption. In the realm of biomedicine, quantum dots have shown promise as fluorescent markers for molecular imaging, providing a non-toxic alternative to traditional dyes. Furthermore, the understanding of quantum dots paves the way for exploring more complex quantum systems and phenomena. They have become foundational in the study of quantum coherence, entanglement, and other quantum behaviors at the nanoscale. These behaviors are being harnessed as we step into the era of quantum computing and quantum information processing.

Following the advancements in semiconductor technologies and the emergence of quantum structures, the late 20th century and early 21st century bore witness to another revolutionary wave — the deepening exploration of quantum physics and its practical implications[9]. As our understanding of the quantum realm evolved, it became clear that quantum mechanics wasn't just about understanding the behavior of the tiniest particles. It also held the promise of entirely new frameworks for processing and handling information. Traditional computers, built on classical physics principles, had limitations that quantum mechanics could potentially transcend. Richard Feynman, in the 1980s, was among the pioneers who recognized this potential. He proposed that a machine operating on quantum principles could simulate nature in ways classical computers never could. In parallel, David Deutsch [22], further formalized the concept of a quantum computer, which could harness the superposition principle of quantum mechanics to perform multiple calculations simultaneously.

The 1990s and early 2000s witnessed substantial theoretical advancements in the budding field of quantum information theory [23]. Among these developments, quantum entanglement stood out as both mystifying and revolutionary. This phenomenon describes a state wherein the quantum states of separate particles become so intertwined that the state of one particle instantly reflects changes made to the other, irrespective of the distance that separates them. Imagine two entangled particles placed at opposite ends of the universe; a change induced in one would instantaneously be mirrored by the other, a feat that classical physics struggles to explain. Such an instantaneous link appears to violate the principle that information cannot travel faster than the speed of light—a foundational pillar of Einstein's theory of relativity [24]. Hence, it's no surprise that Einstein, along with collaborators Podolsky and Rosen [25], expressed early skepticism of entanglement. They introduced the concept of "hidden variables" to argue that quantum mechanics might be incomplete, providing an alternative explanation for the seemingly "non-local" behaviors observed. Albert Einstein, in particular, was uneasy about the implications of entanglement and, in an attempt to convey the counterintuitive nature of this quantum behavior, famously referred to it as "spooky action at a distance."

Yet, as more research was conducted, it became clear that entanglement was not merely a theoretical curiosity, but an intrinsic and fundamental aspect of quantum mechanics. Its validation through numerous experiments has cemented it as a cornerstone of quantum information theory, opening doors to a multitude of applications from quantum teleportation to quantum computing. However, the rich tapestry of quantum correlations is not limited

to entanglement alone. Quantum discord is another fascinating measure that distinguishes between classical and quantum correlations in mixed quantum states [26]. Unlike entanglement, which zeroes in on the non-separability of quantum states, quantum discord probes into the very essence of "quantumness" in correlations, revealing peculiarities even in systems not traditionally viewed as entangled. But these theoretical foundations truly came to life in experimental settings, particularly with the violation of the Bell inequalities. Proposed by physicist John Bell, these inequalities established criteria that any classical local hidden variable theory must meet. If quantum mechanics had merely been a manifestation of some underlying classical processes, these inequalities should not have been violated. Enter Alain Aspect (The Nobel Prize in Physics 2022). In the early 1980s, Aspect conducted a series of groundbreaking experiments that tested the Bell inequalities [27]. The results Violations of the inequalities were observed, providing strong evidence against local hidden variable theories and bolstering the non-classical and non-local nature of quantum mechanics. In the transition from theoretical principles to practical applications in quantum computing, the classical bit is replaced by the quantum bit, or qubit, which has the unique ability to exist in a superposition of both 0 and 1 states at once, unlike its classical counterpart. However, creating a stable qubit that can maintain its quantum state long enough to execute computations remains a significant challenge. This is where quantum dots come into the picture. Quantum dots, with their ability to confine electrons in three dimensions, offer an enticing solution. When an electron is trapped within a quantum dot, its spin - a quantum property akin to a tiny magnetic moment - can be harnessed as a qubit. The relative isolation of the quantum dot can shield the electron from external influences, potentially offering longer coherence times, which is the duration a qubit can retain its quantum state. Furthermore, the ability to tune quantum dots means that they can be precisely engineered to specific frequencies, allowing for interactions between qubits. Additionally, quantum dots can be positioned with remarkable precision on semiconductor chips, aligning with established manufacturing techniques and making them compatible with existing semiconductor infrastructures. Another key advantage of quantum dots is the potential for scalability. With semiconductor technologies advancing and transistors shrinking in size, quantum dots offer a pathway to integrate potentially millions of qubits on a single chip. This integration capability is paramount if quantum computers are to surpass their classical counterparts in real-world applications.

In this thesis, our first aim is to investigate the dynamics of quantum correlations within two excitonic qubits embedded in two coupled semiconductor InAs quantum dots independently interacting with dephasing reservoirs. Their behavior in both Markovian and non-Markovian environments is explored against dimensionless time and temperature. Moreover, the effects of the external electric field on these correlations as well as the effects related to the Förster interaction are extensively analyzed. The second is to study the behavior of global quantum discord and entanglement in two coupled double quantum dots made of AlGaAs/GaAs as a function of temperature. We use each double quantum dot as a qubit, where the electron can occupy either the right or left dot. The goal of our investigation is to understand the impact of the energy offset of each qubit and the tunneling coupling energy on quantum correlations. The final aim is to use the three InAs quantum dots as a working substance of a quantum heat engine, which allows the engine to operate at very small scales, in the presence of an electric field, and the Forster mechanism, which describes the transfer of energy between quantum dots and affects thus the engine's behavior. In this regard, we study the behavior of the work performed by the engine and the entanglement in the system as the Forster parameter is varied.

The structure of this thesis is laid out as follows:

- Chapter I delves into the essential tools and principles related to semiconductor quantum dots. Specifically, it explores the motion of charge carriers within semiconductors

and the density of states in the conduction band. This chapter also introduces foundational models of quantum wells, wires, and dots. Concluding the chapter, we discuss zero-dimensional systems and their practical implementation.

- In Chapter II, we talk about the basics of quantum mechanics and information theory. We look at the main rules of quantum mechanics, what a quantum state is, and important ideas in quantum physics like entanglement and superposition. We also discuss the standard ideas in information theory and dive deeper into quantum information. We then explore how quantum systems can be connected and measured. We also touch upon a topic called quantum discord. At the end of the chapter, we share our study from the paper [28], focusing on the study of Global Quantum Discord and Entanglement in two interconnected AlGaAs/GaAs Double Quantum Dots.

- In Chapter III, we journey through the foundational concepts of quantum theory, especially in the context of open systems. A special emphasis is placed on non-Markovianity, as we explore measures that identify the depth of memory effects by observing the information flow between a system and its corresponding environment. Our research findings are showcased in several works: in [29], we meticulously analyze the dynamics of quantum correlations within two coupled semiconductor InAs quantum dots; [30] offers a detailed exploration of the use of the Wigner Function as an Entanglement Detector in such quantum dot systems; and [31] delves into the resilience of Wigner function negativity, especially when faced with exciton-exciton interaction effects within these coupled semiconductor dots.

- In chapter IV, we present our paper [32], in which we utilize three InAs quantum dots as the functional material for a quantum heat engine. This enables the engine to function at extremely tiny scales, influenced by an electric field and the Forster mechanism. This mechanism outlines the energy transfer between quantum dots and subsequently impacts the engine's operations. Consequently, we investigate the engine's work output and the system's entanglement as we adjust the Forster parameter.

- In Chapter V, we outline the conclusions drawn from our research and discuss potential directions for future exploration.

# Chapter 1

# Semiconductor Quantum Dots

## 1.1 Overview on Semiconductors

### 1.1.1 What is a semiconductor?

A semiconductor [33] is a material that can either conduct or not conduct electricity depending on certain conditions; it is used in many electronic devices such as transistors [34, 35], diodes [36, 37, 38], and solar cells [39, 40, 41]. It is an essential component of modern electronic devices and technologies, including computers, TV screens [42, 43, 44], telecommunications, energy systems, and consumer electronics like mobile phones, laptops, and microwaves [45]. The high demand for semiconductors in these areas is one of the reasons for the delay in manufacturers producing many electronic devices. Noting that there is no single definition for semiconductors when it comes to conductivity and resistivity of materials, semiconductors exhibit a conductivity $\sigma$ and resistivity $\rho$ that falls between those of metals and insulators (see fig. 1.1).

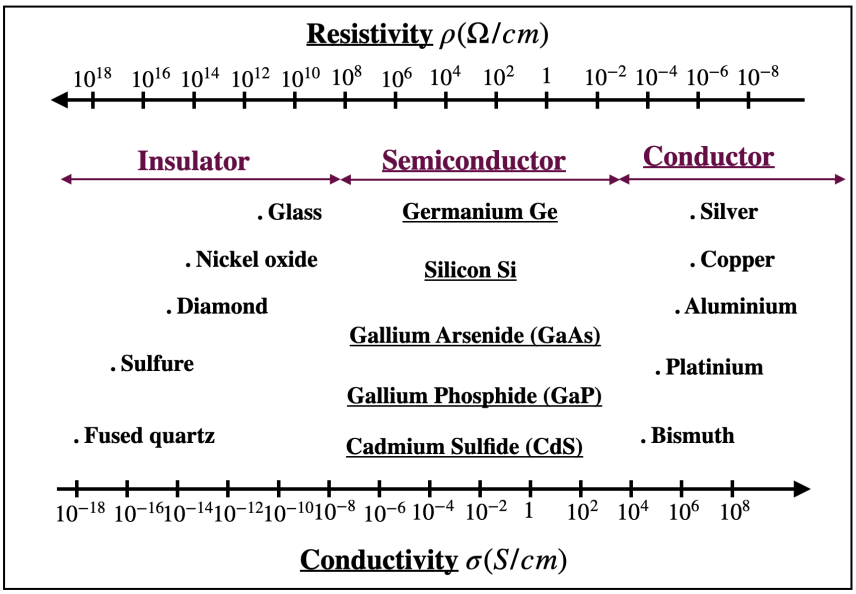


FIGURE 1.1: Typical range of conductivities for insulators, semiconductors, and conductors.

In electrical engineering, a material is said to be conductive if it allows the passage of electric current; it is a material that has a low electrical resistivity which is the inverse of the electrical conductivity observed. Physically, a given material is a conductor (of electricity) if it has free electrons (at least one electron per atom). These electrons are present in the layers far from the nucleus. The binding forces with the latter being weak, tend to move within the

conductive material from one atom to another. This movement in the absence of an external electric field is disordered and does not generate an electric current. However, if an external electric field is applied, imposing a potential difference between the ends of a conductor, these free electrons will undergo electric forces. The initial disordered movement becomes an ordered movement, hence the appearance of an electric current.
In metals, the conduction happens with a single type of carrier, which are the electrons. But in the semiconductors, the conduction occurs through several means:

- Through the free electrons ( type N).
- Through the free holes (type P).
- Through the two types of carriers.

The conductivity (or resistivity) of semiconductors is very sensitive to temperature and concentration of impurities. A semiconductor is said to be intrinsic (pure) if it contains few impurities compared to the number of holes and electrons generated thermally.

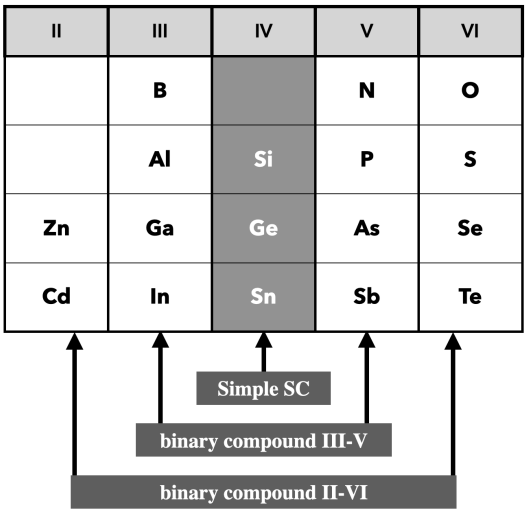


FIGURE 1.2: The semiconductors periodic table

.

Figure 1.2 presents the semiconductor's periodic table, which contains the single species of elements, such as Germanium (Ge) which was the first semiconductor used, Silicon (Si) which is the most used in the industry because it has a number of unique properties that make it well suited for many different applications, and Tin (Sn) in column IV of the Mendeleev table. There are also compounds Semiconductors, which are composed of two ( binary III-V or II-VI compounds), three elements (Ternary compounds), and four elements (Quaternary compounds). We present below some examples of ternary compounds and quaternary compounds:

- Ternary compounds semiconductors:
  AlGaAs (Aluminum Gallium Arsenide), AlAsSb (Aluminum Arsenide Antimonide), InSbAs (Indium Antimonide Arsenide), GaSbP (Gallium Antimonide Phosphide), and InGaP (Indium Gallium Phosphide).
- Quaternary compounds semiconductors:
  InAlGaSb (Indium Aluminum Gallium Antimonide), AlGaInP (Aluminum Gallium Indium Phosphide), and InGaAsN (Indium Gallium Arsenide Nitride).

### 1.1.2 Energy band in solids

#### Electron in an atom

The Bohr model is sufficient to describe the system of a single electron in an atom (Hydrogen). We show that the energy is quantified, and it is written,

$$E_n = -\frac{E_0}{n^2}, \tag{1.1}$$

Where $E_0$ is a constant ($E_0 = 13,6eV$), and n is the principal quantum number.
Only quantum mechanics can solve the problem of an atom with many electrons, and we can show that the energy levels are discrete, and the electrons are distributed according to the Pauli exclusion principle, which forbids two electrons of the same atom to have identical quantum numbers.

#### Electrons in a solid

The electron is affected not only by its own nucleus and its electronic environment but also by the nuclei and electrons of neighboring atoms, the solution of the Schrödinger equation applied to the system constituted by an electron in a solid, shows again that the energy levels of the electron are grouped in authorized energy bands (see Figure 1.3a).

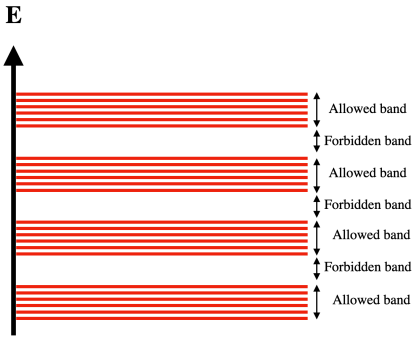


FIGURE 1.3: The energy levels of the electrons.

**The valence band**: the last authorized band completely filled. It contains the electrons that participate in the bonds.
**Conduction band**: it is the band that comes just above the valence band. It can be either empty or partially filled; it can never be completely filled.

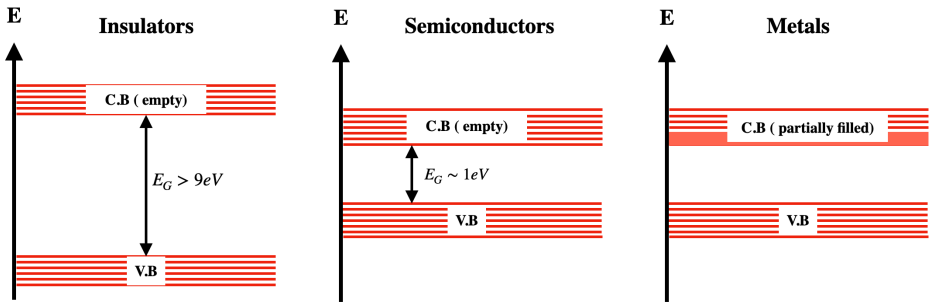


FIGURE 1.4: Valence and conduction bands for insulators, semiconductors, and metals.

Figure 1.4 shows the difference between metals, semiconductors, and insulators that in an insulator the valence band's electrons are separated by a large gap $E_G$ from the conduction band, in conductor metals the valence band and conduction band are overlapping, and in semiconductors, there is a small band gap between the valence and conduction bands that excitation can make electrons moving to the conduction band, in this case, the semiconductor behaves as a conductor to make the current flow. We note that $E_G = E_c - E_c$, where $E_c$ and $E_v$ are the energy of the conductance and the valence band respectively.
Notice that a completely filled band does not participate in the conduction of electricity, and for an insulator or a semiconductor the valence band is full and the conduction band is empty at $T = 0K$, in this case, there is no conduction. at $T > 0K$ the electrons have a kinetic energy of thermal agitation, $E_C = \frac{3}{2}K_BT$. A certain number of electrons can pass from the valence band to the conduction band if the value of $E_G$ is not too high. When the electron leaves the valence band for the conduction band, it leaves a void in the bond between two atoms called a hole. The loss of the electron leads to the appearance of a positive charge, and the existence of the hole behaves as a positive charge that captures a neighboring electron, which gives another hole in the place of the latter. This process repeats itself indefinitely and is called generation-recombination. We can present some examples of the gap energy of different semiconductors,

| **Type** | **Semiconductors** | $E_G(eV)$ |
|---|---|---|
| IV | C | 5.3 |
| IV | Si | 1.1 |
| IV | Ge | 0.17 |
| IV | SiC | 2.8 |
| III-V | GaAs | 1.4 |
| III-V | GaP | 2.3 |
| III-V | InAs | 0.40 |
| II-VI | CdS | 2.6 |
| II-VI | CdSe | 1.7 |
| II-VI | CdTe | 1.5 |
| II-VI | ZnS | 3.6 |
| II-VI | ZnSe | 2.6 |

TABLE 1.1: Gap energy values for different semiconductors .

## 1.2 Movement of charge carriers in semiconductors

**Electron in a vacuum:**
Under the action of an electric field $\vec{E}$ an electron takes a uniformly accelerated motion with a time dependent speed,

$$\vec{v} = -\frac{e}{m_e^*}\vec{E}.t + \vec{cst}. \tag{1.2}$$

Where $e$ is the charge of the electron, $m_e^*$ is the effective mass of the electron, $\vec{E}$ is the electric field, $t$ represents the time, and $\vec{cst}$ is an arbitrary constant vector.

**Electron in a solid:**
The free electrons of the conduction band move in the presence and the absence of an electric field $\vec{E}$ (Figure 1.5). When the electric field is absent, the movement of the electrons is

disordered in all directions because of the thermal origin. In this case, the average speed is null, on the other hand, when we apply an electric field the electrons acquire an additional speed that is superimposed on the thermal motion. In this case, the electron will be submitted to uniformly accelerated movements broken by collisions with the atoms of the lattice, due to the electrostatic force $\vec{F_e} = q.\vec{E}$, the acceleration of the electron can be given by the equation,

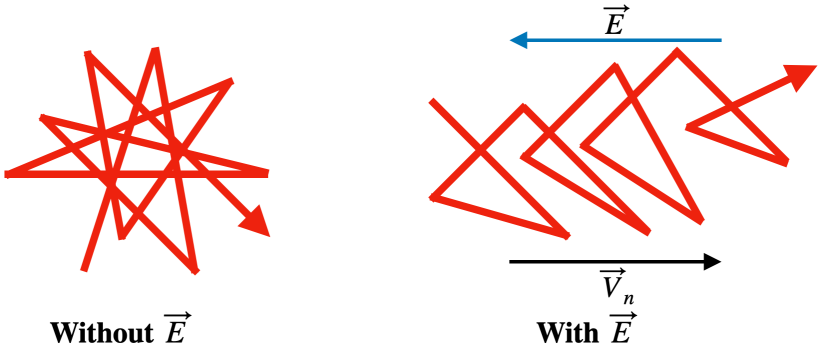


FIGURE 1.5: Movement of the electrons in the presence and absence of an electric field $\vec{E}$.

$$\vec{\gamma_n} = \frac{q.\vec{E}}{m_e^*}. \tag{1.3}$$

This acceleration acts between two shocks separated by an average time called $\tau$. The average speed of electrons is given by,

$$\vec{v_n} = \vec{\gamma_n}.\tau = \frac{q\tau\vec{E}}{m_e^*} = -\mu_n.\vec{E}. \tag{1.4}$$

We can apply the same reasoning to free holes, one can find that,

$$\vec{v_p} = \vec{\gamma_p}.\tau = \frac{q\tau\vec{E}}{m_h^*} = \mu_p.\vec{E}. \tag{1.5}$$

Where $\mu_n$ and $\mu_p$ are called the mobility of electrons and holes respectively, which depend on the charge, and the temperature, and are expressed in $cm^2V^{-1}s^{-1}$. Table 1.2 shows values of $\mu_n$ and $\mu_p$ for some semiconductors.

| **Semiconductors** | $\mu_n\ (cm^2V^{-1}s^{-1})$ | $\mu_p\ (cm^2V^{-1}s^{-1})$ |
|---|---|---|
| Ge | 3900 | 1900 |
| Si | 1500 | 600 |
| GaAs | 8500 | 400 |
| InSb | 78000 | 750 |

TABLE 1.2: mobility of electrons and holes for different semiconductors.

### 1.2.1 The current density

Consider a solid with a free electron density $n_e(cm^{-3})$. When the solid is under an electric field $\vec{E}$, the electrons acquire an average speed $v_n$,

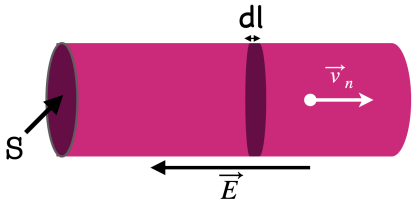


the total mobile charge contained in the small volume $dV$ is :

$$dQ = -q.n_e.S.dl, \qquad \vec{dl} = \vec{v_n}.dt. \tag{1.6}$$

The current intensity is given by,

$$i = \frac{dQ}{dt} = -q.n_e.V_n.S. \tag{1.7}$$

The current density is defined as,

$$\vec{J} = \frac{\vec{i}}{S} = -q.n_e.\vec{v_n} = q.n_e.\mu_n.\vec{E}. \tag{1.8}$$

In the general case,

$$\vec{J_n} = q.n_e.\mu_n.\vec{E} = \sigma_n.\vec{E}, \qquad \vec{J_p} = q.p_e.\mu_p.\vec{E} = \sigma_p.\vec{E}, \tag{1.9}$$

with $\sigma_n = q.n_e.\mu_n$ and $\sigma_p = q.ne.\mu_p$ are the conductivities of the solid. The total conductivity of a solid is given by,

$$\sigma = \sigma_n + \sigma_p. \tag{1.10}$$

### 1.2.2 Conduction of an intrinsic semiconductor

Semiconductors (Germanium or Silicon) have four electrons on their peripheral layer because they belong to the fourth column of the periodic classification of elements. It is possible to produce them with a high degree of purity (less than one impurity atom for $10^{11}$ atoms of semiconductors), it is then called an intrinsic semiconductor. Consider a non-excited silicon crystal at absolute zero ($0K$) in the dark. In order to see eight electrons on its external layer, each silicon atom puts its four peripheral electrons with the neighboring atoms. This pooling of electrons, called a covalent bond, ensures the cohesion of the silicon crystal. The electrons that participate in these bonds are strongly linked to the silicon atoms. There is therefore no mobile charge likely to ensure the flow of an electric current. The semiconductor is then an insulator, indeed the valence band is saturated, and all places are occupied while the conduction band which offers free places is empty. However, at ambient temperature, a certain number of electrons of the valence band pass to the conduction band by leaving behind them the same number of holes. This phenomenon concerns only a very small number of silicon atoms (one atom in $10^{13}$ at a temperature of $300K$), in this case, the intrinsic carrier concentration ($n_i$) in intrinsic semiconductors is represented by the equality of the number of electrons ($n_e$) and the number of holes ($n_p$). This is a fundamental property of intrinsic semiconductors and holds true at thermal equilibrium, where the absence of impurities or dopants results in equal numbers of electrons and holes:

$$n_e = n_p = n_i. \tag{1.11}$$

When an electric field is applied to an intrinsic semiconductor there is displacement of electrons in the opposite direction to the field, and displacement of holes in the direction of the field. The current densities of electrons and holes are given by equation (1.9), the total current density $J_T$ is given by,

$$\vec{J_T} = \vec{J_n} + \vec{J_p} = \sigma_i.\vec{E}, \tag{1.12}$$

with $\sigma_i = \sigma_n + \sigma_p = qn_i(\mu_n + \mu_n)$. The resistivity of an intrinsic semiconductor can be written as,

$$\rho_i = \frac{1}{\sigma_i} = \frac{1}{qn_i(\mu_n + \mu_n)}. \tag{1.13}$$

### 1.2.3 Conduction of an extrinsic semiconductor

The introduction of certain elements (dopants) in very small quantities in a semiconductor can considerably increase the number of free carriers "electrons or holes" and thus reduce the resistivity of the material (increase its electrical conductivity). The semiconductor is called extrinsic or doped (N or P). Extrinsic semiconductors are used in electronic devices such as transistors and solar cells. The dopant atoms change the properties of the semiconductor crystal lattice, creating an excess or deficiency of electrons that can be used to control the flow of electrical current. There are two main types of extrinsic semiconductors:

**N-type semiconductor**: doped with impurities of the V column which are called donors. These atoms have five electrons on their peripheral layers. By substituting into the semiconductor crystal lattice, they easily lose their fifth electron since four electrons are sufficient to ensure the covalent bond. These electrons leave behind them fixed positive charges at the nuclei which are not equivalent to holes and cannot participate in conduction. In N-type semiconductors, the excess of electrons increases the conductivity of the semiconductor, making it a good conductor of electricity.

**P-type semiconductor**: doped with impurities from column III which are called acceptors. The trivalent atom lacks an electron to establish covalent bonds with the four semiconductor atoms that surround it. In fact, the electrons that participate in the bonds are indistinguishable from each other. Everything happens as if one of the neighboring semiconductor atoms had given up an electron to the trivalent boron atom, thus creating a hole in the semiconductor crystal. The atom that receives an electron is called an acceptor, it has lost its neutrality to become a fixed negative ion. At ordinary temperatures, almost all acceptor atoms are ionized.

## 1.3 Density of state in the conduction band

### 1.3.1 3D systems:

We consider an electron of the conduction band free to move under the crystal, and we assume that a crystal is approximated by a cube, where L is the length of the cube. We search the possible states of the electron in the cube and the corresponding energies. In this regard, we need to solve the Schrödinger equation:

$$-\frac{\hbar^2}{2m^*}\left(\frac{d^2}{dx^2} + \frac{d^2}{dy^2} + \frac{d^2}{dz^2}\right)\Psi(x,y,z) = E\Psi(x,y,z). \tag{1.14}$$

The solution of this equation has the following form,

$$\Psi(x,y,z) \sim e^{ik_x}e^{ik_y}e^{ik_z}. \tag{1.15}$$

This leads to the expression of energies:

$$E = \frac{\hbar^2}{2m^*}(k_x^2 + k_y^2 + k_z^2). \tag{1.16}$$

We consider the Born-Von Karman (BVK) boundary conditions,

$$\Psi(x+L,y,z) = \Psi(x,y,z), \tag{1.17}$$

$$\Psi(x,y+L,z) = \Psi(x,y,z), \tag{1.18}$$

$$\Psi(x,y,z+L) = \Psi(x,y,z). \tag{1.19}$$

From equation 1.17 we show that,

$$\begin{aligned} e^{ik(x+L)}e^{ik_y}e^{ik_z} &= e^{ik_x}e^{ik_y}e^{ik_z}, \\ \Rightarrow e^{ik_xL} &= 1, \\ \Rightarrow k_{nx} &= \frac{2\pi}{L}n_x, \end{aligned} \tag{1.20}$$

Using the same reasoning, we can show that,

$$k_{ny} = \frac{2\pi}{L}n_y, \qquad k_{nz} = \frac{2\pi}{L}n_z. \tag{1.21}$$

The electronic states are presented by the wave vector $\vec{k}$ in the coordinate space $(k_x, k_y, k_z)$, where the elementary volume is given by $V = (\frac{2\pi}{L})^3$.

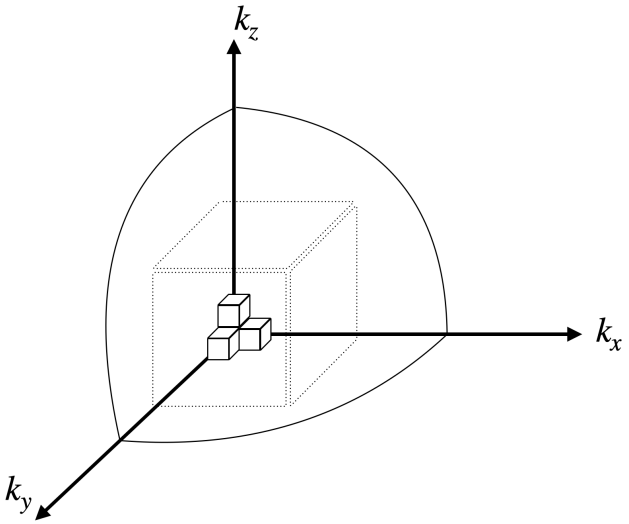


All energy states between $E$ and $E + dE$ have their representative points in the space between the spheres of radius $k$ and $k + dk$, with $E = \frac{\hbar^2k^2}{2m^*} \Rightarrow dE = \frac{\hbar^2}{m^*}k.dk$.

The reciprocal volume $\nu_1$, which represents the smallest space occupied by a single state, is

$$\nu_1 = \frac{(2\pi)^3}{L^3}. \tag{1.22}$$

For $N^{3D}$ states, the reciprocal volume occupied is

$$\nu_N = \frac{4}{3}\pi k^3. \tag{1.23}$$

The number of states can be determined by evaluating the ratio of reciprocal volumes,

$$\begin{aligned} N^{3D} &= 2 * \frac{\nu_N}{\nu_1}, \\ &= \frac{L^3}{3\pi^2}k^3. \end{aligned} \tag{1.24}$$

Factor 2 is included to account for the fact that each state can be occupied by both spin-up and spin-down carriers. In terms of energy this can be written as

$$\begin{aligned} N^{3D} &= \frac{L^3}{3\pi^2}(\sqrt{\frac{2m^*E}{\hbar^2}})^3, \\ &= \frac{L^3}{3\pi^2}(\frac{2m^*}{\hbar^2})^{3/2}E^{3/2}. \end{aligned} \tag{1.25}$$

The density of states $N(E)$ is equal to a derivative of the number of states with respect to the energy $E$:

$$N(E) = \frac{dN}{dE}.$$

We can finally get the density of states for 3D systems,

$$N(E) = \frac{L^3}{2\pi^2}(\frac{2m^*}{\hbar^2})^{3/2}\sqrt{E} \tag{1.26}$$

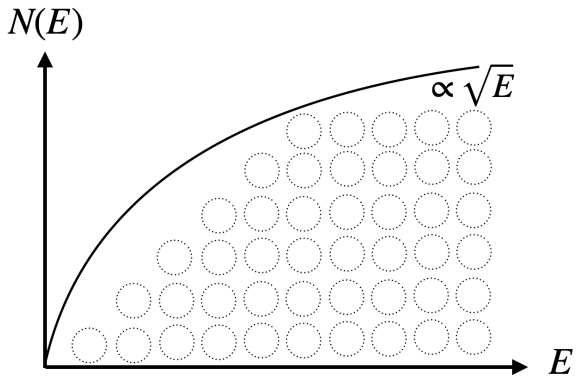


FIGURE 1.6: The density of states as a function of energy in $3D$ systems.

Therefore, the density of states within a band, specifically near a minimum point where the energy can be described as a parabolic function of momentum, is smooth and proportional to the energy's square root (see Figure 1.6).

### 1.3.2 $2D$ systems:

In Two-dimensional systems, the density of states can be determined similarly (see Figure 1.7). In this case, there are only two degrees of freedom, and we can represent a state by the values of $n_x$ and $n_y$ to create a circular shape in $k$-space, which is referred to as a two-dimensional electron (or hole) gas.

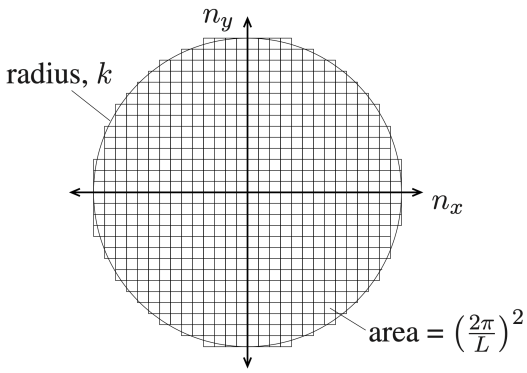


FIGURE 1.7: Filling the momentum states within a 2D quantum well.

The reciprocal area $A_1$, which represents the smallest space occupied by a single state, is

$$A_1 = \frac{(2\pi)^2}{L^2}. \tag{1.27}$$

For $N^{2D}$ states, the reciprocal area occupied is

$$A_N = \pi k^2. \tag{1.28}$$

We find the number of states $N^{2D}$ analogously to the three-dimensional case by calculating the ratio of the reciprocal areas, also taking account of the spin of electrons by multiplying by 2,

$$\begin{aligned} N^{2D} &= 2 * \frac{A_N}{A_1}, \\ &= \frac{L^2}{2\pi} k^2, \\ &= \frac{L^2}{2\pi} (\sqrt{\frac{2m^*E}{\hbar^2}})^2, \\ &= \frac{L^2}{2\pi} * \frac{2m^*E}{\hbar^2}. \end{aligned} \tag{1.29}$$

The density of states for 2D systems is given by,

$$N(E) = \frac{dN^{2D}}{dE} = \frac{L^2 m^*}{\pi\hbar^2} = constante. \tag{1.30}$$

As evident from the formula, the two-dimensional density of states remains unchanged by changing the energy E. Consequently, the 2D density of states remains constant across all possible electron energies (see Figure 1.8).

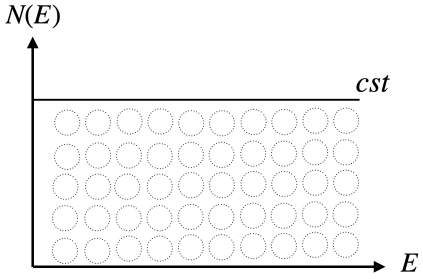


FIGURE 1.8: The density of states as a function of energy in $2D$ systems.

### 1.3.3 $1D$ systems:

In One-dimensional systems, there is only one degree of freedom. The electron momentum then fills states along a line,

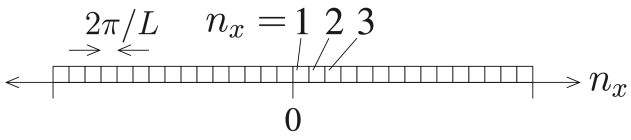


FIGURE 1.9: Filling the momentum states within a 1D quantum wire.

Continuing with the previous reasoning, the total number of states $N^{1D}$, can be obtained by dividing the length of the line in $k$-space by the length occupied by one state, and further dividing it by the length in real space:

$$\begin{aligned} N^{1D} &= \frac{\zeta_N}{\zeta_1} = \frac{L}{\pi}k, \\ &= \frac{L}{\pi}\sqrt{\frac{2m^*E}{\hbar^2}}, \\ &= \frac{L}{\pi}(\frac{2m^*}{\hbar^2})^{1/2}E^{1/2}. \end{aligned} \tag{1.31}$$

If the spin is to be taken into account, we obtain finally the one-dimensional density of states N(E),

$$N(E) = \frac{L}{\pi}(\frac{2m^*}{\hbar^2})^{1/2}\frac{1}{\sqrt{E}}. \tag{1.32}$$

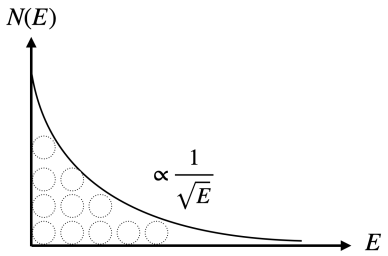


FIGURE 1.10: The density of states as a function of energy in $1D$ systems.

### 1.3.4 0D systems:

In a 0D system (Quantum Dots), no free motion is possible because there is no $k$-space to be filled with electrons and all available states exist only in discrete energies, resulting in quantized energy states represented by a delta function:

$$N(E) = 2\delta(E).$$

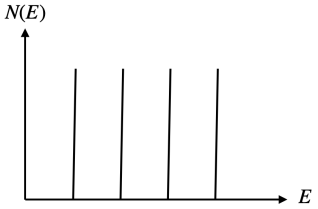


FIGURE 1.11: The density of states as a function of energy in $0D$ systems.

In the table below 1.3, we compare the density of states for bulk (3D), quantum wells (2D), and quantum wires (1D), we observe that each reduction in the electron motion's degrees of freedom results in a decrease in the functional form of $N(E)$ by factors of $E^{1/2}$.

| **Dimensionality** | $N(E)$ | |
|---|---|---|
| 3D | $\frac{L^3}{2\pi^2}(\frac{2m^*}{\hbar^2})^{3/2}\sqrt{E}$ | $\propto E^{\frac{1}{2}}$ |
| 2D | $\frac{L^2 m^*}{\pi\hbar^2}$ | $\propto E^0$ |
| 1D | $\frac{L}{\pi}(\frac{2m^*}{\hbar^2})^{1/2}\frac{1}{\sqrt{E}}$ | $\propto E^{-\frac{1}{2}}$ |
| 0D | $2\delta(E)$ | $\propto \delta(E)$ |

TABLE 1.3: The density of states for reduced dimensionality systems.

## 1.4 Calculation of the carrier concentration:

It is necessary to determine the concentration of electrons in the conduction band and the concentration of holes in the valence band, to define the density of states in the conduction and the valence bands, and the occupation probability of each energy state $E$ denoted $f(E)$.

### 1.4.1 Density of state in the conduction and valence bands

We can use the same method as used in the previous section to define the density of states in the conduction and valence bands. One can show that in the conduction band, we have

$$N(E) = \frac{4\pi}{h^3}(2m_e^*)^{3/2}.(E - E_c)^{1/2}, \tag{1.33}$$

While for the valence band, it is given by

$$N(E) = \frac{4\pi}{h^3}(2m_h^*)^{3/2}.(E_v - E)^{1/2}. \tag{1.34}$$

### 1.4.2 Fermi-Dirac function

the probability of occupation at temperature $T$ of an energy level $E$ by an electron is given by the Fermi-Dirac function:

$$f(E) = \frac{1}{1 + e^{\frac{(E-E_F)}{K_B T}}}, \tag{1.35}$$

Where $E_F$ is the Fermi level defined by $f(E_F) = \frac{1}{2}$; we note that $E_F$ is a constant. The probability that the level is unoccupied is,

$$1 - f(E) = \frac{1}{1 + e^{-\frac{(E-E_F)}{K_B T}}}; \tag{1.36}$$

it is also the probability of having a hole of energy E.

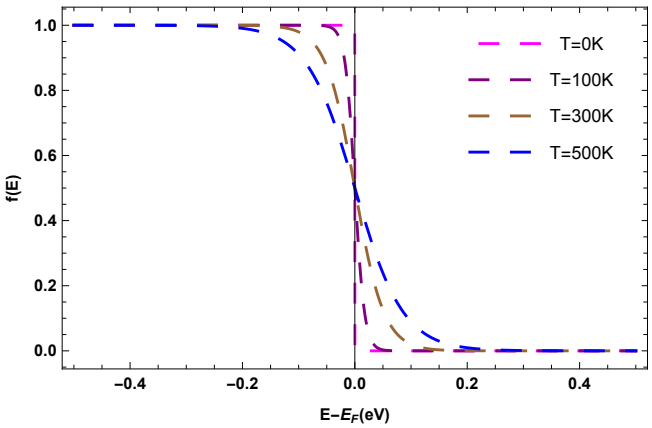


FIGURE 1.12: Fermi distribution function vs $(E - E_F)$ for various temperatures.

- At $T = 0K$, $f(E) = 1$ for $E < E_F$, and $f(E) = 0$ for $E > E_F$. In this case, all energy states below $E_F$ are occupied, and all states above $E_F$ are empty.
- At $T > 0$, the function $f(E)$ is symmetric with respect to $E_F$, which means that the probability that the energy level $E_F + dE$ is occupied is equal to the probability that the energy level $E_F - dE$ is unoccupied. Notice that $90\%$ of the function f(E) variation occurs between $\pm 3k_B T$ of $E_F$. Outside this range, $f(E)$ can be approximated by :

$$E - E_F \gg 3K_B T : e^{\frac{E-E_F}{K_B T}} \gg 1 \Longrightarrow f(E) \approx e^{-\frac{E-E_F}{K_B T}}$$

$$E_F - E \gg 3K_B T : e^{\frac{E-E_F}{K_B T}} \ll 1 \Longrightarrow f(E) \approx 1 - e^{\frac{E-E_F}{K_B T}}$$

### 1.4.3 Concentration of free electrons and free holes at thermodynamic equilibrium

**Free electrons:**

The concentration of free electrons in the conduction band is equal to the number of places occupied in this band.

$$\begin{aligned}
n &= \int_{E_C}^{\infty} N(E).f(E)\,dE, \\
&= \frac{1}{2\pi^2}(\frac{2m_e}{\hbar^2})^{\frac{3}{2}} \int_{E_C}^{\infty} (E-E_C)^{\frac{1}{2}}.e^{-(\frac{E-E_F}{K_BT})}\,dE, \\
&= \frac{1}{2\pi^2}(\frac{2m_e}{\hbar^2})^{\frac{3}{2}} \int_{E_C}^{\infty} (E-E_C)^{\frac{1}{2}}.e^{-(\frac{E-E_F}{K_BT})}\,dE, \\
&= \frac{1}{2\pi^2}(\frac{2m_e}{\hbar^2})^{\frac{3}{2}} \int_{E_C}^{\infty} (E-E_C)^{\frac{1}{2}}.e^{-(\frac{E-E_C+E_C-E_F}{K_BT})}\,dE, \\
&= \frac{1}{2\pi^2}(\frac{2m_e}{\hbar^2})^{\frac{3}{2}}.e^{-(\frac{E_C-E_F}{K_BT})} \int_{E_C}^{\infty} (E-E_C)^{\frac{1}{2}}.e^{-(\frac{E-E_C}{K_BT})}\,dE, \\
&= \frac{1}{2\pi^2}(\frac{2m_e}{\hbar^2})^{\frac{3}{2}}.e^{-(\frac{E_C-E_F}{K_BT})}.(K_BT)^{\frac{1}{2}} \int_{E_C}^{\infty} (\frac{E-E_C}{K_BT})^{\frac{1}{2}}.e^{-(\frac{E-E_C}{K_BT})}\,dE. \qquad (1.37)
\end{aligned}$$

If we put $x = (\frac{E-E_C}{K_BT})$, or $dx = \frac{dE}{K_BT}$, the previous equation becomes,

$$\begin{aligned}
n &= \frac{1}{2\pi^2}(\frac{2m_e}{\hbar^2})^{\frac{3}{2}}.e^{-(\frac{E_C-E_F}{K_BT})}.(K_BT)^{\frac{3}{2}} \int_0^{\infty} \sqrt{x}e^{-x}dx, \\
&= \frac{1}{2\pi^2}(\frac{2m_e}{\hbar^2})^{\frac{3}{2}}.e^{-(\frac{E_C-E_F}{K_BT})}.(K_BT)^{\frac{3}{2}} \times \frac{\sqrt{\pi}}{2},
\end{aligned}$$

$$n = N_C(T).e^{-(\frac{E_C-E_F}{K_BT})}. \qquad (1.38)$$

Where $N_C(T) = 2.(\frac{m_eK_BT}{2\pi\hbar^2})^{\frac{3}{2}}$ is the effective density of states at temperature $T$ in the conduction band.

**Free holes:**

The concentration of free holes in the valence band is equal to the number of places unoccupied in this band,

$$p = \int_{-\infty}^{E_V} N(E)[1-f(E)]\,dE. \qquad (1.39)$$

We can use the same method as in the previous demonstration, and we can find that,

$$p = N_V(T)e^{-(\frac{E_F-E_V}{K_BT})}. \qquad (1.40)$$

With $N_V(T) = 2 \times (\frac{m_hK_BT}{2\pi\hbar^2})^{\frac{3}{2}}$ being the effective density of states at temperature $T$ in the valence band. The table below shows the values of $N_C$ and $N_V$ for some semiconductors,

| Semiconductors | Ge | Si | GaAs |
|---|---|---|---|
| $N_C(cm^{-3}) =$ | $1,04 \times 10^{19}$ | $2,8 \times 10^{19}$ | $4,7 \times 10^{17}$ |
| $N_V(cm^{-3}) =$ | $6 \times 10^{18}$ | $1,04 \times 10^{18}$ | $7 \times 10^{18}$ |

TABLE 1.4: Values of $N_C$ and $N_V$ for Ge, Si, and GaAs at 300 K.

### 1.4.4 The n.p product (the mass action law):

When Eqs. 1.38 and 1.40 are multiplied together, we find that,

$$n \times p = N_C(T).N_V(T)e^{\frac{-E_G}{K_B T}}, \tag{1.41}$$

where $E_G$ is the energy gap, notice that $n \times p$ is a constant for a given semiconductor at temperature $T$ and independent of $E_F$. This product will play an important role and it can be expressed in the following form

$$n \times p = n_i^2, \tag{1.42}$$

with,

$$n_i = \sqrt{N_C.N_V}\, e^{\frac{-E_G}{2K_B T}}. \tag{1.43}$$

In the intrinsic semiconductor, thermal excitation can produce the movement of the electrons from the valence band to the conduction band. Each movement creates the electrons and holes in pairs with $n = p$; in this case, equation 1.42 can be expressed as,

$$n = p = n_i, \tag{1.44}$$

$n_i$ is the intrinsic carrier concentration, which depends on the gap energy $E_G$ and temperature. We give in the table below some examples of the intrinsic concentration for Si for different values of temperature.

| T(k) | 300 | 400 | 500 |
|---|---|---|---|
| $n_i(cm^{-3})$ | $1,45 \times 10^{10}$ | $5,7 \times 10^{12}$ | $1,5 \times 10^{14}$ |

TABLE 1.5: Values of the intrinsic carrier concentration $n_i$ for Si.

## 1.5 Fermi level position

### 1.5.1 Fermi position for an intrinsic semiconductor

In a semiconductor, we have four types of charges. Among these charges, two have a negative charge (electrons $n$ and acceptor ions $N_a$), and two have a positive charge (holes $p$ and donor ions $N_d$). At equilibrium, there is equality between positive and negative charges:

$$n + N_a = p + N_d. \tag{1.45}$$

Equations 1.42 and 1.45 can be solved for n and p, we can find that,

$$n = \frac{N_d - N_a}{2} + \sqrt{(\frac{N_d - N_a}{2})^2 + n_i^2}, \tag{1.46}$$

$$p = \frac{N_a - N_d}{2} + \sqrt{(\frac{N_a - N_d}{2})^2 + n_i^2}. \tag{1.47}$$

For an intrinsic semiconductor $n = p = n_i$,

$$n_i = N_C(T).e^{\frac{E_{Fi}-E_C}{K_BT}} = N_V(T).e^{\frac{E_V-E_{Fi}}{K_BT}},$$

$$\frac{N_C(T)}{N_V(T)} = e^{\frac{E_V-E_{Fi}}{K_BT} - \frac{E_{Fi}-E_C}{K_BT}},$$

$$ln(\frac{N_C(T)}{N_V(T)}) = \frac{1}{K_BT}.(E_V - E_{Fi} - E_{Fi} + E_C),$$

$$E_{Fi} = \frac{E_C + E_V}{2} - \frac{K_BT}{2}.ln(\frac{N_C(T)}{N_V(T)}). \tag{1.48}$$

In the intrinsic semiconductors $N_C(T) = N_V(T)$, we obtain that,

$$E_{Fi} = \frac{E_C + E_V}{2}. \tag{1.49}$$

This means that the Fermi level is at the midpoint of the band gap (Figure 1.13).

### 1.5.2 Fermi position for an N-type semiconductor

For N-type semiconductors, we can use a condition in which $N_d - N_a >> n_i$, in the equations (1.46, 1.47), which yields,

$$n = N_d - N_a, \tag{1.50}$$

$$p = n_i^2/n. \tag{1.51}$$

If, furthermore, $N_d >> N_a$, then,

$$n = N_d, \qquad and \qquad p = n_i^2/N_d. \tag{1.52}$$

In this case,

$$n = N_d = N_C(T).e^{-(\frac{E_C-E_F}{K_BT})}. \tag{1.53}$$

After simple calculations, we can find that,

$$E_F = E_C - K_BT.ln[\frac{N_C(T)}{N_d}]. \tag{1.54}$$

We note that this energy $E_F$ decreases with temperature (Figure 1.13).

### 1.5.3 Fermi position for a P-type semiconductor

For P-type semiconductors, we can use the condition $N_a - N_d >> n_i$, in the equations (1.46, 1.47). In this case,

$$p = N_a - N_d, \tag{1.55}$$

$$n = n_i^2/p. \tag{1.56}$$

If, furthermore, $N_d >> N_a$, then,

$$p = N_a, \qquad and \qquad n = n_i^2/N_a. \tag{1.57}$$

In this case,

$$p = N_a = N_V(T).e^{-(\frac{E_F - E_V}{K_B T})}. \tag{1.58}$$

Again, after simple calculations, we find,

$$E_F = E_V + K_B T.ln[\frac{N_V(T)}{N_a}]. \tag{1.59}$$

We note that this energy increases with temperature (Figure 1.13).

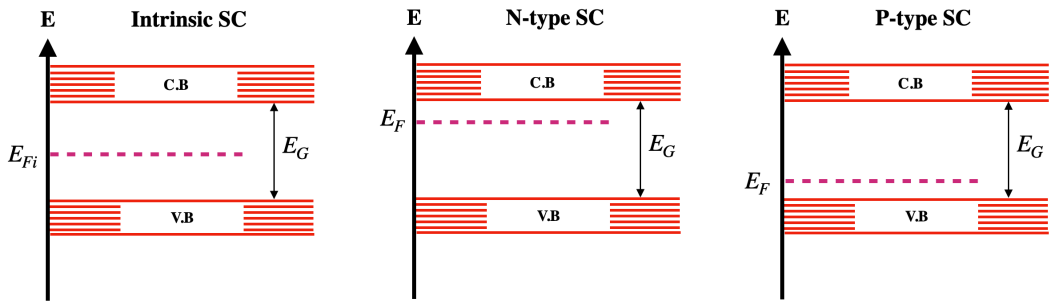


FIGURE 1.13: Fermi level position within the band gap in the case of intrinsic, N-type, and P-type semiconductors.

## 1.6 Inhomogeneous semiconductor: Diffusion

### 1.6.1 Definition

An inhomogeneous semiconductor is a semiconductor sample in which the properties $(n(x,y,z), \sigma(x,y,z), \rho(x,y,z)...)$ are not uniform in space of $(x,y,z)$. For simplicity, all reasoning will be done in a sample where all properties evolve only along the x-axis $(n(x), \sigma(x), \rho(x)...)$. In nature, matter moves from regions of high concentration to regions of low concentration, this movement is activated thermally, and the phenomenon of diffusion tends to reduce the gradients of concentrations. We consider the case of an N-type semiconductor, in which,

$$n(x) = n_0 = N_d, \qquad p(x) = p_0 = n_i^2/N_d^2. \tag{1.60}$$

When part of a semiconductor is illuminated, we can obtain a generation of pairs of electrons-holes (excitons) in this part,

$$n(x) = n_0 + \Delta n(x), \qquad p(x) = p_0 + \Delta p(x). \tag{1.61}$$

In the case of a low injection $\Delta n(x) << n_0$, there are more holes in the illuminated region, and they will move toward the regions where their density is lower. This phenomenon is called diffusion, this phenomenon ceases when the distribution has become uniform again.

### 1.6.2 First law of Fick

The first law of Fick explains the diffusion process, in which we observe the movement of carriers from a higher concentration to a lower concentration region, with a carrier flux $\Phi$ which presents the number of carriers that cross a unit of the surface during a unit of time. Fick's law of diffusion shows that the flux of the carriers is proportional to the gradient of their density.

$$\vec{\Phi_n} = -D_n.\vec{grad}\, n, \tag{1.62}$$

In the uni-dimensional case,

$$\Phi_n = -D_n.\frac{dn(x)}{dx}, \qquad \Phi_p = -D_p.\frac{dp(x)}{dx}, \tag{1.63}$$

$D_p$ and $D_n$ are diffusion coefficients of positive and negative carriers respectively.

### 1.6.3 Diffusion current density

Diffusion current density is due to the transport of carriers of the non-uniform concentration of charges in semiconductors. The current per unit area $J$ is given by the flux $\Phi$ multiplied by the value of the charge.
**Diffusion current density for electrons**:

$$J_{Dn}(x) = -q.\Phi_n(x) = q.D_n\frac{dn(x)}{dx}. \tag{1.64}$$

**Diffusion current density for holes:**

$$J_{Dp}(x) = q.\Phi_p(x) = -q.D_p\frac{dp(x)}{dx} \tag{1.65}$$

The constants $D_p$ and $D_n$ are related to the mobilities of electrons and holes by the Einstein relation:

$$\frac{D_p}{\mu_p} = \frac{D_n}{\mu_n} = \frac{K_BT}{q}. \tag{1.66}$$

If we have both an electric field and a gradient of carriers in a semiconductor, the charges move under the effect of

- **Electric field:** conduction current, $J_{Cn}$ and $J_{Cp}$.
- **Gradient of density:** diffusion current, $J_{Dn}$ and $J_{Dp}$.

The total current in this case is the sum of the conduction and the diffusion currents:

$$J = J_n + J_p, \tag{1.67}$$

Where,

$$J_n = q.n(x)\mu_n.E(x) + q.D_n.\frac{dn(x)}{dx}, \tag{1.68}$$

$$J_p = q.p(x)\mu_p.E(x) - q.D_p.\frac{dp(x)}{dx}. \tag{1.69}$$

In the general case,

$$\vec{J_T} = \vec{J_n} + \vec{J_p}, \tag{1.70}$$

with,

$$\vec{J_n} = q.n\mu_n.\vec{E} + q.D_n.\vec{\nabla}_n, \tag{1.71}$$

$$\vec{J_p} = q.p\mu_p.\vec{E} - q.D_p.\vec{\nabla}_p. \tag{1.72}$$

## 1.7 Non-equilibrium homogeneous semiconductor

An electron can pass from the valence band to the conduction band; it becomes free and this gives the creation of a hole in the valence band. This phenomenon is called the generation of an electron-hole pair. On the other side, a free electron passes from the conduction band to the valence band (disappearance of a hole), and it loses the energy. This phenomenon is called recombination. At thermodynamic equilibrium, generation and recombination are exactly equal, the density of holes $p_0$ and electrons $n_0$ is independent of time (stationary) and follows the law of mass action :

$$n_0.p_0 = n_i^2. \tag{1.73}$$

However, outside of thermodynamic equilibrium, the electron density is

$$n = n_0 + \Delta n, \tag{1.74}$$

and the density of the holes is:

$$p = p_0 + \Delta p. \tag{1.75}$$

In this case,

$$n.p \neq n_i^2. \tag{1.76}$$

There are two possible cases:

- $n.p < n_i^2$, it has fewer carriers than at thermodynamic equilibrium. It is a phenomenon of extraction.
- $n.p > n_i^2$, there are more carriers than at thermodynamic equilibrium. It is a phenomenon of injection (generation, accumulation).
  - When $\Delta n$ is of the same order as the density of minority carriers, it is a low-level injection.
  - When $\Delta n$ is comparable to the density of the majority carriers, it is a high-level injection.

### 1.7.1 generation of an electron-hole pair

The energy necessary for the creation of an electron-hole pair in a semiconductor can come from an external perturbation using photons, highly energetic particles ((ionizing radiation, hot carrier), or a strong electric field.

**photon-based generation:**

When the photon's energy $h\nu$ is less than the gap energy $E_G$ of a semiconductor, the photon is not absorbed and the semiconductor is transparent. To create a pair of electron-hole, it is necessary that the energy of the photon $h\nu$ be higher than the gap energy $E_G$ of a semiconductor, the photon is then absorbed and its energy causes the creation of a hole-electron pair. This condition exists if,

$$h\nu > E_G \iff \lambda(\mu m) < \frac{1,24}{E_G(eV)}. \tag{1.77}$$

In this case, the photon flux is defined by Beer-Lambert law,

$$\Phi(x) = \Phi_0 e^{-\alpha x}, \tag{1.78}$$

with $\alpha$ being the absorption coefficient. We can define the speed of generation by,

$$\begin{aligned} G(x) &= \frac{S.(\Phi(x) - \Phi(x+dx))}{S.dx}, \\ &= -\frac{\partial \Phi(x)}{\partial x}, \\ &= \Phi_0.\alpha.e^{-\alpha x}. \end{aligned} \tag{1.79}$$

**Generation by ionizing radiation:**

High-energy particles lose their energy by creating electron-hole pairs. In the case where the particle is completely stopped in the semiconductor, the number of electron-hole pairs created will determine its energy (nuclear detectors).

**Generation by a strong electrical field.**

In a semiconductor submitted to a very intense electric field, the free carriers are so fast (hot carriers), that they can behave like ionizing particles and create electron-hole pairs. This effect is cumulative, and the created carriers can also acquire energy and generate the creation of other electron-hole pairs.

### 1.7.2 Recombination:

An excess of electrons or holes compared to the equilibrium state leads to the increase of the recombination phenomenon to bring the system back to its equilibrium state. We can mention two types of recombination,

**Direct recombination:**

In the direct transition of an electron from the conduction band to the valence band (band-to-band recombination), the recovered energy can be,

- converted into photons (radiative recombination with light emission).
- Transformed into phonons (non-radiative recombination), in which the dissipation energy is in the form of thermal heating of the crystal lattice.
- Transferred to an electron in a conduction band that is transferred to a higher level or a hole in the valence band that is transferred to a lower level. This is called Auger recombination.

**Indirect recombination:**

The defects of the crystal lattice (interstitial, gaps, dislocations), or some chemical impurities (Au in Si, Cu in GaAs) give discrete energy levels located towards the middle of the forbidden band; they are deep levels. When a deep level captures an electron:

- The probability of capturing a hole is more important than that of sending back the electron; it will make a recombination. It is thus a center of recombination (recombination center).
- The electron can simply be re-emitted in the conduction band, the level has simply retained the electron for a certain time; it is a trap.

## 1.8 Simple models of quantum well, quantum wires and dots

Research has demonstrated that confining electrons or holes in a thin semiconductor layer causes a significant change in their behavior due to a reduction in dimensionality. This can be achieved by further reducing the electron's environment from a quantum well (two-dimension) to a quantum wire (one-dimension) and eventually to a quantum dot (zero-dimension). The dimension here refers to the number of freedoms of the electron's momentum. In a quantum wire, electrons are confined in two directions, reducing the degree of freedom to one, while in a quantum dot, they are confined in all three dimensions, reducing the degree of freedom to zero. We note that,

$$D_f + D_c = 3, \tag{1.80}$$

where $D_f$ and $D_c$ are the degrees of freedom and confinement respectively. The table below 1.6 shows the number of degrees of freedom $D_f$, with the number of directions of confinement $D_c$ of metals, quantum wells, quantum wires, and quantum dots.

| **Systems** | $D_c$ | $D_f$ |
|---|---|---|
| Bulk: | 0 | 3 |
| Quantum well: | 1 | 2 |
| Quantum wire: | 2 | 1 |
| Quantum dot: | 3 | 0 |

TABLE 1.6: $D_f$ and $D_c$ for diferents systems.

### 1.8.1 Schrödinger's equation in quantum wells

#### The infinite quantum well

The one-dimensional potential well with infinite depth is the simplest confinement potential in quantum mechanics. It is an introductory-level text on quantum physics, as it is a very simple quantum system. It corresponds classically to the study of the displacement of the center of mass of a sphere in a tube with infinitely solid walls (see Figure 1.14).


FIGURE 1.14: Motion of a sphere in a tube.

Whatever the kinetic energy of the sphere, it will remain confined inside the tube. We have therefore potential energy which will be of the form shown in Figure 1.15.

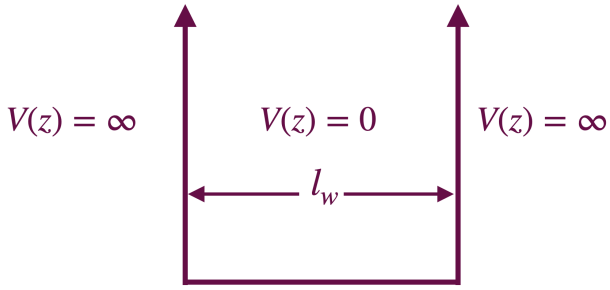


FIGURE 1.15: The one-dimensional infinite well confining potential.

The time-independent Schrödinger equation, based on the wave mechanics analogy to Hamilton's classical mechanics [46], describes the total energy as the sum of kinetic and potential energy $T$ and $V$ respectively, which are represented as eigenvalues of linear operators in wave mechanics:

$$T\psi + V\psi = E\psi \tag{1.81}$$

Where $\psi$ presents the state of the system, In analogy with classical physics, the kinetic energy operator $T$ for a constant mass particle can be written as follows,

$$T = \frac{P^2}{2m}, \tag{1.82}$$

where $P$ is the linear momentum operator defined by,

$$P = -i\hbar\nabla = -i\hbar(\frac{\partial}{\partial x}\vec{i} + \frac{\partial}{\partial y}\vec{j} + \frac{\partial}{\partial z}\vec{k}). \tag{1.83}$$

By substituting equations 1.82 and 1.83 in the Schrödinger equation 1.81, it becomes,

$$-\frac{\hbar^2}{2m}(\frac{\partial^2}{\partial x^2} + \frac{\partial^2}{\partial y^2} + \frac{\partial^2}{\partial z^2})\psi + V(x,y,z)\psi = E\psi. \tag{1.84}$$

We note that $V(x,y,z)$ is the potential energy of the system. In the case of a one-dimensional potential (quantum well) (Figure 1.15), the Schrödinger equation 1.84 in the **z-axis** becomes,

$$-\frac{\hbar^2}{2m}\frac{\partial^2}{\partial z^2}\psi(z) + V(z)\psi(z) = E\psi(z). \tag{1.85}$$

The particle cannot be in the region where $V = \infty$, because it would then have infinite energy, its probability density of presence must therefore be zero and we have $\psi(z) = 0$. In the region between $0$ and $l_w$, the potential is zero and the energy is only kinetic. The Schrödinger equation is written as,

$$-\frac{\hbar^2}{2m}\frac{\partial^2}{\partial z^2}\psi(z) = E\psi(z). \tag{1.86}$$

Which can be written as,

$$\frac{\partial^2}{\partial z^2}\psi(z) + \frac{2mE}{\hbar^2}\psi(z) = 0/ \tag{1.87}$$

Using de-Broglie's formula awe get $k^2 = \frac{2mE}{\hbar^2}$ with $E > 0$, then the Schrödinger equation is,

$$\frac{\partial^2}{\partial z^2}\psi(z) + k^2\psi(z) = 0. \tag{1.88}$$

The solution of the equation 1.88 is given by,

$$\psi(z) = Asin(kz) + Bcos(kz). \tag{1.89}$$

To determine A and B, we use the boundary conditions, and it is necessary to remember one of the properties that wave functions must have, that is continuity. This must be true, especially at the points $z = 0$ and $z = l_w$, which in this case yield the following constraint on the wave number:

$$k = \frac{n\pi}{l_w}, \tag{1.90}$$

where $n$, is a positive integer. Then,

$$E = \frac{\hbar^2}{2m}.\frac{n^2\pi^2}{l_w^2}. \tag{1.91}$$

It is noted that from equation 1.91 that:

- The energy is quantified; it depends on an integer $n$ that we call a "quantum number".
- The energy levels move away from each other when $n$ increases.
- The minimum energy is not zero. This has very important consequences in statistical physics and has no classical equivalent.
- When $l_w$ increases, the energy levels are tightened and when $l_w$ tends to infinity the quantization disappears.

The constant factor A remains unknown, and in order to determine it, we consider the normalization condition of the wave function, which gives,

$$A = \sqrt{\frac{2}{l_w}}. \tag{1.92}$$

Therefore,

$$\psi(z) = \sqrt{\frac{2}{l_w}}.sin(\frac{n\pi z}{l_w}). \tag{1.93}$$

Figure 1.16, shows the wave function plots for the first three possible values of the quantum number n.

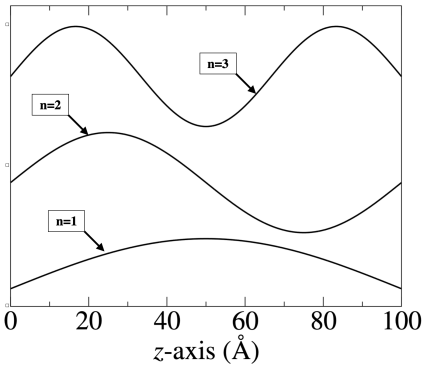


FIGURE 1.16: The wave function of a one-dimensional infinite well-confining potential.

### The finite quantum well

A one-dimensional finite well is a simple physical model to describe the potential distribution in a semiconductor material with a limited well depth (Figure 1.17).

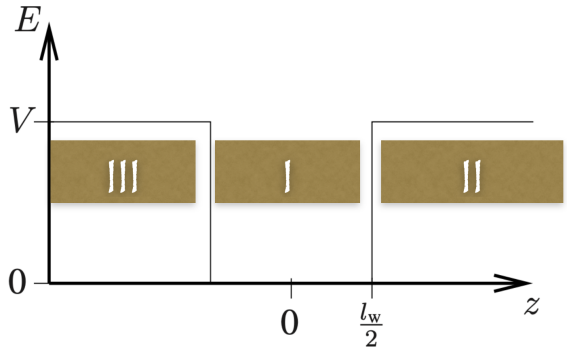


FIGURE 1.17: The one-dimensional finite well confining potential.

The Schrödinger equation can be written in this case for the semiconductor layers as follows,

$$-\frac{\hbar^2}{2m^*}\frac{\partial^2}{\partial z^2}\psi(z)+V\psi(z)=E\psi(z), \qquad z\leq -\frac{l_w}{2} \qquad (RegionIII) \tag{1.94}$$

$$-\frac{\hbar^2}{2m^*}\frac{\partial^2}{\partial z^2}\psi(z)=E\psi(z), \qquad -\frac{l_w}{2}\leq z\leq \frac{l_w}{2} \qquad (RegionI) \tag{1.95}$$

$$-\frac{\hbar^2}{2m^*}\frac{\partial^2}{\partial z^2}\psi(z)+V\psi(z)=E\psi(z), \qquad \frac{l_w}{2}\leq z \qquad (RegionII) \tag{1.96}$$

The solution for $E<V$, has the following bound state form,

$$\psi(z)=\begin{cases} Ce^{\kappa z}, & (RegionIII) \\ Acos(kz)+Bsin(kz), & (RegionI) \\ De^{-\kappa z}. & (RegionII) \end{cases} \tag{1.97}$$

With $k=\frac{\sqrt{2m^*E}}{\hbar}$ and $\kappa=\frac{\sqrt{2m^*(V-E)}}{\hbar}$.
The search for constants is more complicated than in the infinite well, and it is necessary to use the boundary conditions concerning the continuity of the function $\psi(z)$ and the continuity of its derivative.
These equations have two sorts of solutions, symmetric (even-parity) eigenstates defined as cosine waves and antisymmetric (odd-parity) states defined as sine waves.

- The even states (Figure 1.18):

$$\psi(z)=\psi(-z).$$

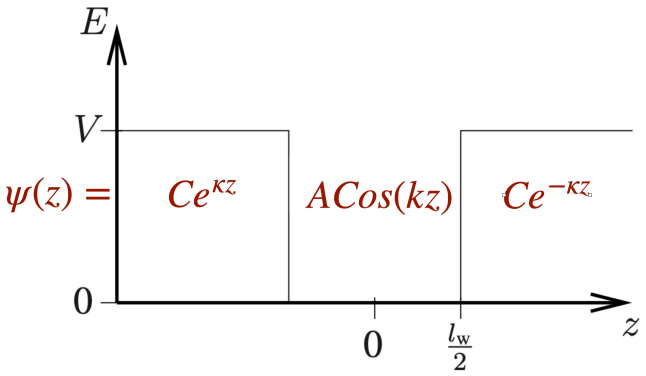


FIGURE 1.18: Solutions to the finite well potential for the even states.

The continuity of the function $\psi(z)$ and its derivative yield,

$$\kappa = k\,Tan(\frac{k\,l_w}{2}). \tag{1.98}$$

– The odd states (Figure 1.19):

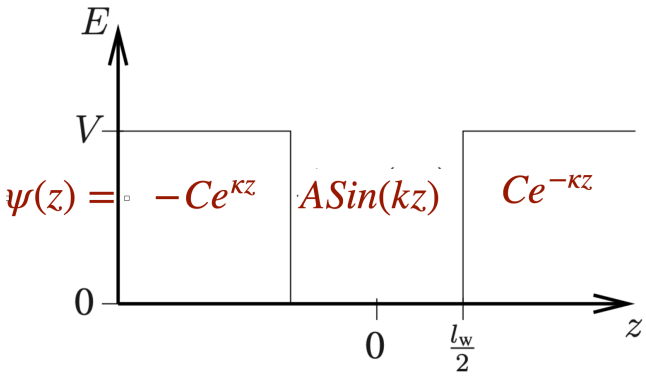


FIGURE 1.19: Solutions to the finite well potential for the odd states.

The continuity of the function $\psi(z)$ and the continuity of its derivative gives,

$$-\kappa = kcot(\frac{kl_w}{2}). \tag{1.99}$$

As we defined before that both $k$ and $\kappa$ are functions of the energy $E$, we have,

$$\begin{aligned} k^2+\kappa^2 &= \frac{2m^*E}{\hbar^2}+\frac{2m^*V}{\hbar^2}-\frac{2m^*E}{\hbar^2}, \\ k^2+\kappa^2 &= \frac{2m^*V}{\hbar^2}. \end{aligned} \tag{1.100}$$

Single variable equations can be solved in many ways and the commonly mentioned method in the literature for our specific case is 'graphical methods' [47, 48], in which we introduce

the variables $x$ and $y$ defined by,

$$x = \frac{kl_w}{2} \Rightarrow k = \frac{2x}{l_w},$$
$$y = \frac{\kappa l_w}{2} \Rightarrow \kappa = \frac{2y}{l_w}.$$

Equation (1.100) becomes,

$$x^2 + y^2 = \frac{mVl_w^2}{2\hbar^2}. \tag{1.101}$$

This equation (1.101 ) represents the equation of a circle with radius $R = \sqrt{\frac{m^* V l_w^2}{2\hbar^2}}$.
We have previously demonstrated for the even state (Eq.1.98) that

$$\begin{aligned} &\kappa = k\,Tan(\frac{k\,l_w}{2}),\\ &\frac{l_w}{2} \times \kappa = \frac{l_w}{2} \times k\,Tan(\frac{k\,l_w}{2}),\\ &y = x\,Tan(x). \end{aligned} \tag{1.102}$$

We also show for the odd state (Eq.1.99) that

$$\begin{aligned} &-\kappa = k\,cot(\frac{kl_w}{2}),\\ &\frac{l_w}{2} \times -\kappa = \frac{l_w}{2} \times kcot(\frac{kl_w}{2}),\\ &y = -x\,cot(x). \end{aligned} \tag{1.103}$$

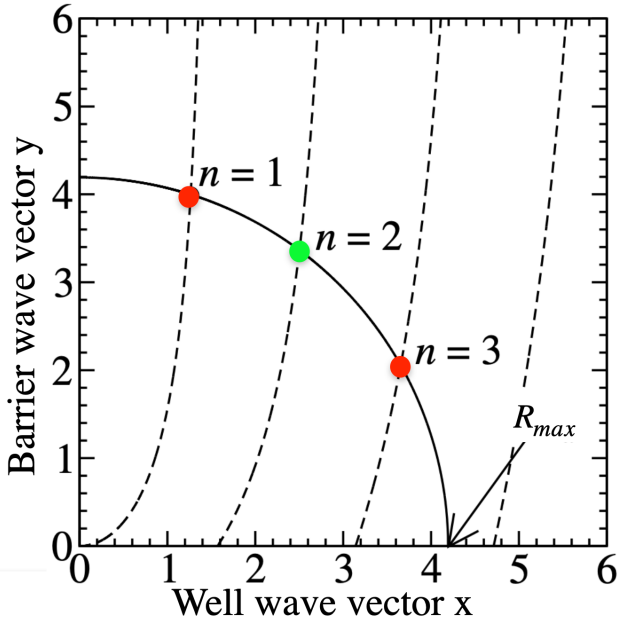


FIGURE 1.20: Scheme of the matching conditions for a bound state in a finite GaAs square well with $l_w = 200$ Å, and $V = 100meV$.

Figure (1.20) shows that the even solutions exist where the semicircle intersects with the dashed curves $y = x\,Tan(x)$ (red dots), while the odd solutions exist where the semicircle

intersects the dashed curves $y = -x\,cot(x)$ (green dot). The total number of solutions $N$ is the number of dashed curves that are intersected by the circle (red/green dots). The difference between the finite well and the infinite well is that in the finite well case, there is always at least one symmetric wave function, meaning that the wave function has the same value at the center of the well as it does at the walls. This symmetric wave function corresponds to the ground state energy, which is the lowest energy eigenstate. However, not all stationary states are symmetric, and there may be even and odd wave functions as well. In the case of an infinite well, the particle is confined to a region with infinite depth and width, and so it has an infinite number of possible energy states. These energy states are not equally spaced and the wave functions associated with them are sinusoidal within the well and is null outside of it. The wave functions are orthogonal, meaning that they are orthogonal over the entire range of the well. Unlike the finite well, all wave functions in an infinite well are symmetric and there is no notion of even or odd wave functions.
For $z > \frac{l_w}{2}$, we note that $\psi(z,t)$ is an evanescent wave that decreases over a characteristic distance $\delta$,

$$\psi(z,t) = \pm Be^{-\kappa z}\, e^{-i\frac{Et}{\hbar}}, \tag{1.104}$$

with $\delta = \frac{1}{\kappa} = \frac{\hbar}{\sqrt{2m^*(V-E)}}$,

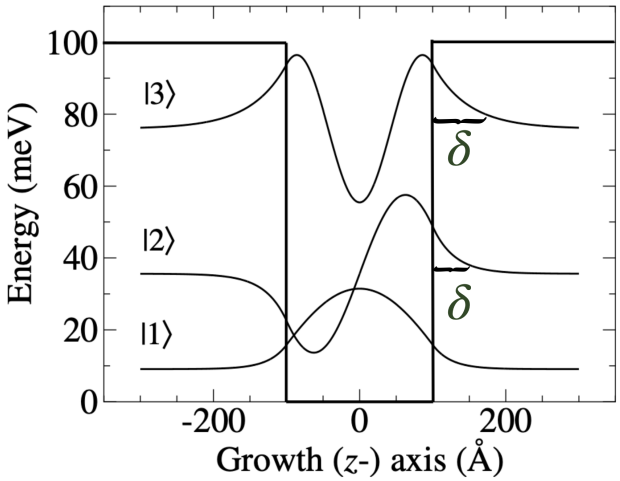


FIGURE 1.21: The wave function $\psi(z)$ for the first three energy levels of GaAs with $l_w = 200$ Å, $m^* = 0.067m_0$ , and $V = 100meV$.

We note other differences between the finite well and the infinite well:

- infinite well: the particle is confined.
- finite well: the particle has a non-zero probability of being outside the well (close to $\delta$), which gives an effective widening of the well ($l_w \to l_w + \delta$).

The only step left is to determine the amplitudes A and B of the wave function in the well and barrier regions, respectively.

- The even states:

We use the normalization of the state:

$$\int_{-\infty}^{+\infty} \psi(z).\psi^*(z)\, dz = 1. \tag{1.105}$$

Since the function is even, the previous equation (Eq. 1.105) becomes,

$$2\int_0^{+\infty}\psi(z).\psi^*(z)\,dz = 1, \tag{1.106}$$
$$2\times[\int_0^{\frac{l_w}{2}} A^2 cos^2(kz)dz + \int_{\frac{l_w}{2}}^{+\infty} C^2(e^{-\kappa z})^2 dz] = 1.$$

The solutions to the integrals are found by utilizing commonly accepted methods which yields,

$$\frac{A^2}{2k}[kl_w + sin(\frac{kl_w}{2})] + \frac{C^2}{\kappa}e^{-\kappa l_w} = 1. \tag{1.107}$$

Now, using the continuity of $\psi(z)$ and the continuity of its derivative, we obtain,

$$C = A\ cos(k\frac{l_w}{2})\ e^{\kappa\frac{l_w}{2}}. \tag{1.108}$$

Substituting this equation ( Eq. 1.108) into equation (Eq. 1.107) and rearranging A gives,

$$A = [\frac{l_w}{2} + \frac{1}{2k}\,sin(kl_w) + \frac{1}{\kappa}cos^2(k\frac{l_w}{2})]^{-\frac{1}{2}}. \tag{1.109}$$

The expression of the parameter $C$ is obtained using equation 1.108. A nearly identical calculation can be applied to the odd-parity states to get

$$A = [\frac{l_w}{2} - \frac{1}{2k}\,sin(kl_w) + \frac{1}{\kappa}sin^2(k\frac{l_w}{2})]^{-\frac{1}{2}}, \tag{1.110}$$

and,

$$C = A\ sin(k\frac{l_w}{2})\ e^{\kappa\frac{l_w}{2}}. \tag{1.111}$$

### 1.8.2 Schrödinger's equation in quantum wires

The general Schrödinger equation for an effective mass system can be written as,

$$-\frac{\hbar^2}{2m^*}\nabla^2\psi(x,y,z) + V(x,y,z)\psi(x,y,z) = E\psi(x,y,z), \tag{1.112}$$

where as before, $\psi(x,y,z)$ is the wave function of the electron, $m^*$ is the effective mass of the electron, $E$ is the energy of the electron, and $V(x,y,z)$ is the potential energy of the electron. In a quantum wire, it is possible to separate the movement along the length of the wire, similar to the in-plane dispersion discussed [16]. If the axis of the wire is taken along the $x$ direction, the total potential $V(x,y,z)$ can always be expressed as the sum of a 2D confinement potential and the potential along the wire:

$$V(x,y,z) = V(x) + V(y,z). \tag{1.113}$$

The wave function $\psi(x,y,z)$ can then be written as,

$$\psi(x,y,z) = \psi(x)\psi(y,z). \tag{1.114}$$

In this case, Schrödinger equation 1.112 becomes,

$$-\frac{\hbar^2}{2m^*}(\frac{\partial^2}{\partial x^2}+\frac{\partial^2}{\partial y^2}+\frac{\partial^2}{\partial z^2})\psi(x)\psi(y,z)+(V(x)+V(y,z))(\psi(x)\psi(y,z))=E\psi(x)\psi(y,z). \tag{1.115}$$

We express the energy as a combination of terms that relate to the two components of motion, we find that,

$$-\frac{\hbar^2}{2m^*}[\psi(y,z)\frac{\partial^2\psi(x)}{\partial x^2}+\psi(x)\frac{\partial^2\psi(y,z)}{\partial y^2}+\psi(x)\frac{\partial^2\psi(y,z)}{\partial z^2}] + \psi(y,z)V(x)\psi(x)+\psi(x)V(y,z)\psi(y,z)=(E_x+E_{y,z})\psi(x)\psi(y,z). \tag{1.116}$$

Equation 1.116 can now be reinterpreted by linking different kinetic and potential energies to the components $E_x$ and $E_{y,z}$, resulting in two separate equations as follows,

$$-\frac{\hbar^2}{2m^*}\psi(y,z)\frac{\partial^2\psi(x)}{\partial x^2}+\psi(y,z)V(x)\psi(x)=\psi(y,z)\,E_x\,\psi(x), \tag{1.117}$$

$$-\frac{\hbar^2}{2m^*}[\psi(x)\frac{\partial^2\psi(y,z)}{\partial y^2}+\psi(x)\frac{\partial^2\psi(y,z)}{\partial z^2}]+\psi(x)V(y,z)\psi(y,z)=\psi(x)E_{y,z}\psi(y,z), \tag{1.118}$$

$\psi(y,z)$ and $\psi(x)$ are not acted by any operator in equations 1.117 and 1.118 respectively, so they can be divided out. We note that the potential component of a quantum wire along the x-axis is equal to zero ($V(x)=0$), which is due to the idealized nature of the wire being infinitely long and perfectly conducting, with no impurities or defects present. This simplifies the mathematical analysis and provides a clearer understanding of the behavior of electrons within the wire. Therefore, the final separated equations of motion are presented as follows,

$$-\frac{\hbar^2}{2m^*}\frac{\partial^2\psi(x)}{\partial x^2}=E_x\,\psi(x), \tag{1.119}$$

$$-\frac{\hbar^2}{2m^*}[\frac{\partial^2\psi(y,z)}{\partial y^2}+\frac{\partial^2\psi(y,z)}{\partial z^2}]+V(y,z)\psi(y,z)=E_{y,z}\psi(y,z). \tag{1.120}$$

The first equation 1.119 can be satisfied by a plane wave of the form $e^{ik_x x}$, leading to the well-known dispersion relationship:

$$E_x=\frac{\hbar^2k_x^2}{2m^*}. \tag{1.121}$$

The second equation 1.120 represents the Schrödinger equation for a general cross-sectional wire. Specific solutions of this equation will be demonstrated, these particular solutions depend on the ability to break down the motion into separate and distinct components.

### Infinitely deep rectangular wires

Infinitely deep rectangular wires are quantum wires with a rectangular cross-section and an infinite depth. The width $L_z$ and height $L_y$ of the wire are assumed to be uniform, confining the electron motion to two dimensions (see Figure 1.22 ).

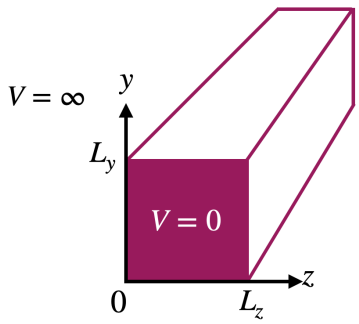


FIGURE 1.22: Scheme of a deep rectangular quantum wire.

As shown in Figure 1.22, the potential inside the quantum wire is equal to zero, while it is infinite outside the wire, which means that the Schrödinger equation can be defined only inside the wire. In this case, equation 1.120 becomes,

$$-\frac{\hbar^2}{2m^*}[\frac{\partial^2\psi(y,z)}{\partial y^2}+\frac{\partial^2\psi(y,z)}{\partial z^2}]=E_{y,z}\psi(y,z). \tag{1.122}$$

The shape of the potential in this equation makes it possible to separate $\psi(y,z)$ to $\psi(y)\psi(z)$, then equation 1.122 becomes,

$$-\frac{\hbar^2}{2m^*}[\psi(z)\frac{\partial^2\psi(y)}{\partial y^2}+\psi(y)\frac{\partial^2\psi(z)}{\partial z^2}]=E_{y,z}\psi(y)\psi(z). \tag{1.123}$$

We can replace the energy $E_{y,z}$ components with individual energy components $E_y$ and $E_z$, or $E_{y,z}=E_y+E_z$, then, equation 1.123 becomes,

$$-\frac{\hbar^2}{2m^*}\psi(z)\frac{\partial^2\psi(y)}{\partial y^2}-\frac{\hbar^2}{2m^*}\psi(y)\frac{\partial^2\psi(z)}{\partial z^2}=\psi(z)E_y\psi(y)+\psi(y)E_z\psi(z). \tag{1.124}$$

The following concludes the decoupling process,

$$-\frac{\hbar^2}{2m^*}\frac{\partial^2\psi(y)}{\partial y^2}=E_y\psi(y), \tag{1.125}$$

$$-\frac{\hbar^2}{2m^*}\frac{\partial^2\psi(z)}{\partial z^2}=E_z\psi(z). \tag{1.126}$$

Equations 1.125 and 1.126 are the same as those in the one-dimensional infinite quantum well. The two-dimensional Schrödinger equation has been separated into two one-dimensional equations, then the solutions are given by,

$$\psi(y)=\sqrt{\frac{2}{L_y}}\,sin(\frac{\pi n_y y}{L_y}), \tag{1.127}$$

and,

$$\psi(z)=\sqrt{\frac{2}{L_z}}\,sin(\frac{\pi n_z z}{L_z}). \tag{1.128}$$

The energy components $E_y$ and $E_z$ are given by,

$$E_y = \frac{\hbar^2 \pi^2 n_y^2}{2m^* L_y^2}, \tag{1.129}$$

$$E_z = \frac{\hbar^2 \pi^2 n_z^2}{2m^* L_z^2}. \tag{1.130}$$

Thus, the total energy $E_{y,z} = E_y + E_z$ is given by,

$$E_{y,z} = \frac{\hbar^2 \pi^2}{2m^*}(\frac{n_y^2}{L_y^2} + \frac{n_z^2}{L_z^2}). \tag{1.131}$$

**Circular cross-section wire**

Reflecting on the Schrödinger equation for the motion within the limited cross-sectional plane of a quantum wire, as previously stated in the equation 1.120 given by,

$$-\frac{\hbar^2}{2m^*}[\frac{\partial^2 \psi(y,z)}{\partial y^2} + \frac{\partial^2 \psi(y,z)}{\partial z^2}] + V(y,z)\psi(y,z) = E_{y,z}\psi(y,z). \tag{1.132}$$

Given the cylindrical symmetry of the quantum wire, as illustrated in Figure 1.23, it would appear to be beneficial to adopt polar coordinates to describe the cross-sectional motion.

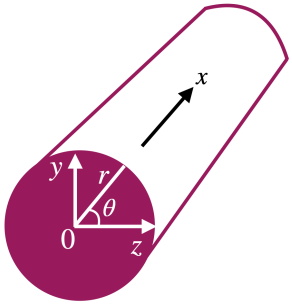


FIGURE 1.23: Scheme of a circular cross-section quantum wire.

The polar coordinates are defined by the modulus $r$ and angle $\theta$, and the corresponding Cartesian coordinates( $x$, $y$, and $z$) can then be defined by,

$$y = r\,sin\theta \qquad and \qquad z = r\,cos\theta, \tag{1.133}$$

$$r = \sqrt{y^2 + z^2}, \tag{1.134}$$

The wave function $\psi(y,z)$ can easily be expressed using the transformed variables $r$ and $\theta$. The wave function, typically, can exhibit periodic oscillations with respect to $\theta$ along the circular cross-section. In this scenario, the derivative of the wave function $\frac{\partial \psi}{\partial \theta}$ is equal to zero and the wave function can be represented as a function of $r$ only. As a result, the Schrödinger equation (1.120) can be simplified to,

$$-\frac{\hbar^2}{2m^*}(\frac{\partial^2}{\partial y^2} + \frac{\partial^2}{\partial z^2})\psi(r) + V(r)\psi(r) = E_r\psi(r). \tag{1.135}$$

We note that,

$$\frac{\partial}{\partial y}\psi(r) = \frac{\partial}{\partial r}\psi(r) \times \frac{\partial r}{\partial y}. \tag{1.136}$$

Hence,

$$\frac{\partial}{\partial y}\psi(r) = \frac{\partial}{\partial r}\psi(r) \times \frac{y}{r}. \tag{1.137}$$

The second derivative would be,

$$\frac{\partial}{\partial y}\frac{\partial}{\partial y}\psi(r) = \frac{\partial}{\partial y}[\frac{\partial}{\partial r}\psi(r) \times \frac{y}{r}], \tag{1.138}$$

$$= \frac{\partial^2}{\partial r^2}\psi(r) \times \frac{\partial r}{\partial y}\frac{y}{r} + \frac{\partial}{\partial r}\psi(r)\frac{\partial}{\partial y}(\frac{y}{r}), \tag{1.139}$$

$$= \frac{1}{r}\frac{\partial}{\partial r}\psi(r) - \frac{y^2}{r^3}\frac{\partial}{\partial r}\psi(r) + \frac{y^2}{r^2}\frac{\partial^2}{\partial r^2}\psi(r). \tag{1.140}$$

Using similar measure for $z$, hence,

$$(\frac{\partial^2}{\partial y^2} + \frac{\partial^2}{\partial z^2})\psi(r) = \frac{2}{r}\frac{\partial}{\partial r}\psi(r) - \frac{(y^2+z^2)}{r^3}\frac{\partial}{\partial r}\psi(r) + \frac{(y^2+z^2)}{r^2}\frac{\partial^2}{\partial r^2}\psi(r). \tag{1.141}$$

Using 1.134 equation 1.141 becomes,

$$(\frac{\partial^2}{\partial y^2} + \frac{\partial^2}{\partial z^2})\psi(r) = \frac{1}{r}\frac{\partial}{\partial r}\psi(r) + \frac{\partial^2}{\partial r^2}\psi(r). \tag{1.142}$$

The final form of Schrödinger equations 1.135 becomes,

$$-\frac{\hbar^2}{2m^*}(\frac{1}{r}\frac{\partial}{\partial r} + \frac{\partial^2}{\partial r^2})\psi(r) + V(r)\psi(r) = E_r\psi(r). \tag{1.143}$$

This equation cannot have a definitive answer in a general form, and therefore, one has to use either numerical or approximate methods to find a solution [16].

### 1.8.3 Schrödinger's equation in quantum dots

#### Quantum boxes

The particle in this model is trapped within a box that has a finite size, and the potential energy inside the box is considered to be zero, while it is assumed to be infinitely large outside the box. This means that the particle is free to move inside the box but cannot escape from the box (figure 1.24). We take into account an infinite potential that separates the interior of a box from the exterior. The three-dimensional Schrödinger equation inside the quantum box is given by,

$$-\frac{\hbar^2}{2m^*}(\frac{\partial^2}{\partial x^2} + \frac{\partial^2}{\partial y^2} + \frac{\partial^2}{\partial z^2})\psi(x,y,z) = E_{x,y,z}\psi(x,y,z). \tag{1.144}$$

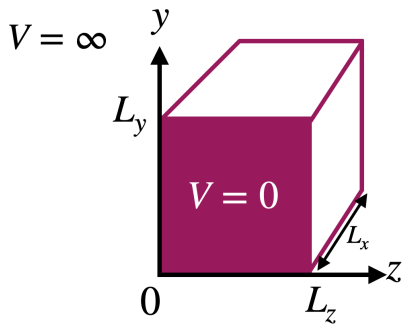


FIGURE 1.24: Scheme of a quantum box with side $L_x$, $L_y$, and $L_z$.

We note that $E_{x,y,z} = E_x + E_y + E_z$, in this case, Equation 1.144 can be decoupled into three equations given by,

$$-\frac{\hbar^2}{2m^*}\frac{\partial^2}{\partial x^2} = E_x\psi(x), \tag{1.145}$$

$$-\frac{\hbar^2}{2m^*}\frac{\partial^2}{\partial y^2} = E_y\psi(y), \tag{1.146}$$

$$-\frac{\hbar^2}{2m^*}\frac{\partial^2}{\partial z^2} = E_z\psi(z). \tag{1.147}$$

The solutions, in this case, are equivalent to those of an infinitely deep quantum well with widths $L_x$, $L_y$, and $L_z$ respectively. In a similar manner to the confinement energy in an infinitely deep quantum wire, as described in equation (1.131), the confinement energy within this quantum box can be calculated as follows,

$$E_{x,y,z} = \frac{\hbar^2\pi^2}{2m^*}\left(\frac{n_x^2}{L_x^2} + \frac{n_y^2}{L_y^2} + \frac{n_z^2}{L_z^2}\right). \tag{1.148}$$

### Spherical quantum dots

Spherical quantum dots are nanoscale structures that have a spherical shape (see Figure 1.25). Due to their small size, the electrons in a spherical quantum dot are confined in all three dimensions, leading to the quantization of their energy levels. The study is similar to that previously established for the quantum wire with a circular cross-section.

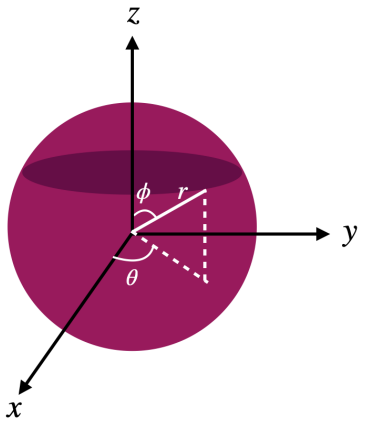


FIGURE 1.25: Schematic of a spherical quantum dot.

The Schrödinger equation inside the spherical quantum dot is given by,

$$-\frac{\hbar^2}{2m^*}(\frac{\partial^2}{\partial x^2}+\frac{\partial^2}{\partial y^2}+\frac{\partial^2}{\partial z^2})\psi(r)+V(r)\psi(r)=E_r\psi(r), \tag{1.149}$$

Where $E_r$ indicates the energy associated with the confinement, which is defined by,

$$r=\sqrt{x^2+y^2+z^2}. \tag{1.150}$$

Using the transformation from Cartesian to spherical polar coordinates (as detailed in the section of a circular cross-section wire), we can find that,

$$\frac{\partial^2}{\partial x^2}\psi(r)=\frac{1}{r}\frac{\partial}{\partial r}\psi(r)-\frac{x^2}{r^3}\frac{\partial}{\partial r}\psi(r)+\frac{x^2}{r^2}\frac{\partial^2}{\partial r^2}\psi(r). \tag{1.151}$$

Using similar measure for $y$ and $z$, therefore,

$$(\frac{\partial^2}{\partial x^2}+\frac{\partial^2}{\partial y^2}+\frac{\partial^2}{\partial z^2})\psi(r)=\frac{3}{r}\frac{\partial}{\partial r}\psi(r)-\frac{x^2+y^2+z^2}{r^3}\frac{\partial}{\partial r}\psi(r)+\frac{x^2+y^2+z^2}{r^2}\frac{\partial^2}{\partial r^2}\psi(r), \tag{1.152}$$

$$=\frac{2}{r}\frac{\partial}{\partial r}\psi(r)+\frac{\partial^2}{\partial r^2}\psi(r). \tag{1.153}$$

Substituting into equation 1.149 then yields,

$$-\frac{\hbar^2}{2m^*}(\frac{2}{r}\frac{\partial}{\partial r}+\frac{\partial^2}{\partial r^2})\psi(r)+V(r)\psi(r)=E_r\psi(r). \tag{1.154}$$

The analytical and numerical solutions of equation (1.154) have been investigated before ( for example in [49, 16]). The results of the calculations of the three energy levels with the lowest energy of a spherical GaAs quantum dot surrounded by a $Ga_{0.8}Al_{0.2}As$ finite barrier with a sharp boundary are presented. As shown in Figure 1.26, the confinement energy decreases as the size of the system increases, which is typical of confined systems.

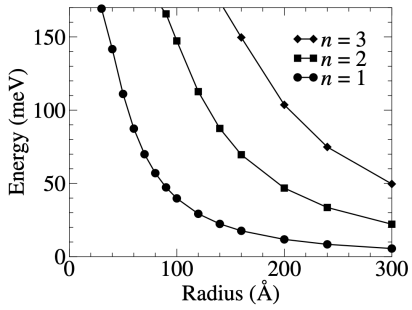


FIGURE 1.26: The energies in a spherical GaAs quantum dot.

The depicted figure 1.27 shows the radial components of the wave functions, which all exhibit a peak at the center of the potential. Moreover, as the principal quantum number $n$ increases, the number of nodes in the wave functions also increases. However, to gain a deeper understanding of the states, it is more insightful to examine the charge density.

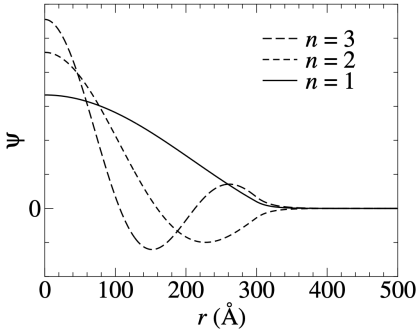


FIGURE 1.27: The wave functions of the three lowest-energy states in the 300 Åspherical GaAs quantum dot.

## 1.9 Zero-dimensional systems and their experimental realization

### 1.9.1 Quantum dots

Quantum dots fall under the category of nano-materials, where well-established quantum confinement effects occur. These nanomaterials are composed of semiconductors and have sizes in the order of nanometers [50]. Their optoelectronic features are defined by their size and shape, which influence their behavior accordingly. For instance, when a relatively large quantum dot, around $7nm$ in size, is excited by a photon with energy $h\nu$, it emits light in the orange or red wavelength range. On the other hand, a much smaller quantum dot ($2nm$) emits light with lower wavelengths in the green or blue range. As a result, Quantum dots capable of self-emission exhibit precise and diverse colors across a wide range of light intensities, making them ideal for next-generation large-scale displays. Their efficient light utilization and straightforward structure contribute to their widespread application in such display technologies. Figure 1.28 illustrates how the band gap of quantum dots changes with their size.

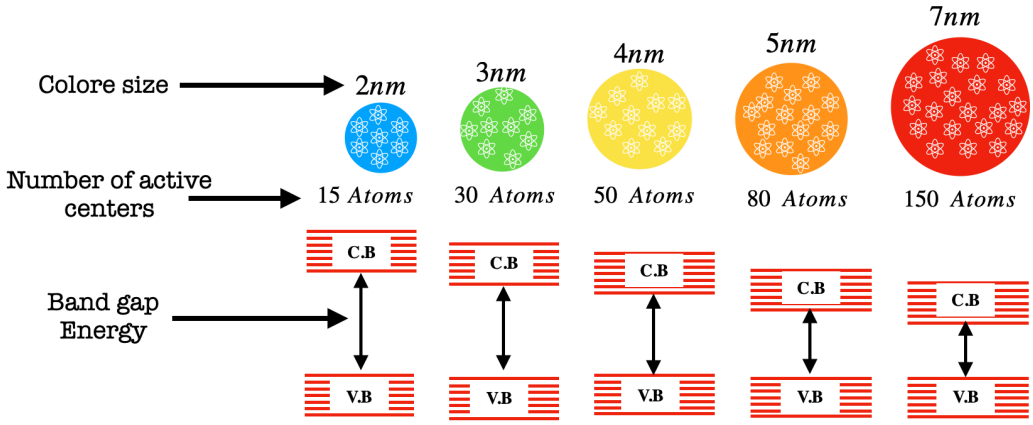


FIGURE 1.28: Band gap energy varies with the size of quantum dots.

### 1.9.2 Experimental realization of quantum dots

Quantum dots can be created using single-element materials, like Germanium or Silicon, as well as compound semiconductors such as CdSe, CdTe, PbS, and PbSe (section 1.1.1). Due to their discrete electronic states resembling those found in atoms and molecules, quantum dots

are often referred to as artificial atoms. Due to their unique spatial attributes, quantum dots display a multitude of distinct electronic, chemical, and optical properties rarely observed in other materials. Their size dependence allows for convenient tuning of these properties by controlling the quantum dot's size. Unlike the need to develop numerous processes for accurately synthesizing various sizes of monodisperse nanocrystal materials, quantum dots offer the advantage of being cost-effective. These exceptional qualities make quantum dots highly promising for a wide range of industrial and scientific research applications. Recently, there has been a growing interest in exploring quantum dots as evidenced by a rising number of studies dedicated to their realization. The first method used to create semiconductor hetero-structures with 3D confinement with lithographic patterning and etching of quantum well structures, using one of the various lithographic techniques, including optical holography and lithography, X-ray lithography, electron and focused ion beam lithography, scanning tunneling lithography, etc. Although the methods are different, the fundamental processes involved are fundamentally identical:

- Growing a layered structure and then applying another structure onto it.
- Generating a three-dimensional pattern while growing.

Although these methods are slow due to their serial processes, they still offer several benefits that make them attractive. They allow the creation of dots with almost any lateral shape, size, and arrangement, based on the resolution of the specific lithographic technique utilized. Additionally, they are generally compatible with modern, highly integrated semiconductor technology.
A noteworthy alternative approach involves the use of lithographic techniques to produce small electrodes on the surface of a quantum well. By applying a suitable voltage to the electrodes, a spatially modulated electric field is generated, which confines the electrons to a limited region. These confined areas, also known as electrostatically confined dots (or parabolic dots), derive their name from the fact that their shape can be approximated by a parabola with reasonable accuracy [51].
An alternative method for producing quantum dot structures involves self-assembly, which can be accomplished through either epitaxial or chemical synthesis techniques.
An epitaxial deposition involves placing semiconductor materials with slightly different lattice constants on top of each other. This process harnesses the resulting lattice strain to create arrays of three-dimensional islands or quantum dots.

Chemical synthesis offers an economical and rapid approach to creating highly crystalline clusters, consisting of a few hundred to tens of thousands of atoms in diverse shapes. These nanocrystals called colloidal dots are produced in a solution and are coated with organic molecules (ligands) that ensure their solubility and hinder aggregation.

**Self-assembled quantum dots:**

Self-assembled quantum dots (SAQD) are fabricated using a well-established technological process known as Stranski-Krastanov growth. This growth method involves epitaxy between materials with distinct lattice constants. As one material layer is grown on top of another, nanoscale islands form, due to the mismatch in lattice constants. This phenomenon occurs when the width of the layer, referred to as the wetting layer, exceeds a specific critical thickness. The two primary experimental techniques employed for epitaxial nanostructure growth are Molecular Beam Epitaxy (MBE) and Metalorganic Chemical Vapor Deposition (MOCVD) [52, 53].

Molecular beam epitaxy (MBE) is a thin-film deposition and growth technology that was developed in the 1960s. It was independently proposed by J.R. Arthur and J.C. Tsang in 1966 and later demonstrated by J.R. Arthur and A.Y. Cho in 1968 at Bell Laboratories [54]. MBE has since evolved into a highly sophisticated technique for the epitaxial growth of semiconductor materials with atomic-level precision. It is widely used in research and industrial settings to fabricate high-quality crystalline structures, including quantum dots, with controlled composition, size, and arrangement. MBE is conducted in a high vacuum or ultra-high vacuum environment, with pressures ranging from ($10^{-8}$ to $10^{-12}$ Torr). To achieve comparable impurity levels as other deposition methods, these low deposition rates necessitate a significantly improved vacuum. The absence of carrier gases, along with the ultra-high vacuum conditions, leads to the highest attainable purity of the grown films.
In solid-source MBE, elements like GaAs, in an exceptionally pure state, are individually heated within quasi-Knudsen effusion cells or electron-beam evaporators until they gradually sublimate. The resulting gaseous elements then condense on the wafer's surface, where they may react with each other to form compounds. For instance, in the case of gallium and arsenic, single-crystal gallium arsenide can be produced. When using evaporation sources like copper or gold, the gaseous elements that impinge on the surface can be adsorbed (after a period of time during which the impinging atoms move around the surface) or reflected. Additionally, atoms on the surface may also desorb (leave the surface). Precise control of the source temperature determines the rate at which the material impinges on the substrate surface, while the temperature of the substrate itself influences the rate of hopping or desorption. The term "beam" indicates that the evaporated atoms do not interact with each other or with gases in the vacuum chamber until they reach the wafer. This lack of interaction is due to the atoms' long mean free paths, allowing them to travel without significant collisions until they reach the substrate.

In this thesis, an important interest will be devoted to InAs/GaAs self-assembled quantum dots (SAQDs), due to their distinct characteristics, including excellent optical properties, significant orbital level splittings, and robust Coulomb correlation effects. These features make InAs QDs highly appealing for potential applications in quantum information processing devices.
The growth protocol for the site and size-controlled InAs quantum dots (QDs) was optimized by Hirakawa *et al* [1] using atomic force microscopy (AFM) assisted anodic oxidation. The study aimed to understand how the size of the QDs is influenced by the AFM-oxidation conditions. The results revealed that the site-controlled InAs QDs exhibited distinct facets, indicating their excellent crystalline quality.
Their research findings showed that they could consistently control the lateral size of the quantum dots (QDs) within a range of $40 - 180nm$ by adjusting the oxidation voltage ($V_{ox}$). For studying the transport properties of the site-controlled QDs, they created lateral single QD junction structures by directly depositing Au/Ti nanogap electrodes onto the QDs. In this process, they achieved a significant improvement in fabrication yield, with 80% of the nanojunctions containing single QDs, compared to only a few percent without site control.
In the fabricated single QD transistors, clear diamond-like patterns were observed in the Coulomb stability diagrams, signifying that these devices functioned as single electron transistors. Additionally, by controlling the size of the QDs, they were able to manipulate the charging energies and the orbital quantization energies across a wide range. These findings have implications for the potential applications of these site-controlled QDs in electronic devices and quantum information processing. To grow site-controlled quantum dots (QDs), the researchers first prepared alignment marks for AFM-anodic oxidation on semi-insulating oriented GaAs substrates using electron-beam lithography (EB lithography). After that, they

performed wet chemical etching on the patterned substrates, followed by a thorough cleaning process using a series of solvents and ozone ashing to eliminate any remaining resist. Next, they utilized an atomic force microscope (AFM) to create oxide dots in specific areas with dimensions of $4 \times 4\mu m^2$.

Figures (1.29a, 1.29b and 1.29c) illustrate the schematic representation of the site-controlled growth protocol for InAs quantum dots (QDs), and Figs.(1.29d, 1.29e and 1.29f) show corresponding atomic force microscopy (AFM) images of a sample surface during the process. The oxide dots were formed on a semi-insulating GaAs substrate at $V_{ox} = 50V$ and $T_{ox} = 30ms$. The substrate was positively biased with respect to the grounded tip [1, 55]. All oxide dots exhibited a consistent height of approximately $4nm$ and a base diameter of about $100nm$. The distance between the oxide dots was fixed at 250 nm. Following the chemical etching of the oxide dots, shallow nanoholes were obtained (1.29b, 1.29e), serving as nucleation sites for the subsequent growth of the InAs QDs. These nanoholes had the same diameter (around $100nm$) as the oxide dots and a depth of approximately $4nm$.

Afterwards, the sample was introduced into an MBE chamber, and thin native oxides were removed using Ga-assisted oxide desorption at temperatures ranging from $460 - 480^oC$. A $7nm$-thick GaAs buffer layer was then deposited on the patterned substrate at $510^oC$, followed by the deposition of InAs to grow the QDs.

In Figure 1.29f, AFM images of the QDs grown on the patterned substrate are shown. Selective dot nucleation occurred in the nanoholes, resulting in the formation of site-controlled QDs with a diameter of approximately $90nm$. The QDs grown using this method exhibited clear facets, indicating their excellent crystalline quality. Notably, the undesired dot nucleation was effectively suppressed.

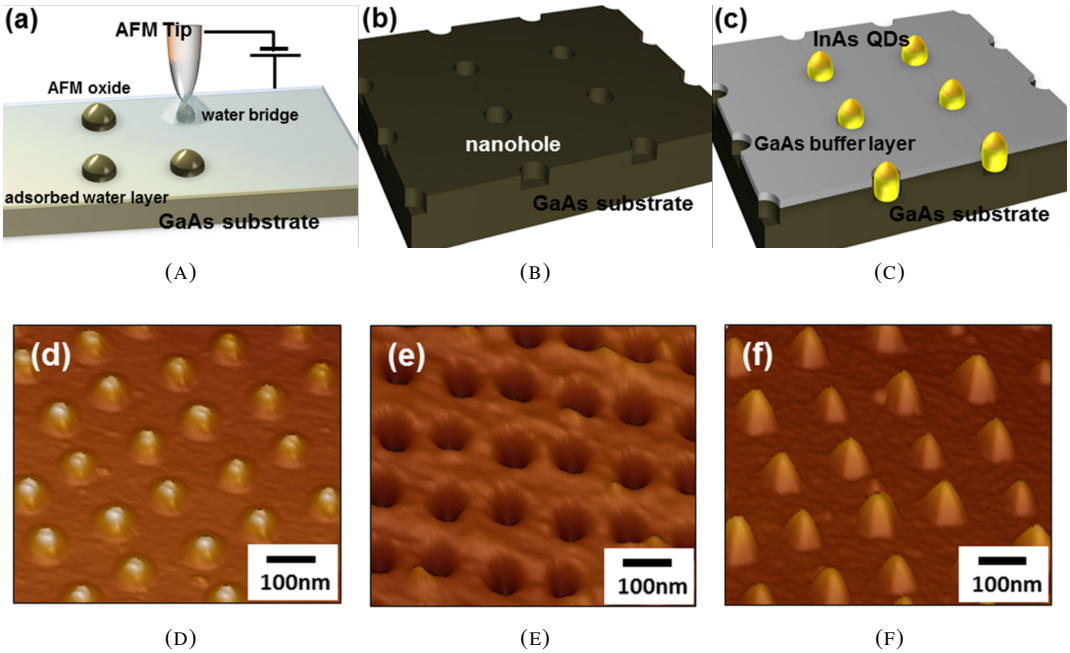


FIGURE 1.29: Schematics of the fabrication procedure for site-controlled InAs QDs using AFM assisted anodic oxidation [1].

Let's discuss how the size of site-controlled InAs quantum dots (QDs) can be manipulated by varying the conditions of AFM oxidation. Figures 1.30(a) and 1.30(b) display AFM images of the sample surfaces featuring oxide dots and etched nanoholes. It was observed

that $V_{ox}$ values below 20V did not lead to any significant oxidation. The figures reveal that increasing the voltage ($V_{ox}$) and extending the oxidation time ($T_{ox}$) result in broader and taller oxide dots due to the incorporation of oxygen atoms, leading to volume expansion. This outcome demonstrates the controllability of nanohole size through systematic adjustments in $V_{ox}$ and $T_{ox}$.

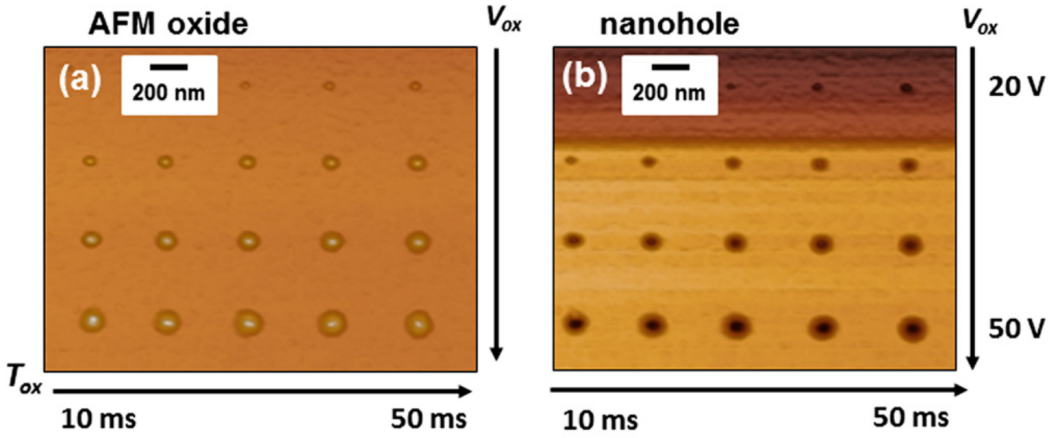


FIGURE 1.30: AFM images of oxide dots and nanoholes formed at various $V_{ox}$ and $T_{ox}$ [1].

**Colloidal quantum dots:**

In addition to SAQD fabricated using advanced deposition techniques, quantum dots can also be synthesized through crystal nucleation in colloidal solutions. The dots obtained using this method are referred to as colloidal nanocrystals (CN) or colloidal quantum dots (CQD) [56, 57].
The synthesis of CQDs involves three-component solutions consisting of organic surfactants, precursors, and solvents. The precursor compounds contain materials for dot nucleation. The solution medium is then heated to a sufficiently high temperature, causing the precursors to chemically transform into monomers. Nucleation occurs when these monomers reach a high enough supersaturation level, initiating the growth of nanocrystals. Temperature plays a critical role in the nucleation process, requiring it to be high enough to allow for rearrangement and annealing of atoms while still being low enough to facilitate crystal growth. Monomer concentration is also a crucial parameter, as a high enough concentration enables the formation of relatively small critical sizes, leading to even growth of most particles. This regime results in smaller particles growing faster than larger ones, leading to size monodispersivity. However, when the monomer concentration is depleted during growth, the critical size becomes larger than the average size present, resulting in highly heterogeneous nucleation.

Typical CQDs are composed of binary alloys such as *CdSe*, *CdS*, *InAs*, and *InP*, or ternary alloys such as $CdSe_xS_{1-x}$. These quantum dots can contain as few as 100 to $10^5$ atoms within their volume, with diameters ranging from 2 to 10 nanometers1.31. These nanocrystals are typically embedded within an insulating dielectric matrix, providing full confinement to carriers within the quantum dots.

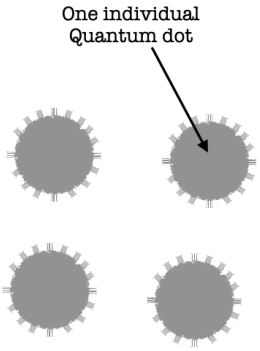


FIGURE 1.31: Diagram illustrating CQDs. Each nanocrystal typically adopts a spherical shape and is enclosed by ligands, acting as linker molecules that facilitate electronic coupling between adjacent dots.

Another group of quantum dots, in which quantum dots can be fabricated by additional confinement in a two-dimensional electron gas in specific semiconductor heterostructures. This confinement can be achieved either laterally by electrostatic gates or vertically by etching techniques [58, 59] (see Fig. 1.32). By varying the applied potential at the gates or applying an external magnetic field, the properties of these quantum dots can be controlled, often referred to as electrostatic quantum dots. These quantum dots are regarded as the leading candidates for the practical realization of quantum qubits [60, 61, 62]. Qubits are based on the spins of two electrons in two coupled electrostatically defined quantum dots. The coupling between these two dots can be tuned through gating, allowing the spins of two separated electrons to interact via a tunable exchange interaction.

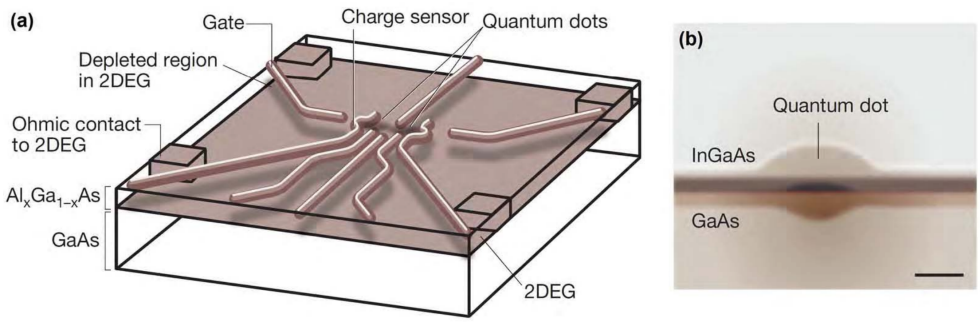


FIGURE 1.32: (a) A gate-defined double quantum dots, with 2DEG for two-dimensional electron gas. (b) A self-assembled quantum dot. Scale bar $\sim 5nm$. Extracted from Fig. 1 of Ref. [2].

### 1.9.3 Fabrication Modifications

Regarding the motivation for the research conducted on quantum dots, a fundamental question arises: "Why is it essential to conduct theoretical studies on quantum dots?" If quantum dots were heterostructures with highly variable and uncontrollable fabrication outcomes, then investing substantial effort in their theoretical modeling would seem futile. However, the ability to control and modify the growth outcomes opens up vast possibilities for their engineering and modeling, thereby justifying the effort put into theoretical studies. Over the

last decade, several advancements in growth processes have emerged, leading to the development of various types of self-assembled and colloidal nanocrystals with a certain level of geometrical and compositional tunability. Some of the cutting-edge modifications based on self-assembled quantum dots (SAQDs) are discussed below.

### Post-growth annealing of SAQDs

Upon completing the fabrication process, self-assembled quantum dots can undergo thermal annealing. The specifics of post-growth annealing are described in references [63, 64, 65]. The primary outcome of this process is the diffusion of In (indium) into the surrounding GaAs matrix, resulting in spatially increased, energetically reduced, graded, and tunable confinement of the quantum dots.

### Quantum posts

As a standard step in the fabrication of InAs/GaAs SAQDs [66], once the InAs islands are formed on the GaAs substrate, it becomes possible to deposit thin layers in an alternating superlattice of InAs and GaAs above them. However, due to potential strain concerns, In from the superlattice diffuses above the In islands, resulting in the formation of In-rich tubes positioned over each self-assembled In island. To complete the structure, a regular capping with a GaAs matrix is applied, leading to an overall outcome of a quantum rod structure, essentially an elongated quantum dot 1.33. The fabrication details can be found in references [3, 67, 68]. By meticulously controlling the growth parameters, the thickness of layers in the superlattice, and their deposition rate, it becomes feasible to precisely tune the In content within the tube and its height. Furthermore, additional growth control using different arsenic sources has been reported [69, 70].

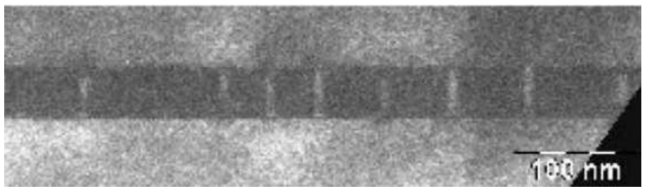


FIGURE 1.33: TEM image of quantum rods normal to the growth direction. The image is taken from Ref. [3].

### Quantum rings

SAQDs serve as the basis for Quantum rings, the process begins with self-organized InAs dots, and to create the rings, a brief annealing phase follows after covering the dots with a thin GaAs layer [71, 72]. These nanostructures offer stronger confinement compared to dots due to their modified shape. Recent findings [73] indicate that these structures demonstrate excellent intraband detection capabilities.

### Growth-kinetics control

By altering the growth kinetics while capping InAs islands with GaAs, it becomes feasible to adjust the dimensions of self-assembled quantum dots formed by InAs. To achieve this, adjustments are made to the growth sequence during the capping of InAs islands, allowing for tuning of the quantum dots' thickness and lateral dimensions while maintaining a constant wetting layer thickness [74].

### Core-shell CQDs

To mitigate the surface states in conventional CQDs, a method involves growing an additional layer of a distinct semiconductor of the same type around the initial CQD, creating what is known as core-shell CQDs. This fabrication process enhances the luminescence properties [75] by eliminating surface states that contribute to decoherence and non-radiative recombinations. These core-shell nanostructures are categorized into two types based on the band gap ratio of the core and shell materials.

In the first type structure, the conduction (valence) band edge in the core is positioned below (above) the values in the shell, resulting in the confinement of both electrons and holes in the core. On the other hand, second-type alignment leads to the confinement of only one type of carrier (either electrons or holes) in the core while the other remains unrestricted.

### CQD super-crystal

During the nucleation process, it is feasible to arrange CQDs in a self-assembled manner, forming a super-lattice structure [76, 77]. The monodispersity of CQDs allows for the creation of artificial solids consisting of well-defined sites composed of CQDs. To achieve favorable transport properties in these super-crystals, three primary directions in technology development are emphasized:

- Fabrication of monodispersed systems.
- Enhanced interdot coupling.
- Uniform high-level doping.

Despite significant advancements in technology, a considerable challenge still persists in obtaining CQD super-crystals with both satisfactory geometrical monodispersity and interdot coupling [78] (Figure 1.34).

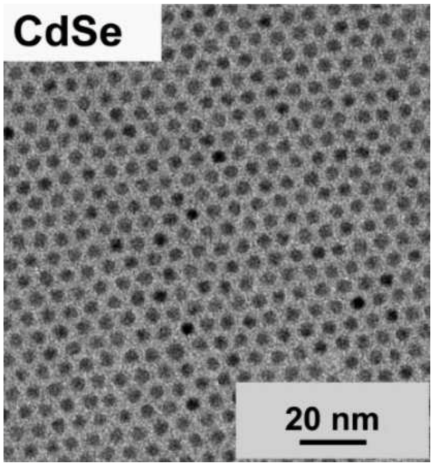


FIGURE 1.34: TEM image of CdSe CQD supercrystals.The image is taken from Ref. [4]

# Chapter 2

# Quantum information processing with quantum dots

## 2.1 Fundamentals of quantum information theory

### 2.1.1 Description of a quantum system

#### State space

In quantum mechanics, we describe the state of a system by a wave function $|\psi\rangle$, which includes information about the physical properties such as position, momentum, and energy. The state is associated with a complex vector in a Hilbert space $\mathcal{H}$. The wave function can be used to calculate the probability of observing a particular outcome when a measurement is made on the system. In order to represent a valid quantum state, the wave function must satisfy the following conditions:

- $|\psi(t)\rangle$ must be normalized, such that: $||\psi(t)||^2 = \langle\psi(t)|\psi(t)\rangle = 1$.
- The vector $|\psi(t)\rangle$ must have a single value.
- It is necessary for the wave function $|\psi(t)\rangle$ to have a finite amplitude within a finite interval.

#### Density matrix

The density matrix $\rho_s$ (or density operator) [79], is a mathematical construct in quantum mechanics employed to characterize the state of a quantum system that isn't in a pure state. It is a matrix that contains information about the probabilities of finding a system in different pure states. The density matrix is particularly advantageous for examining systems coupled to their environment, as it allows for the calculation of observables that take into account the effects of the environment on the system.

For a pure quantum state:

The density matrix is defined by

$$\rho_s = |\psi\rangle\langle\psi|. \tag{2.1}$$

Equation (2.1) satisfies several properties:

- The trace of the density matrix is equal to one ($Tr(\rho_s = 1)$), indicating the probability of measuring the system is $100\%$.
- Hermitian, which means that $\rho_s^\dagger = \rho_s$.

- Positive semi-definite, which means that all eigenvalues of the density matrix $\rho_s$ are non-negative.
- Projection operator: $\rho_s^2 = \rho_s \Rightarrow Tr(\rho_s) = 1$.

For a mixed quantum state:
For a mixed state, the density matrix is given by

$$\rho_s = \sum_{i=1}^{n} p_i |\psi_i\rangle\langle\psi_i|, \tag{2.2}$$

where $p_i$ is the probability of the system being in the pure state $|\psi_i\rangle$. Notice that $\sum_{i=1}^{n} p_i = 1$, and $p_i \geq 0$. Equation (2.2) represents the mixture of different pure states, and it is a way to account for the fact that we may not know exactly which pure state the system is in. In this case, the density matrix $\rho_s$ satisfies several important properties:

- The trace of the density matrix is equal to one $Tr(\rho_s) = 1$.
- Hermitian, which means that $\rho_s^\dagger = \rho_s$.
- Positive semi-definite, which means that all eigenvalues of the density matrix $\rho_s$ are non-negative.
- $Tr(\rho_s) \leq 1$, this property allows the ability to differentiate between a pure state and a mixed state, it is possible to calculate the degree of the mixture in a mixed state using this property [80].

### Wigner function

The Wigner function, named in honor of physicist Eugene Wigner [81], is a mathematical tool used in quantum mechanics to describe a system's quantum state in phase space. It takes the wave function of a quantum state and generates a quasi-probability distribution over the position and momentum of the system. Over the past few years, multiple works have tackled the quantification of quantum correlations by using the Wigner function in several quantum systems. Wigner's objective was to replace the wave function which appears in Schrodinger's equation with a probability distribution in phase space. The Wigner function is a measurable quantity, and it is a very well-behaved function, but nevertheless, it can also take negative values for a quantum state and therefore is a quasi-probability function. This negativity has played recently a significant role in quantum information theory. For a system described by the density matrix $\rho_s$, the Wigner function is defined by,

$$W(q,p) = \frac{1}{2\pi} \int_{-\infty}^{\infty} dy \; \mathrm{e}^{-ipy} \langle q + \frac{y}{2} | \rho | q - \frac{y}{2} \rangle. \tag{2.3}$$

With the appropriate change of variables, we find,

$$W(q,p) = \frac{1}{\pi} \int_{-\infty}^{\infty} dy \; \mathrm{e}^{2ipy} \langle q - y | \rho | q + y \rangle. \tag{2.4}$$

It should be noted that the Wigner function exhibits numerous properties, and we will outline the most significant ones below

- **Probability completeness:** The Wigner function should satisfy the normalization condition,

$$\int \int W(q,p) dq dp = 1. \tag{2.5}$$

- **Hermitian operators:** When the density matrix is Hermitian, the Wigner function takes only real values.
- **Linearity:** In the term of density states, the Wigner function is linear,

$$W(q,p)_{p_1\rho_1+p_2\rho_2+\ldots} = p_1 W_{\rho_2} + p_1 W_{\rho_2} + \ldots . \tag{2.6}$$

- **Fidelity:** The fidelity of a given state $\rho_s$ to any pure state $|\psi\rangle$ can be expressed in terms of the Wigner function as follows:

$$F^2 = (\sqrt{\langle\psi|\rho_s|\psi\rangle}^2 = \pi \int_{-\infty}^{\infty}\int_{-\infty}^{\infty} dq\, dp\, W(q,p) W_{|\psi\rangle\langle\psi|}(q,p). \tag{2.7}$$

- **Transpose operation:** The Wigner function in phase space represents the translation of the transposition of the density matrix in the following way,

$$W_{\rho_s^T}(q,p) = W_{\rho_s}(q,-p). \tag{2.8}$$

- **Purity:** The purity of a state is given by,

$$P = Tr(\rho_s^2) = 2\pi \int_{-\infty}^{\infty} dq\, dp\, W^2(q,p). \tag{2.9}$$

### The Qubit

A qubit [82] (short for a quantum bit) is the basic unit of quantum information, analogous to the classical bit in classical computing. However, while a classical bit can only take one of two values (0 or 1), a qubit can exist in a superposition of both states simultaneously. In other words, a qubit is a two-level quantum mechanical system that can exist in a coherent superposition of both $|0\rangle$ and $|1\rangle$ states at the same time, until it is measured or disturbed by its environment. The general expression of a qubit is given by,

$$|\psi\rangle = \alpha|0\rangle + \beta|1\rangle, \tag{2.10}$$

where $\alpha$ and $\beta$ are two complex numbers, satisfying the normalization condition

$$|\alpha|^2 + |\beta|^2 = 1. \tag{2.11}$$

In general, the pure state of a qubit can be written as a function of $\theta$ and $\Phi$ by,

$$|\psi\rangle = cos(\theta)|0\rangle + e^{i\Phi} sin(\theta)|1\rangle, \tag{2.12}$$

with $\frac{-\pi}{2} \leq \theta < \frac{\pi}{2}, \quad 0 \leq \Phi < 2\pi.$
The Bloch sphere illustrated in Figure 2.1, provides a geometric representation of the qubit defined in equation 2.12. In classical computing, if we have two bits, we will have four possible states given by 00, 01, 10, and 11. Similarly, a two-qubit system has four basic computational states denoted by $|00\rangle$, $|01\rangle$, $|10\rangle$, and $|11\rangle$. A pair of qubits can also exist in superpositions of these four states, such as the following state vector,

$$|\psi\rangle = \alpha_{00}|00\rangle + \alpha_{01}|01\rangle + \alpha_{10}|10\rangle + \alpha_{11}|11\rangle, \tag{2.13}$$

$$= \alpha_{00}\begin{pmatrix}1\\0\\0\\0\end{pmatrix} + \alpha_{01}\begin{pmatrix}0\\1\\0\\0\end{pmatrix} + \alpha_{10}\begin{pmatrix}0\\0\\1\\0\end{pmatrix} + \alpha_{11}\begin{pmatrix}0\\0\\0\\1\end{pmatrix}. \tag{2.14}$$

After a measurement, the state of the qubit is $|x\rangle$ ($x$ = 00, 01, 10 or 11), with a probability of $|\alpha_x|^2$.

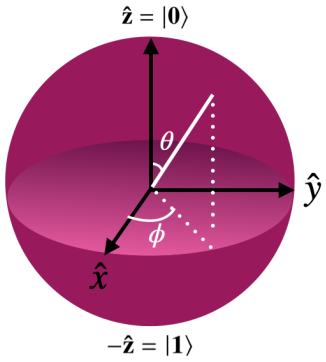


FIGURE 2.1: Bloch Sphere of a two-dimensional quantum system.

## 2.2 Information theory

### 2.2.1 Classical Information Theory

Before formally presenting the concept of information theory, introduced by Claude Shannon, it appears advantageous to briefly define what is first meant by information. Broadly speaking, information can be described as the data or knowledge that is exchanged, received, or manipulated. This can manifest in various ways such as text, images, sounds, numbers, symbols, and strings of bits, through communication channels governed by the principles of classical physics.

In 1948 Claude Shannon created his revolutionary mathematical theory of communication [83]. But, Shannon's theory identifies three levels of communication problems, The first level, the technical problem, deals with the accuracy of transmitting communication symbols through a channel. The second level, the semantic problem, concerns how precisely the transmitted symbols communicate the intended meaning. Finally, the third level, the effectiveness problem, deals with how well the received meaning can influence behavior in an intended manner.

To formalize the measurement of information, it is interesting to consider an example that illustrates this concept. Let $E$ be an event with probability $p$. The objective is to determine the amount of information conveyed by a message stating that this event has occurred. Intuitively, the measurement of the quantity of information provided by the message depends on the probability $p$. If the probability of event $E$ is higher before the message arrives, then the message conveys very little information. Therefore, the higher probability of the event $E$ coincides with the lower amount of information conveyed by a message announcing the occurrence of $E$.

Based on the previous situation, it is necessary for a function that expresses the amount of information received from a message to be decreasing with $p$. Let's assume that we want to measure the amount of information provided by event X, which is produced in a probabilistic experiment. To accomplish this, we define an "information function" $H(X = x)$ that satisfies the following conditions.

- The amount of information in the event $x$ with probability $p(x)$ can be quantified by the function $H(x)$. This function is inversely proportional to the improbability $p(x)$ such as,
$$H(x) = f(\frac{1}{p(x)}), \tag{2.15}$$
where $f$ is an increasing function.
- Since a certain event carries no information, $f(1)$ equals zero.
- The combined information from two independent events $x$ and $y$ is equivalent to the sum of their individual amounts of information,
$$\begin{aligned} H(x,y) &= f(\frac{1}{p(x,y)}), && (2.16)\\ &= f(\frac{1}{p(x)p(y)}), && (2.17)\\ &= f(\frac{1}{p(x)}) + f(\frac{1}{p(y)}), && (2.18)\\ &= H(x) + H(y). && (2.19) \end{aligned}$$

We can conclude from these properties that $f(\frac{1}{p(x)})$ is a logarithmic function in nature, with the base of the logarithm often being 2, which corresponds to the two values of "bit". As a result, the amount of information associated with the realization of an event $x$ is equal to,

$$H(x) = log(\frac{1}{p(x)}) = -log(p(x)). \tag{2.20}$$

**Shannon information**

Shannon created the idea of statistical entropy in the field of information theory. This was done to measure information loss and determine the maximum amount of information that can be transmitted. The concept of entropy was initially introduced in the second law of thermodynamics to study the process of evolution, in the third law of thermodynamics to describe the condition of zero entropy, and utilized in statistical physics to explain how the properties of atoms influence the physical properties of matter.
Shannon also studied the noise in a classical channel, based on the probability of occurrence (frequency) of letters in a text. According to Shannon's first source coding theorem, consider a signal source (transmitter) with $n$ symbols $(a_1, ..., a_n)$, and we note that $X$ is the random variable describing the information transmitted by the source. Figure 2.2 represents the steps of data transmission. The distribution probability is defined by,

$$p_i = P(X = x_i), \qquad i = 1, 2, ..., n. \tag{2.21}$$

It is observed that Shannon entropy is related to the probability distribution $p_1, ..., p_n$. It is defined by,

$$H(X) = -\sum_{i}^{n} p_i \log p_i. \tag{2.22}$$

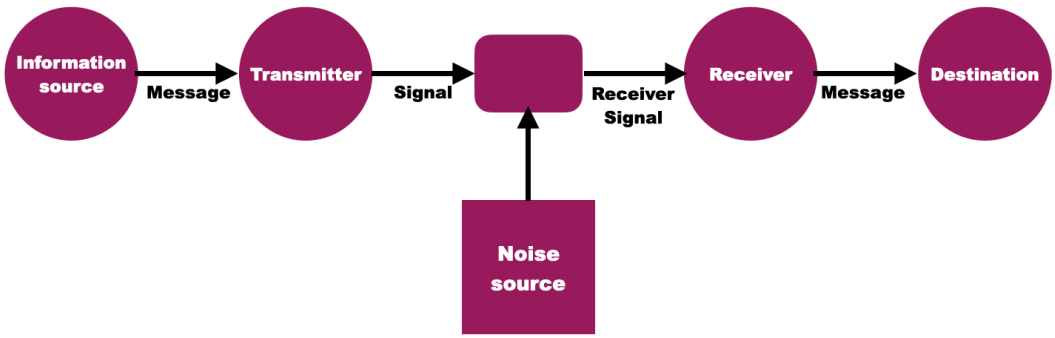


FIGURE 2.2: Shannon's model for message transmission.

It satisfies the following properties,

- The entropy represented by $H(X)$, is always non-negative ($H(X) \geq 0$). When the probability of one event is equal to 1, and all other probabilities are equal to 0, $H(X)$ equals 0, indicating that the occurrence of that event provides no information.
- For a fixed value of $n$, the maximum value of $H(X)$ is achieved when $p_i = \frac{1}{n}$ for all $i$.
- The concavity property states that $H(\lambda_1 p_1 + \lambda_2 p_2)$ is always less than or equal to $\lambda_1 H(p_1) + \lambda_2 H(p_2)$, where $\lambda_1$ and $\lambda_2$ are constants.

For example, in Figure 2.3, Shannon entropy is applied to a non-biased coin toss, where the probability of getting heads is $p_h = a$ and the probability of getting tails is $p_t = 1 - a$. In this case, the Shannon entropy formula reduces to $H(a) = -a\log(a) - (1-a)\log(1-a)$. The graph shows that $H(a)$ is at its maximum when the two outcomes are equally likely, with $p_h = p_t = \frac{1}{2}$. For $p_h > p_t$, the value of $H(a)$ decreases and eventually reaches zero when one outcome has a probability of one.

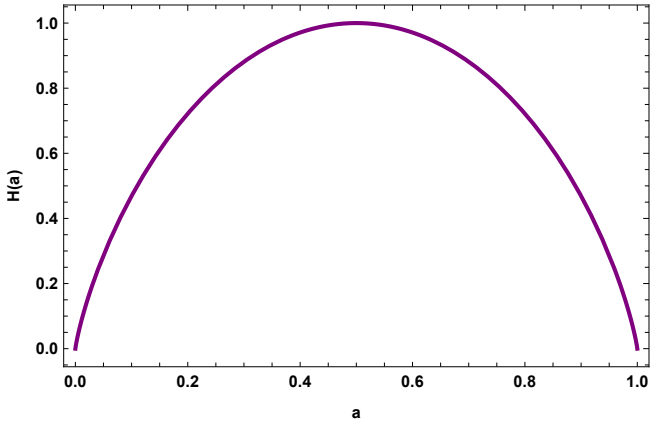


FIGURE 2.3: The Shannon entropy for the case of an unbiased coin toss.

This observation can be extended to situations with multiple events. More options result in more information, which tends to increase with a homogeneous probability distribution, such as when all events have equal probabilities. For instance, there is more information available when choosing from a set of one hundred words as opposed to a set of twenty words.

### Classical quantities

The important characteristics of Shannon entropy can be described in relation to other relevant concepts, including conditional entropy, relative entropy, and mutual information,

- **The joint entropy**: The joint entropy is a measure of the amount of uncertainty or randomness in a pair of random variables. More specifically, it is the entropy of the joint probability distribution of the two random variables $X$ and $Y$. It is denoted as $H(X,Y)$ and it can be written as,

$$H(X,Y) = -\sum_{x,y} p(x,y)\log(p(x,y)). \tag{2.23}$$

  The joint entropy does not depend on the order of the variables. In other words, the joint entropy is symmetric,

$$H(X,Y) = H(Y,X). \tag{2.24}$$

  It satisfies the inequality,

$$H(X,Y) \leq H(X) + H(Y). \tag{2.25}$$

  But if the two variables $X$ and $Y$ are independent, we obtain,

$$H(X,Y) = H(X) + H(Y). \tag{2.26}$$

- **Conditional entropy**: refers to the amount of uncertainty or randomness that remains in a random variable after we observe additional information. It is denoted as $H(X|Y)$ and it can be written as,

$$H(X|Y) = -\sum_{j}(p(y_j)\sum_{i} p(x_i|y_i)\log(p(x_i|y_j)), \tag{2.27}$$

$$= -\sum_{i,j} p(x_i,y_j)\log(p(x_i|y_j)). \tag{2.28}$$

  The marginal probabilities $p(x_i)$ and $p(y_j)$, represent the probability of $X$ and $Y$ occurring independently. On the other hand, the probability of $X$ and $Y$ occurring together is represented by $p(x_i,y_j)$, while $p(x_i|y_j)$ represents the probability of $X$ occurring given that $Y$ has already occurred. The conditional entropy is always non-negative and is only zero if the two variables $X$ and $Y$ are independent.

- **Relative entropy**: measures the difference between two probability distributions. It is calculated by summing the product of the probabilities of each outcome in one distribution with the logarithm of the ratio between the probabilities of the same outcome in the other distribution. It is denoted as $H(p||q)$ and it can be written as,

$$H(p(x)||q(x)) = \sum_{x\in\xi} p(x)\log(\frac{p(x)}{q(x)}). \tag{2.29}$$

  The relative entropy is always non-negative and is zero only if the two distributions are identical $p(x) = q(x)$.

- **Mutual information**: measures the amount of information that two random variables share. It is the difference between the entropy of a variable and its conditional entropy

given the other variable. It is denoted as $H(X:Y)$ and it can be written as,

$$H(X:Y) = \sum_x \sum_y p(x,y)\log(\frac{p(x,y)}{p(x)p(y)}), \tag{2.30}$$

$$= \sum_x p(x) \sum_y \frac{p(x,y)}{p(x)}[\log(\frac{p(x,y)}{p(x)} - \log(p(y)], \tag{2.31}$$

$$= \sum_x p(x) \sum_y p(Y=y|X=x)[\log p(Y=y|X=x) - \log p(y)], \tag{2.32}$$

$$= -\sum_x p(x)H(Y|X=x) - \sum_y p(y)\log p(y), \tag{2.33}$$

$$= H(Y) - H(Y|X), \tag{2.34}$$

$$= H(X) - H(X|Y). \tag{2.35}$$

The mutual information is always non-negative and is zero only if the two variables are independent. The different quantities mentioned earlier for two random variables A and B can be represented in the form of a Venn diagram (see Figure 2.4).

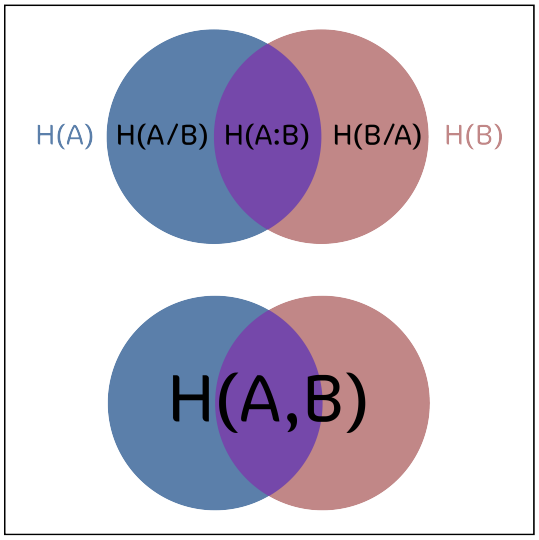


FIGURE 2.4: Venn diagram of different entropies.

### 2.2.2 Quantum Information Theory

The theory of quantum information (Von Neumann's theory) is a development of Shannon's information theory that utilizes the properties of quantum mechanics. This theory is based on basic definitions similar to Shannon's but with different properties.

#### Von Neumann entropy

The concept of Von Neumann entropy involves quantifying the information present in a quantum state, which is achieved by measuring the entropy of the probability distribution created

from the state $\rho_s$ through a projective measurement. Let $\rho$ be the density state of a quantum system X, the Von Neumann entropy is defined by this formula,

$$S(X) = S(\rho) = -Tr(\rho \log(\rho)). \tag{2.36}$$

We consider that $\lambda_i$ are the eigenvalues of $\rho$. In this case,

$$S(\rho) = S(\sum_i p_i |\psi_i\rangle\langle\psi_i|) = -\sum_{i=1}^{d} \lambda_i \log \lambda_i = H(p_i), \tag{2.37}$$

where $|\psi_i\rangle$ are the eigenvectors of the density state $\rho$.
We note that the Von Neumann entropy satisfies the following properties.

- **Non-negativity**: The Von Neumann entropy is always non-negative $(S(\rho) \geq 0)$.
- **Purity**: $S(\rho) = 0$ when $\rho$ is a pure state.
- **Additivity**: The Von Neumann entropy is additive for composite quantum systems, which means that
$$S(\rho \otimes \sigma) = S(\rho) + S(\sigma). \tag{2.38}$$
- **Invariance**: The Von Neumann entropy is invariant under unitary transformations, which means that
$$S(U\rho U^{-1}) = S(\rho). \tag{2.39}$$
- **Concavity**: The Von Neumann entropy is a concave function of the density matrix. That is if a density matrix is a convex combination of two other density matrices, then
$$S(\sum_i p_i \rho_i) \geq \sum_i p_i S(\rho_i), \tag{2.40}$$
with $p_i \geq 0$ and $\sum_i p_i = 1$.
- **Strong subadditivity**: We consider a state of a tripartite system ABC ($\rho_{ABC}$). Strong subadditivity implies that,
$$S(\rho_{ABC}) + S(\rho_B) \leq S(\rho_{AB}) + S(\rho_{BC}). \tag{2.41}$$
- **Triangle inequality**: We consider a bipartite system AB,
$$S(\rho_{AB}) \geq |S(\rho_A) - S(\rho_B)|. \tag{2.42}$$

**Quantum quantities**

Similar to the principles of classical information theory, we establish the concepts of quantum conditional entropy and quantum relative entropy, along with quantum mutual information.

- **The quantum conditional entropy** is defined for a composite system XY as follows:
$$S(X|Y) = S(X,Y) - S(Y). \tag{2.43}$$
The joint entropy $S(X,Y)$ is defined as $S(X,Y) = -Tr(\rho_{XY} \log(\rho_{XY}))$.

- **The relative entropy** of $\rho$ with respect to $\sigma$ can be defined as follows

$$S(\rho||\sigma) = Tr(\rho\log\rho) - Tr(\rho\log\sigma), \tag{2.44}$$
$$= -S(\rho) - Tr(\rho\log\sigma), \tag{2.45}$$

  where $\rho$ and $\sigma$ are two density operators. We note that the quantum relative entropy is always non-negative; this result is known as Klein's inequality. Furthermore, the quantum relative entropy is jointly convex in its arguments and is also monotonic.

- **The quantum mutual information** is defined by,

$$I(X:Y) = S(X) - S(X|Y), \tag{2.46}$$
$$= S(X) + S(Y) - S(X,Y). \tag{2.47}$$

  In a bipartite quantum system, mutual information is utilized to quantify the total correlations between the two subsystems.
  The quantum conditional entropy and the quantum mutual information are defined similarly as in Shannon's information theory. However, it should be noted that their interpretation may differ. Additionally, unlike the classical case, the quantum conditional entropy may not be positive and can be negative.

## 2.3 Quantum correlations

In this part, we shed some light to study the precious subjects of deep studies, which are quantum correlations, due to their fundamental resources in different quantum processing tasks [84, 85, 86, 87, 88].
The notion of quantum entanglement [89], introduced by Einstein $et\ al$ [90] and Schrödinger [91] in 1935, was considered a synonym for quantum correlations present in diverse quantum systems for a long time ([92, 93, 94, 95]). However, further investigations [89, 96, 97] have revealed the existence of additional quantum correlations beyond entanglement, necessitating the development of alternative measures to quantify all such correlations. In 2001, Ollivier and Zurek [96, 97], as well as Henderson et al [89] independently, proposed a new measure known as quantum discord, which encompasses all non-classical correlations. In this section, we present the measurement procedure of the two main ingredients of quantum correlations.

### 2.3.1 Entanglement

Entanglement is considered a new resource that can be utilized for performing tasks in quantum communications. It is a barrier between the quantum and the classical world. To study a quantum system, we consider a bipartite system composed of two subsystems A and B in the Hilbert spaces $\mathcal{H}_\mathcal{A}$ and $\mathcal{H}_\mathcal{B}$ respectively, such as that

$$\mathcal{H} = \mathcal{H}_\mathcal{A} \otimes \mathcal{H}_\mathcal{B}. \tag{2.48}$$

In the Hilbert space $\mathcal{H}$, one can find states that are either factorizable or non-factorizable. The latter being commonly known as entangled states. Suppose $|\psi\rangle_A$ and $|\psi\rangle_B$ represent states defined within the Hilbert spaces $\mathcal{H}_\mathcal{A}$ and $\mathcal{H}_\mathcal{B}$ respectively. The subsystems A and B are considered to be in an entangled state if,

$$|\psi\rangle_{AB} \neq |\psi\rangle_A \otimes |\psi\rangle_B. \tag{2.49}$$

To explain this concept, let's consider a system S in the state $|\psi\rangle$, composed of two subsystems $S_1$ and $S_2$, each having two levels represented by $|\psi\rangle_1$ and $|\psi\rangle_2$ respectively. Here's a simple example:

- The non-entangled (separable) states:

$$|\psi\rangle = |00\rangle + |01\rangle = |0\rangle \otimes (|0\rangle + |1\rangle). \tag{2.50}$$

- The entangled states:

$$|\psi\rangle = |00\rangle + |11\rangle \neq |\psi\rangle_1 \otimes |\psi\rangle_2. \tag{2.51}$$

A separable state can be represented as a tensor product of the states of its subsystems, while an entangled state cannot be factorized.

Consider a general scenario where two entangled states propagate in opposite directions **??**. These states possess a remarkable characteristics. When a measurement is carried out on one of the states on a specific basis, the measurement outcome of the other state on the same basis is always entirely determined by the result of the first measurement. This intriguing behavior might lead one to believe that information from the first state instantaneously influences the second state (i.e., surpassing the speed of light), thereby contradicting the principles of relativity (which states that nothing can exceed the speed of light). This phenomenon of entanglement is famously known as the EPR paradox [90].

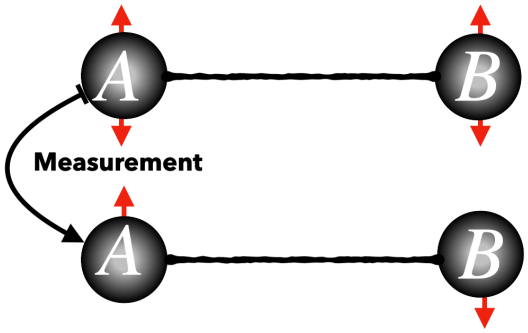


FIGURE 2.5: Two entangled states propagate in opposite directions.

For example, the most famous entangled states are Bell states, which are maximally entangled states. Consider the states $|\phi^{\pm}\rangle$ and $|\phi^{\pm}\rangle$, defined in $\mathcal{H}_{\mathcal{AB}}$ as

$$|\phi^{\pm}\rangle = \frac{1}{\sqrt{2}}(|00\rangle \pm |11\rangle), \tag{2.52}$$

$$|\psi^{\pm}\rangle = \frac{1}{\sqrt{2}}(|01\rangle \pm |10\rangle). \tag{2.53}$$

These states are also referred to as $EPR$ pairs or Bell states, forming an orthonormal basis of the state space. Now, before delving into the specifics of measuring entanglement, it is important to present the essential conditions that any measure of entanglement $E(\rho)$ must meet.

1. $E(\rho) \geq 0$, the equality holds when $\rho$ is separable.

2. $E(\rho)$ is invariant under local unitary operations, which means that the amount of entanglement in a state should remain unaffected by a local change of basis,

$$E(\rho) = E(U \otimes V \rho U^{\dagger} \otimes V^{\dagger}), \tag{2.54}$$

where U and V are unitary.

3. $E(\rho)$ does not increase under local operations and classical communication (LOCC).

4. $E(\rho)$ does not increase under different preparation of $\rho$, which means that,

$$\sum_i p_i E(\rho_i) \geq E(\sum_i p_i \rho_i). \tag{2.55}$$

**Bipartite entanglement**

Several measures of entanglement have been proposed for composite systems, particularly concurrence [98, 99, 100, 101], entanglement of formation [102, 103], and negativity [104, 105].

- **Concurrence:**

For a two-qubit system, the most commonly used measure of bipartite entanglement is concurrence, which was introduced by Wootters, and is defined for a pure state $\rho = |\psi_i\rangle\langle\psi_i|$ by,

$$C(\psi) = |\langle\psi||\tilde{\psi}\rangle|, \tag{2.56}$$

where $|\tilde{\psi}\rangle = \sigma_y|\psi^*\rangle$, $\sigma_y$ represents the Pauli matrix:

$$\sigma_y = \begin{pmatrix} 0 & -i \\ i & 0 \end{pmatrix}. \tag{2.57}$$

For a mixed state $\rho = \sum_i p_i|\psi_i\rangle\langle\psi_i|$, the concurrence is defined by,

$$C(\rho) = Max\left\{0, \lambda_1 - \lambda_2 - \lambda_3 - \lambda_4\right\}, \tag{2.58}$$

where $\lambda_1$ ,$\lambda_2$ ,$\lambda_3$ and $\lambda_4$ are the non-negative eigenvalues of the matrix $\rho\widetilde{\rho}$ arranged in decreasing order. $\widetilde{\rho}$ is the 'Spin Flipped' density matrix defined by,

$$\widetilde{\rho} = (\sigma_y \otimes \sigma_y)\rho^*(\sigma_y \otimes \sigma_y). \tag{2.59}$$

with $\rho^*$ is the complex conjugate of $\rho$ in the standard basis.

- **Entanglement of formation:**

For a pure bipartite state $|\psi\rangle_{AB}$, the Von Neumann entropy of the reduced density operator $\rho_A$ ($\rho_B$) can be used to quantify the entanglement,

$$\begin{aligned} E(|\psi\rangle_{AB}) = S(\rho_A) &= -\sum_i \lambda_i^A \log_2 \lambda_i^A, \\ &= S(\rho_B) = -\sum_j \lambda_j^B \log_2 \lambda_j^B, \end{aligned} \tag{2.60}$$

where $\lambda_i^A$ and $\lambda_j^B$ represents the eigenvalues of $\rho_A$ and $\rho_A$ respectively.
The entanglement presented above can be defined as a function of concurrence $C$,

$$E(\psi) = H(\frac{1}{2}(1+\sqrt{1-C^2})), \tag{2.61}$$

where $H(x)$ denotes the binary entropy given as $H(x) = -x\log_2(x) - (1-x)\log_2(1-x)$. The function $E(\psi)$ exhibits a monotonic increase from 0 to 1 as the concurrence $C$ varies within the range of 0 to 1. Therefore, the concurrence serves as a reliable indicator of the level of entanglement. Specifically, when $C = 0$ the state is deemed separable, but when $C = 1$ the state is maximally entangled.
For a mixed state, the quantification of entanglement of formation is defined as the average entanglement of the pure states, which is minimized by considering all possible decompositions:

$$E(\rho) = min \sum_i p_i E(\psi_i). \tag{2.62}$$

- **Bipartite negativity:**

Bipartite negativity is a measure of entanglement based directly on the separability criterion known as positive partial transpose. It is defined as follows

$$N(\rho) = \frac{\left|\left|\rho^{T_i}\right|\right| - 1}{2}, \tag{2.63}$$

where $||\rho^{T_i}|| = Tr\sqrt{(\rho^{T_i})^+(\rho^{T_i})}$ represents the partial transpose norm.

**Tripartite entanglement**

- **Genuine tripartite entanglement:**

In the context of a three-part system (A, B, and C), the state A is considered separable with respect to the bi-partition (A/BC) if it can be represented as a combination of product states involving subsystems A and BC.

$$\rho_{A/BC}^{\text{sep}} = \sum_j q_j |\phi_A^j\rangle\langle\phi_A^j| \otimes |\phi_{BC}^j\rangle\langle\phi_{BC}^j|, \tag{2.64}$$

with $q_j \geq 0$ and $\sum q_j = 1$, similarly, the separable states for the other two bipartitions are $\rho_{\text{sep}}$ (B/AC) and $\rho_{\text{sep}}$ (C/AB):

$$\rho_{B/AC}^{\text{sep}} = \sum_j q_j |\phi_B^j\rangle\langle\phi_B^j| \otimes |\phi_{AC}^j\rangle\langle\phi_{AC}^j|, \tag{2.65}$$

$$\rho^{\text{sep}}_{C/AB} = \sum_j q_j |\phi^j_C\rangle\langle\phi^j_C| \otimes |\phi^j_{AB}\rangle\langle\phi^j_{AB}|. \tag{2.66}$$

A state is considered biseparable if it can be represented as a combination of states that are separable with respect to different bi-partitions:

$$\rho^{\text{bs}} = p_1\rho^{\text{sep}}_{A/BC} + p_2\rho^{\text{sep}}_{(B/AC)} + p_3\rho^{\text{sep}}_{(C/AB)}. \tag{2.67}$$

On the other hand, a state is classified as genuinely multipartite entangled if it is neither separable nor biseparable.

- **Tripartite negativity:**

The entanglement between the three-qubit system ABC can be detected using the negativity $N$, defined as follows [105]:

$$N(\rho^{T_C}) = \sum_i \left|\lambda_i(\rho^{T_C})\right| - 1, \tag{2.68}$$

where $\rho^{T_C}$ is the partial transpose of $\rho$ with respect to the subsystem C, and $\lambda_i(\rho^{T_C})$ are the eigenvalues of $\rho^{T_C}$. The negativity can also be interpreted as the sum of the absolute values of the negative eigenvalues of $\rho^{T_C}$ [105], and it depends on the subsystem on which we perform the partial transpose of $\rho$.

If the negativity is greater than zero ($N > 0$), we can infer the presence of entanglement between subsystem C and subsystem AB. However, it should be noted that if there is entanglement between subsystems C and AB, the negativity is not necessarily greater than zero. Hence, a modified form of negativity has been defined [106]:

$$N^3(\rho) = \sqrt[3]{N(\rho^{T_A})N(\rho^{T_B})N(\rho^{T_C})}, \tag{2.69}$$

where $N^3(\rho)$ will be non-zero only when the entanglement is shared among all three subsystems (complete tripartite entanglement). However, zero negativity does not necessarily imply the absence of entanglement, except for pure states. Furthermore, it is worth noting that tripartite negativity cannot distinguish between genuine tripartite entangled states and biseparable states in a generalized sense [106, 107].

Note that for tripartite systems that are symmetrical under any interchange of their qubits, the tripartite negativity and the negativity always coincide:

$$N_3(\rho) = N(\rho^{T_A}) = N(\rho^{T_B}) = N(\rho^{T_C}). \tag{2.70}$$

### N-partite entanglement

Taking into account the challenges arising from the absence of a well-established entanglement measure for systems extending beyond the 2×2 and 2×3 dimensions because of the concept of Positive Partial Transposition (PPT) and its significance in characterizing entanglement. In lower-dimensional systems, such as $2 \times 2$ (two qubits) and $2 \times 3$ (qubit-qutrit), entanglement can be quantified and characterized using measures like concurrence or entanglement entropy. These measures work effectively because they align with the key property that all entangled states must exhibit: non-positive partial transposition. Positive Partial Transposition (PPT) is a necessary condition for separability in bipartite quantum systems.

In simpler terms, if a quantum state has a positive partial transpose, it is separable and not entangled. This property is well-established and provides a clear criterion for distinguishing between separable and entangled states in lower-dimensional systems. However, as the dimensionality of the quantum system increases, the relationship between entanglement and (PPT) becomes more intricate. In higher-dimensional systems, the (PPT) criterion alone is not sufficient to capture all aspects of entanglement. Complex multipartite and multi-dimensional entangled states can have positive partial transpositions, making it challenging to use (PPT) as a straightforward measure of entanglement. To circumvent these challenges, many studies [108, 109, 110, 111, 112, 113] have shifted their focus toward exploring lower bounds of entanglement in specific dimensions. The most important of these lower bounds is the lower bound of Li $et\ al.$ [114] which is valid for any dimension or partition and can serve as a witness of entanglement. When a lower bound of entanglement is non-zero, it indicates the presence of some form of entanglement within the quantum state under examination. This property makes lower bounds a powerful tool for detecting and characterizing entanglement, even in cases where traditional measures may falter due to the intricacies of higher-dimensional systems.

For an arbitrary $N$-partite state $\rho \in \mathcal{H} = \mathcal{H}^d \otimes ... \otimes \mathcal{H}^d$ , the lower bound of concurrence is defined by

$$\tau_N(\rho) = \frac{d}{2m(d-1)} \sum_p \sum_{\alpha\beta} (C^p_{\alpha,\beta})^2, \tag{2.71}$$

with $m = 2^{N-1} - 1$, $\sum_p$ stands for the summation over all possible combinations of the indices $\alpha\beta$, $C^p_{\alpha\beta} = max\{0, \lambda(1)^p_{\alpha\beta} - \lambda(2)^p_{\alpha\beta} - \lambda(3)^p_{\alpha\beta} - \lambda(4)^p_{\alpha\beta}\}$, where $\lambda(i)^p_{\alpha\beta}$ are the square roots of the four nonzero eigenvalues, in decreasing order of the non-Hermitian matrix $\sqrt{\rho\tilde{\rho}_{\alpha\beta}}$, with $\tilde{\rho}_{\alpha\beta} = (L_\alpha \otimes L_\beta)\rho^*(L_\alpha \otimes L_\beta)$, and $L_\alpha$ and $L_\beta$ being the generators of $SO(d)$.

In essence, these lower bounds of entanglement not only address the challenges presented by the absence of a universal entanglement measure but also provide a valuable framework for understanding and quantifying entanglement in various dimensions like in [115].

### 2.3.2 Quantum discord

The quantum discord [96] is a measure of the non-classical correlations between two subsystems of a quantum system. For a bipartite system AB, it is defined as the difference between two alternative quantum versions of two classically equivalent expressions of the mutual information,

$$D(\rho_{AB}) = I(\rho_{AB}) - C(\rho_{AB}), \tag{2.72}$$

where $I(\rho_{AB})$ and $C(\rho_{AB})$ are respectively, the mutual information and the classical correlations of the composite system $\rho_{AB}$. They are defined respectively by,

$$I(\rho_{AB}) = S(\rho_A) + S(\rho_B) - S(\rho_{AB}), \tag{2.73}$$

and

$$C(\rho_{AB}) = Max[S(\rho_A) - S(\rho_{AB}/\left\{\Pi^j_B\right\})], \tag{2.74}$$

with the Von Neuman entropy $S(\rho)$ is defined in (2.36) and (2.37), $\rho_A$ and $\rho_B$ are the reduced density matrices of the composite system $\rho_{AB}$. In equation 2.74 the conditional entropy is given by $S(\rho_{AB}/\left\{\Pi^j_B\right\}) = \sum_j P_j S(\rho_{A/j})$ with $\left\{\Pi^j_B\right\}$ being the complete set of orthonormal projection operators that act only on the second subsystem B, $\rho_{A/j} = Tr(\frac{\Pi^j_B \rho_{AB} \Pi^j_B}{P_j})$) is the resulting state of the first subsystem A, and $P_j = Tr_{AB}(\Pi^j_B \rho_{AB} \Pi^j_B)$

is the probability to obtain the outcome $j$.

The set of local measurement operators $\left\{\prod_B^j\right\} \equiv \{|\Pi_1\rangle\langle\Pi_1|, |\Pi_2\rangle\langle\Pi_2|\}$ can be easily constructed using the following states:
$|\Pi_1\rangle = \cos\theta|+\rangle + e^{i\Phi}\sin\theta|-\rangle$ and $|\Pi_2\rangle = \sin\theta|+\rangle - e^{i\Phi}\cos\theta|-\rangle$, with $\theta \in [0,\pi]$ and $\Phi \in [0, 2\pi]$.
Therefore, the quantum discord capturing all quantum correlation is defined as [116]

$$\begin{aligned} D(\rho_{AB}) &= I(\rho_{AB}) - Max[S(\rho_A) - S(\rho_{AB}/\left\{\Pi_B^j\right\})], \\ &= S(\rho_B) - S(\rho_{AB}) + Min_{\{\Pi_B^j\}}[S(\rho_{AB}/\left\{\Pi_B^j\right\}]. \end{aligned} \tag{2.75}$$

It turns out that conditional entropy minimization is the main difficulty in finding an analytic expression for quantum discord present in arbitrary states. Indeed, the procedure of calculation of this later is not easy for all states and the exact analytical expressions are found only in a limited number of cases, and the most general approach until now was obtained for the so-called X-states. Here, the density matrix of our system is written in the form of these states. In fact, the method given by C.Z Wang *et al* [117] can be used to calculate the quantum discord. Hence, this later can be defined by the following expression [117],

$$D(\rho_{AB}) = Min[QD_1, QD_2]. \tag{2.76}$$

Where

$$QD_j = H(\rho_{11} + \rho_{33}) + \sum_{k=1}^{4} \lambda_k Log_2(\lambda_k) + Dj.$$

Here $D_1 = H(\eta)$ and $D_2 = -\sum_{j=1}^{4} \rho_{jj} Log_2(\rho_{jj}) - H(\rho_{11} + \rho 33)$,
with $\eta = \frac{1+\sqrt{[1-2(\rho_{33}+\rho_{44})]^2+4(|\rho_{14}|+|\rho_{23}|)^2}}{2}$, $H(x) = -xLog_2(x) - (1-x)Log_2(1-x)$ is the binary Shannon entropy and $\lambda_k$ are the eigenvalues of the matrix $\rho_{AB}$.

Quantum discord, like entanglement measures, possesses several properties:

1. The value of quantum discord $\mathcal{D}(\rho_{AB}) \geq 0$ for any quantum state $\rho_{AB}$. This property ensures that quantum discord is a valid measure of quantum correlations. The equality holds for classical systems where a local measurement on subsystem B does not disturb the system.

2. Quantum discord is asymmetric in nature. This means that $\mathcal{D}(\rho_{AB})$ is not necessarily equal to $\mathcal{D}(\rho_{BA})$, indicating that the measurement or observation made on one subsystem $(B)$ can have a different impact on the other subsystem $(A)$ compared to the reverse scenario.

3. Quantum discord remains invariant when local unitary transformations are applied to the quantum state.

4. For pure bipartite states, quantum discord is closely related to the concept of entanglement. Specifically, when the quantum state is pure, the quantum discord reduces to the entanglement measured by the Von Neumann entropy.

### 2.3.3 Global Quantum discord

It is clear that the quantum discord is an asymmetric quantity as it depends on the subsystem upon which the measurements are performed. In this regard, Rulli *et al* [118] proposed a symmetrized version called global quantum discord:

$$D_{Global}(\rho_{XY}) = Min_{\{\Pi_X^j \otimes \Pi_Y^k\}} \{S(\rho_{XY}||\Phi_{XY}(\rho_{XY})) - S(\rho_X||\Phi_X(\rho_X)) - S(\rho_Y||\Phi_Y(\rho_Y))\}, \tag{2.77}$$

with

$$\Phi_{XY}(\rho_{XY}) = \sum_{j,k}(\Pi_X^j \otimes \Pi_Y^k)\rho_{XY}(\Pi_X^j \otimes \Pi_Y^k),$$

$$\Phi_\alpha(\rho_\alpha) = \sum_j(\Pi_\alpha^j \rho_\alpha \Pi_\alpha^j),$$

and $S(\rho||\sigma)$ is the relative entropy defined as $S(\rho||\sigma) = Tr(\rho \text{Log}_2(\rho) - \rho \text{Log}_2(\sigma))$.

## 2.4 Contribution 1: Global quantum discord and entanglement in two coupled double quantum dots AlGaAs/GaAs

### 2.4.1 Introduction

In this section, we present a theoretical study on the behavior of global quantum discord and entanglement in two coupled double quantum dots made of AlGaAs/GaAs as a function of temperature. We use each double quantum dot as a qubit, where the electron can occupy either the right or left dot. Our investigation aims to understand the impact of the energy offset of each qubit and the tunneling coupling energy on quantum correlations. Our findings show that the energy offset and tunneling coupling energy significantly affect the variations of entanglement of formation, standard discord, and global quantum discord. Our results provide insights into the interplay between quantum correlations and environmental parameters and have important implications for developing quantum technologies.

Quantum correlations provide precious resources for quantum information tasks. The most interesting measurement of quantum correlations (QC) is entanglement [119] which has been synonymous with quantum correlations for a long time. Albeit, it plays an important role in the quantification and classification of QC that are present in a given quantum system[120, 121], various studies [26, 122, 123] have proved that QC exists even in separable states [124]. Several alternative measurements have been proposed to quantify QC. For example, Zurek *et al* introduced quantum discord for this purpose [26, 122, 123]. This measure presents the interesting property of being more robust than entanglement. As such, when entanglement vanishes in some bipartite systems, discord can survive against the temperature and other decoherence effects. It is therefore interesting to consider quantum discord as a fundamental resource for quantum computing tasks [125, 126, 127, 128, 29]. Recently, the generalization of quantum discord for a multipartite system has been proposed in different ways. The first approach is based on the generalization of mutual information to multipartite systems [129, 130]. The other one is to initially define a measure based on the relative entropy [131, 132]. One of the difficulties in QD as a measure of quantum correlations is that it is not symmetric and it depends on which subsystem is actually being measured. Global quantum discord (GCD) [133] was then proposed as an alternative definition that is always non-negative and symmetric under permuting the roles of the subsystems.

On the other hand, recent years have seen tremendous technical progress allowing the development of semiconductor quantum dots and the uses of these artificial and tunable atoms in

various topics including quantum computation [134, 135, 31, 30]. Many authors have thus focused on the study of QC in quantum dots recently. Indeed, Fanchini *et al.*[136] studied the QC dynamics of two coupled double quantum dots in an open quantum system. In this section, we study the behavior of GQD and entanglement between two double quantum dots (DQD) whereby each DQD forms a qubit in which the electron can occupy the right or the left dot [118], and are free to move between the two dots forming the DQD. In this model, we consider the interaction between two double quantum dots, each DQD consisting of right and left dots connecting through a tunneling barrier. The conductance is influenced by one dot and interdot Coulomb interaction through the tunneling barrier. In the case of weak coupling (small voltage between the source and drain) a finite current is observed at the triple points, where tunneling processes through the three tunneling barriers are allowed, under an appropriate condition where only the interdot tunneling is allowed and the Coulomb interaction effectively isolates the DQD from the source and drain electrodes. In this case, we can consider two charge states, in which an excess electron occupies the left dot ($|L\rangle$) or the right dot ($|R\rangle$) with electrochemical potentials $E_L$ and $E_R$, respectively. When the two specific states are energetically close to each other and the excitation to other states can be neglected, the system can be approximated as a two-level system (qubit). It is characterized by the energy offset, $\epsilon = E_R - E_L$.
This model can be experimentally implemented using AlGaAs/GaAs heterostructure containing two-dimensional electron gas [118]. In this model, we consider a series of Schottky gates and we control the electron configuration in each DQDs by adjusting the voltages applied to the gates. Furthermore, the two DQDs are coupled using the capacitance model describing the Coulomb interaction. The manipulation of the electronic system in quantum dots and a clear understanding of decoherence in practical structures are crucial for future applications of quantum nanostructure to quantum information technology and for a variety of thermodynamic-oriented applications. This model is considered as a working substance for heat machines, and the appearance of different regions of operation for the heat machines (the heat and refrigerator) by adjusting the value of interaction coupling. This nanotechnology is crucial also for a variety of biological applications, including fluorescent assays for drug discovery [137], disease detection[138], single protein tracking and intracellular reporting[139]. The choice of this model is based on several factors, among them, AlGaAs/GaAs allow for precise control and manipulation of the quantum states, it has a well-defined energy spectrum, and has the ability to control the electron-electron interactions and tunneling coupling between the double quantum dots, leading to the observation of various quantum correlation effects. This system has an advantage of being a solid-state device with a high degree of scalability, making it well suited for integration with existing semiconductor technology. Additionally, this system can be operated at low temperatures, allowing for more precise control and manipulation of the quantum states. In effect, we study the QC against temperature, tunneling coupling, and energy offset parameters. We also investigate the role played by the coupling parameter $J$ in the QC. We stress the difference in behavior between the symmetric global discord and the standard discord against the tunneling parameters in each DQD.

### 2.4.2 The model of AlGaAs/GaAs quantum dots

We consider a system of two double quantum dots (DQDs) separated by a potential barrier. Each double quantum dot can be theoretically considered as a two-level system, where the electron can occupy the right or the left dot ($|L\rangle$ or $|R\rangle$) (see figure 2.6). As such, one can use this system for the implementation of a qubit in each double quantum dot. In this case, we consider an Ising-type coupling $\frac{J}{4}(\sigma_z^{(1)} \otimes \sigma_z^{(2)})$ between artificial and tunable charge qubits fabricated in a semiconductor nanostructure.

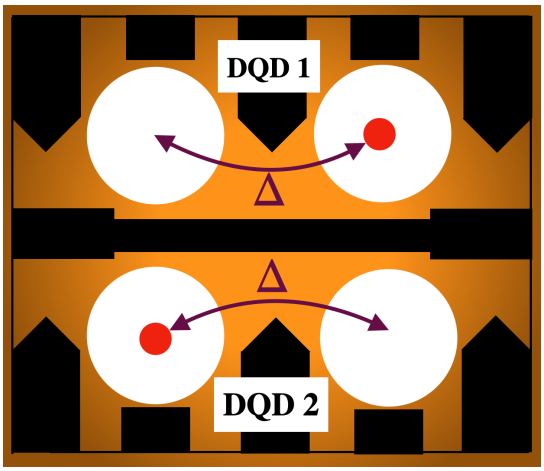


FIGURE 2.6: Schematic representation of two DQDs with one electron localized at the left (right) side of the top (bottom) DQD.

The Hamiltonian of the two-qubit system then reads [118]:

$$H = \frac{1}{2}\sum_{i}^{2}(\epsilon_i \sigma_z^{(i)} + \Delta_i \sigma_x^{(i)}) + \frac{J}{4}(\sigma_z^{(1)} \otimes \sigma_z^{(2)}), \tag{2.78}$$

where $\sigma^i_{x,y,z}$ are the Pauli matrices of the $i^{th}$ qubit, $\epsilon_i$ describes the energy offset of each qubit state, $\Delta_i$ represents the tunneling coupling inside each double quantum dot and $J(>0)$ is the strength of the coupling (Coulomb interaction between electrons). It is worth noting that this Hamiltonian can also be used in describing other physical systems ranging from superconducting qubits to ultracold atoms in optical lattices [140, 141, 142].
The temperature-dependent density matrix describing the state of the system in equilibrium at a temperature $T$ reads

$$\rho(T) = \frac{1}{Z}.exp[-\beta H], \tag{2.79}$$

with $\beta = (K_B T)^{-1}$, $K_B$ being the Boltzmann constant and $Z$ is the partition function given by,

$$Z(T) = Tr(exp[-\beta H]). \tag{2.80}$$

Before presenting the results of our study, we aim to shed light on the relationship between quantum correlations and the parameters in our system. Specifically, we plot figures of entanglement and both standard and global discord to visualize their behavior. We examine the impact of the energy offset of each qubit and the tunneling coupling energy on these quantum correlations. Additionally, we make a comparison of the changes in the entanglement of formation, standard discord, and global quantum discord. The results of this analysis will contribute to our understanding of how these parameters influence the presence and strength of quantum correlations in such systems.

### 2.4.3 Results and discussions

In this section, we comparatively investigate the behavior of quantum correlations of the system against the different parameters of the system. In Figure 2.7, we plot the variation of both the $EOF$ and $QD$, for different values of the strength coupling $J$, against the temperature $T$.

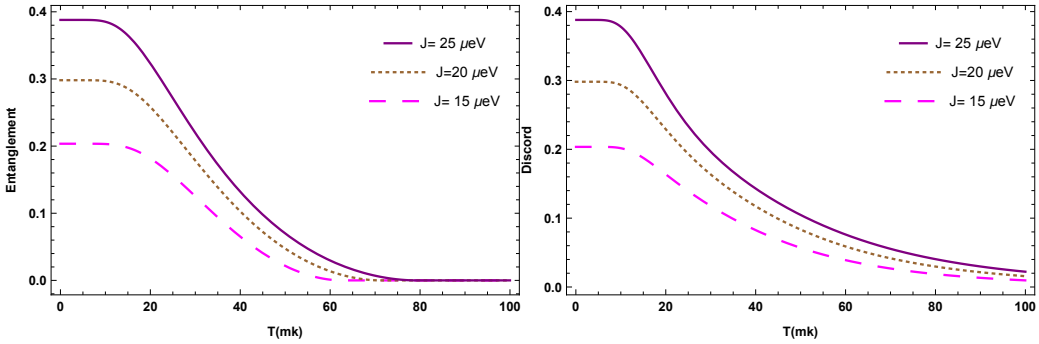


(A) ENTANGLEMENT (B) DISCORD

FIGURE 2.7: Entanglement of formation and quantum discord as a function of temperature $T$ for different values of $J$, with the other parameters fixed at $\epsilon_1 = \epsilon_2 = 0\mu eV$ and $\Delta_1 = \Delta_2 = 10\mu eV$.

Figures 2.7a and 2.7b show that the entanglement and discord decay continuously when the temperature is increased. This decay is mainly due to the thermal relaxation effects. We also observe that the quantum correlations reach their maximum values for smaller temperatures. As the temperature reaches relatively higher values, both entanglement and quantum discord vanish, though the latter is more resistant than the former as it relatively survives more. In addition, one can confirm that the effect of the strength of the coupling parameter $J$ on QC is to favor these quantum correlations for large values.

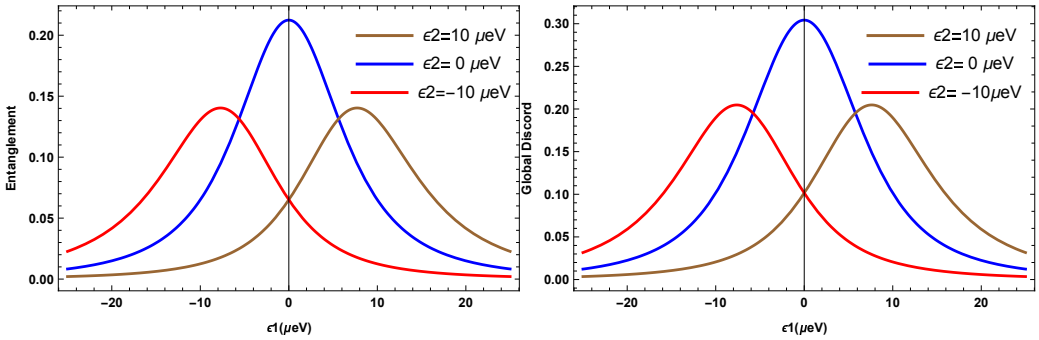


(A) ENTANGLEMENT (B) GLOBAL DISCORD

FIGURE 2.8: Entanglement and Discord as a function of $\epsilon_1$ for different values of $\epsilon_2$, the other parameters being fixed at $\Delta_1 = \Delta_2 = \frac{25}{3}\mu eV$, $J = 20\mu eV$ and $T = 25mK$.

Figure 2.8 displays the behavior of entanglement 2.8a and global discord 2.8b for different values of energy offset of the second qubit $\epsilon_2$, against the same parameter for the first qubit state $\epsilon_1$. It is clear from the figures that both quantum correlations take their maximum when $\epsilon_1 = \epsilon_2$. We can thus say that the quantum correlations take their maximum at resonance condition when $\epsilon_2 = \epsilon_1$. Furthermore, the amount of correlations at resonance when $\epsilon_2 = \epsilon_1 = 0\mu eV$ is higher than the other cases. In this respect, we find that the energy offset is detrimental to the amount of quantum correlations.

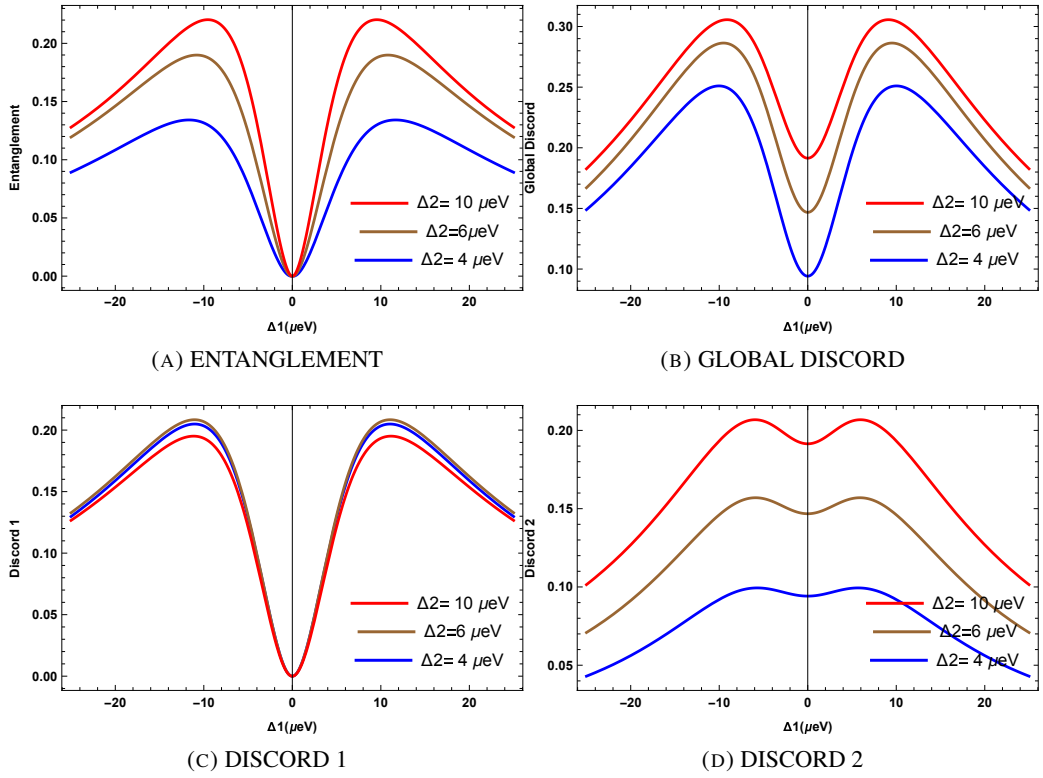


(A) ENTANGLEMENT (B) GLOBAL DISCORD

(C) DISCORD 1 (D) DISCORD 2

FIGURE 2.9: Entanglement, Global Discord, and Standard Discord as a function of $\Delta_1$ for different values of $\Delta_2$, with the other parameters fixed at $\epsilon_1 = \epsilon_2 = 0\mu eV$, $J = 20\mu eV$ and $T = 25mK$.

In order to study the effects of the tunneling coupling energy $\Delta_{i=1,2}$ on the quantum correlations, we plot the behavior of entanglement, quantum discord, and global quantum discord as a function of $\Delta_1$ for different values of $\Delta_2$. As a matter of simplicity, we will note by "Discord 1" the quantum discord obtained when the local measurement, is performed over the first subsystem, and "Discord 2" when it is the second subsystem that is measured. We can observe that the entanglement vanishes when $\Delta_1 = 0$ regardless of the values of $\Delta_2$. In this case, the two double quantum dots are not entangled, because the electron can no longer move within the double quantum dots. On the other hand, global quantum discord is still present although the value of $\Delta_1 = 0$ shows again that despite the state being separable, the system still possesses quantum correlation. However, for the quantum correlations as captured by discord 1 (Figure 2.9a), they too vanish when $\Delta_1 = 0$ just like entanglement. This means that performing a measurement on the first subsystem has a disturbing effect on discord 1 which explains the loss of the quantum correlations. This is in contrast with discord 2, which is present and non-negligible even for $\Delta_1 = 0$. This fully displays the asymmetric nature of the original quantum discord versus the symmetric nature of the global quantum discord. It is worth noting, here that discord 2 vanishes when it is the tunneling coupling in the second double quantum dot that vanishes: $\Delta_2 = 0$. On a final note, the amount of quantum correlations increases with the increase of $\Delta_2$.

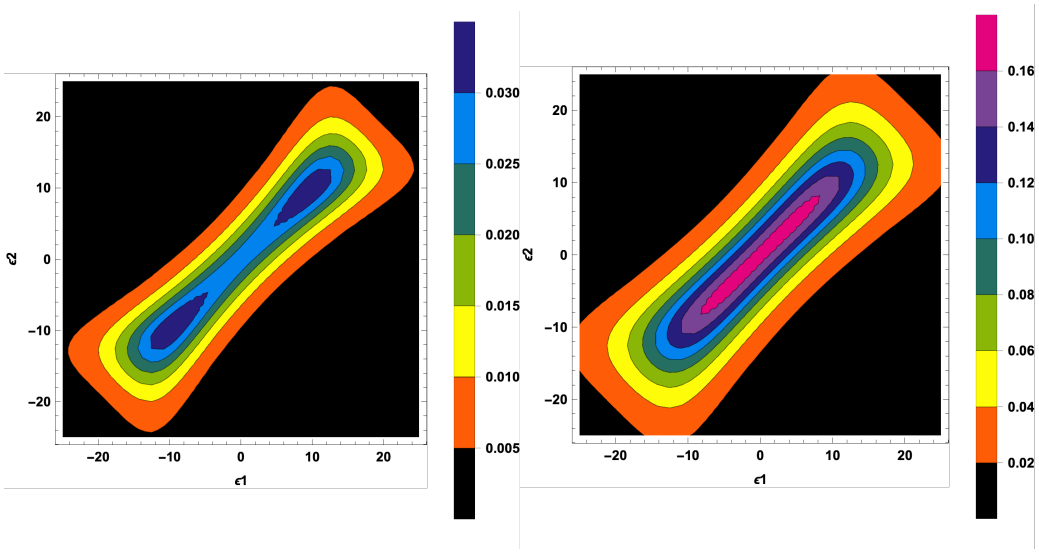


(A) Entanglement: $\Delta_1 = \Delta_2 = \frac{25}{8}\mu eV$

(B) Entanglement: $\Delta_1 = \Delta_2 = \frac{25}{4}\mu eV$

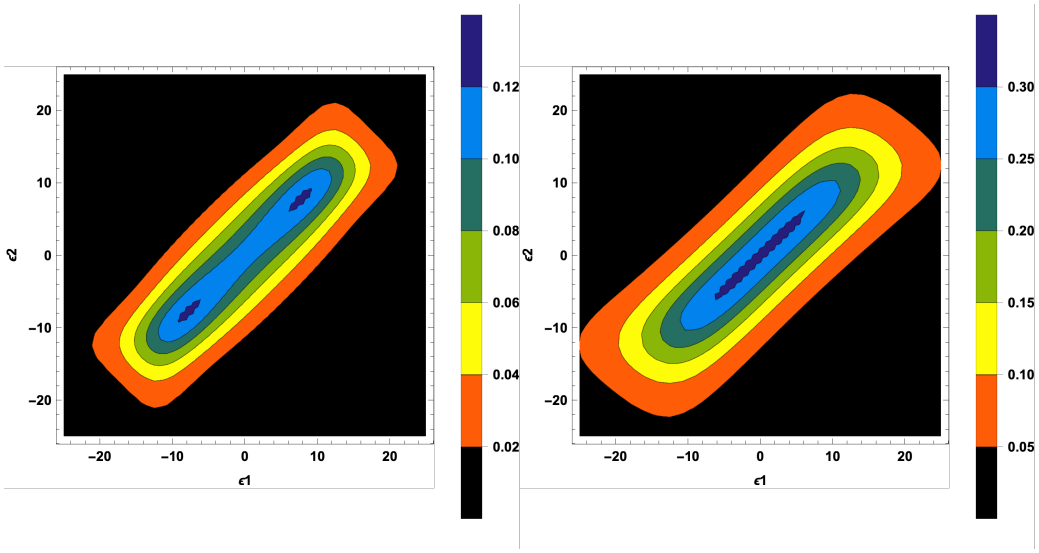


(C) Global Discord: $\Delta_1 = \Delta_2 = \frac{25}{8}\mu eV$

(D) Global Discord: $\Delta_1 = \Delta_2 = \frac{25}{4}\mu eV$

FIGURE 2.10: Entanglement and Discord as a function of $\epsilon_1$ and $\epsilon_2$, with $J = 25\mu eV, T = 25mK$.

To have a global overview of the different behaviors we cast these in the form of density plots. Figure 2.10 shows the behavior of entanglement of formation and global quantum discord as a function of $\epsilon_1$ and $\epsilon_2$ for different values of $\Delta_{1,2}$. This figure confirms our previous results that the energy offset is detrimental to quantum correlations and more so when the value of this parameter is different in both double quantum dots. This harmful effect can be relatively contained by equating the two parameters $\epsilon_1$ and $\epsilon_2$. So, one can control the amount of correlations by adjusting the values of the energy offset in the first and the second qubits. Another remark is that the quantum correlations vanish when $|\epsilon_1| > 20\mu eV$ and/or $|\epsilon_2| > 20\mu eV$, and the amount of these correlations depends on the tunneling coupling parameters. when we increase these parameters the amount of correlations increases too.
Now we plot in figure 2.11 the behavior of quantum correlations against both parameters

$\Delta_1$ and $\Delta_2$, We notice that the entanglement doesn't exist when the values of $\Delta_1$ or $\Delta_2$

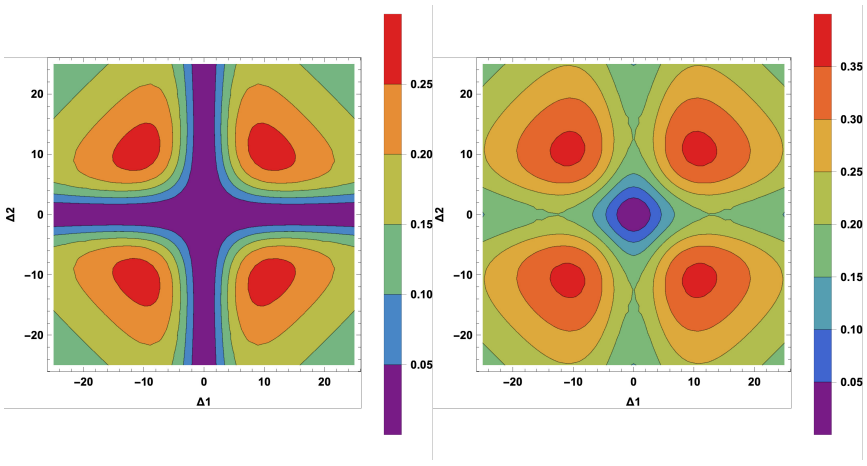


(A) Entanglement: $\epsilon_1 = \epsilon_2 = 0\mu eV$

(B) Global Discord: $\epsilon_1 = \epsilon_2 = 0\mu eV$

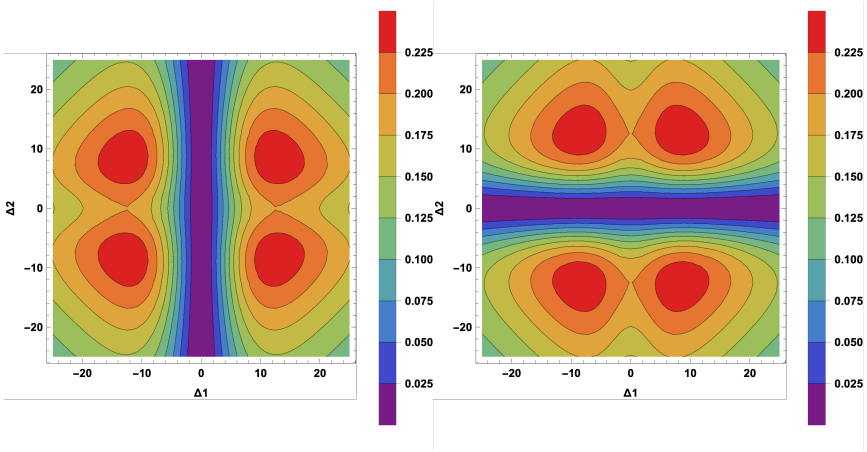


(C) Discord 1: $\epsilon_1 = \epsilon_2 = 0\mu eV$

(D) Discord 2: $\epsilon_1 = \epsilon_2 = 0\mu eV$

FIGURE 2.11: Entanglement and Discord as a function of $\Delta_1$ and $\Delta_2$, with $J = 20\mu eV, T = 25mK$.

approach zero, regardless of the values of the other parameters. When we increase $\Delta_1$ or $\Delta_2$, the amount of entanglement is increased and reaches its maximum when $\Delta_1 = \Delta_2 = \frac{J}{2} = 10\mu eV$ before decreasing again upon further increase of the coupling. On the other hand, global quantum discord doesn't exist in the only case where $\Delta_1$ and $\Delta_2$ are zero. This, on one hand, confirms the robustness of the global discord compared to entanglement against the tunneling coupling inside each double quantum dot, on the other hand, it confirms its symmetric nature unlike discord 1 and 2 discussed next. For the quantum correlations as captured by the original quantum discord, it is confirmed that the results depend on which subsystem is being measured. For instance discord 1 is absent when $\Delta_1$ tends to zero, while discord 2 vanishes when $\Delta_2$ tends to zero. This is due to the fact that the measurements performed on subsystem 1 or 2 respectively perturb this latter and subsequently lead to the losses of quantum correlation captured by these quantities.

### 2.4.4 Conclusion

In summary, we have provided a theoretical study of quantum correlations behaviors against the temperature between electrons in two sets of coupled double quantum dots. We studied the effect of the energy offset of each qubit and the tunneling coupling energy inside each double quantum dot on quantum correlations. Additionally, we have compared the variations of entanglement of formation, standard discord, and global quantum discord.
We have shown that the quantum correlations decay is continuous when we increase the temperature due to the thermal relaxation effects. In addition, we have noted that the amount of quantum correlations increases when the strength of the coupling parameter increases and observed that the quantum correlations reach their maximum at resonance conditions. As expected, the behavior of global discord is similar to that of entanglement. This is due to the fact that measurements performed on either subsystem perturb this latter and subsequently lead to a loss of QC. The model provided also a stage for the understanding of the differences in the behaviors of standard quantum discord and global quantum discord.
We deem that the results pave the way to a proper understanding of the behavior of these types of quantum dots and their correlations in general. Since quantum dots, in general, are promising hosts for the manipulation of qubits and building quantum processors, it is of paramount importance to understand the effect of different types of interactions in the system and the dynamics of quantum correlations in an open quantum system. In this regard, the study can be generalized, to address the question of the dynamics of quantum correlations in an open quantum system and to study multipartite correlations. This is discussed in the next chapter.

# Chapter 3

# Quantum correlations in two coupled semiconductor InAs quantum dots in an open quantum system

## 3.1 Quantum theory of open systems

### 3.1.1 From closed systems to open systems

After discussing the evolution of closed quantum systems described by a state vector $|\psi\rangle$ (see the section 2.1.1), we now turn our attention to systems that can only be described by the density matrix $\rho$. These systems are represented by a quantum statistical ensemble.
Let $\rho(t_0)$ be the initial state at time $t_0$, defined as follows,

$$\rho(t_0) = \sum_{\alpha} \omega_\alpha |\psi_\alpha(t_0)\rangle\langle\psi_\alpha(t_0)|. \tag{3.1}$$

Since the vectors $|\psi_\alpha(t_0)\rangle$ depend on time according to the given evolution, the density matrix of the system at time $t$ is given by,

$$\rho(t) = \sum_{\alpha} W_\alpha U(t,t_0)|\psi_\alpha(t_0)\rangle\langle\psi_\alpha(t_0)|U^\dagger(t,t_0) = U(t,t_0)\rho(t_0)U^\dagger(t,t_0). \tag{3.2}$$

By taking the derivative of $\rho(t)$ with respect to time, we obtain the Liouville-von Neumann equation,

$$\frac{d\rho(t)}{dt} = -i[H(t),\rho(t)]. \tag{3.3}$$

After describing the most important equations describing the dynamics of closed quantum systems, we will now focus on open systems. The following figure 3.1 illustrates an open quantum system. The system S is coupled to another quantum system called the environment. The interaction between system S and the environment generates a certain correlation between them, which is responsible for the non-unitary nature of the open system. Consequently, the reduced system must be described by a quantum master equation. The Hilbert space of the total system $S+E$ is given by the tensor product $\mathcal{H} = \mathcal{H}_\mathcal{S} \otimes \mathcal{H}_\mathcal{E}$, where $\mathcal{H}_\mathcal{S}$ and $\mathcal{H}_\mathcal{E}$ are the Hilbert spaces of the system and the environment, respectively. Then, the total Hamiltonian $H$ takes the following form:

$$H(t) = H_S \otimes I + I \otimes H_E + H_{int}(t). \tag{3.4}$$

Where $H_S$ and $H_E$ are time-independent free Hamiltonians, the interaction is described by the time-dependent interaction Hamiltonian $H_{\text{int}}(t)$.

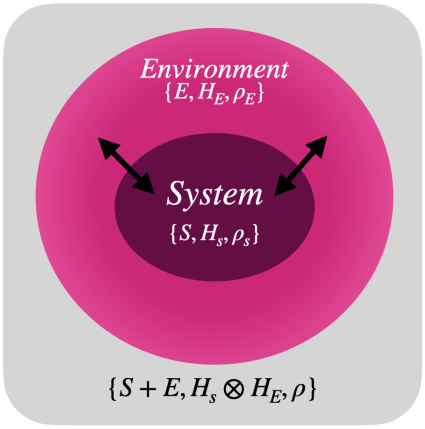


FIGURE 3.1: System with the environment

In most mathematical models describing the dynamics of open systems, the environment is represented by a reservoir consisting of an infinite number of degrees of freedom. This typically leads to irreversible behavior of the open system and the need to solve a coupled set of infinitely many equations of motion. To solve this problem, efforts are made to work within the reduced space of the system, described by a set of physical parameters.
We are only interested in observables that are related to the open systems S. Starting from $A \otimes I_E$, where $A$ acts on $H_s$ and $I_E$ represents the identity on $H_E$, we will define density matrices that represent the state of the system. The density matrix $\rho$ without any indices should be the state of the global system, while the indices $E$ and $S$ represent the specific subsystems. $\rho_s$ can be obtained by taking the partial trace over the degrees of freedom of the environment.

$$\rho_S = Tr_E(\rho). \tag{3.5}$$

Since the global density matrix evolves unitarily in time, by substituting $\rho_s$ into eq. 3.2, we obtain,

$$\rho_s(t) = \mathrm{Tr}_E\{U(t,t_0)\rho(t_0)U^\dagger(t,t_0)\}. \tag{3.6}$$

Where $U(t,t_0)$ is the time evolution operator of the global system. To obtain an equation of motion for the reduced system, we can take the partial trace over the environment on both sides of the Liouville-Von Neumann equation 3.3 for the global system.

$$\frac{d}{dt}\mathrm{Tr}_E(\rho(t)) = \frac{d}{dt}\rho_s(t) = -i\mathrm{Tr}_E[H(t),\rho(t)]. \tag{3.7}$$

All of these equations are correct, but in practice, they are not very applicable because the state of the global system $\rho$ is always involved. Due to the limited understanding of the environmental modes, the state of the global system is typically unknown. In the following sections, we will introduce certain approximations that allow us to derive equations of motion solely based on the state of the reduced density matrix $\rho_S$.

### 3.1.2 Standard theory of Markovian open quantum systems

Markovian systems are the most well-characterized open quantum systems from both mathematical and physical perspectives. Furthermore, the simplest example of the dynamics of an open quantum system is provided by a Markovian quantum process, in which all memory effects are eliminated (the environment forgets the past interaction with the system due to the dispersion of correlations in the degrees of freedom of the environment) and the dynamics are time-stationary.

**Markovian master equation.**

For a dynamic quantum semigroup [143], there exists a generator of the Markovian master equation $\mathcal{L}$ that determines the equation of motion for the state of the reduced system $\rho_s$. This equation is known as the Markovian master equation and is defined by [143],

$$\dot{\rho} = \frac{d\rho(t)}{dt} = \mathcal{L}\rho_s(t), \tag{3.8}$$

In this case, $\mathcal{L}$ is the operator that acts on the system $S$. According to the Gorini-Kossakowski-Sudarshan-Lindblad theorem, the generator $\mathcal{L}$ is the generator of a completely positive quantum dynamical semigroup if and only if it can be written as follows,

$$\mathcal{L}\rho_s = -i[H_s, \rho_s] + \sum_i \gamma_i (A_i \rho_s A_i^\dagger - \frac{1}{2}\{A_i^\dagger A_i, \rho_s\}). \tag{3.9}$$

Where $H_s$ is the system's Hamiltonian, $A_i$ are operators of the system known as the Lindblad operators, and $\gamma_i \geq 0$ are the corresponding decay rates.

The standard theory of Markovian dynamics has been widely applied and provides a qualitatively accurate description of many systems. However, for systems with strong coupling to the environment, finite reservoirs, and low temperatures, the Markov approximation becomes less effective, and alternative techniques are needed to study the dynamics of open systems.

**Microscopic derivation of the Markovian master equation**

we consider a system $S$ interacting with an environment $E$ through the Hamiltonian $H_{\text{int}}$. The total Hamiltonian is given by $H = H_s + H_E + H_{\text{int}}$, where $H_{\text{int}}$ acts on $H_s \otimes H_E$. The dynamics of the total system can be described by the following expression:

$$\frac{d\rho(t)}{dt} = -i[H_{\text{int}}, \rho(t)], \tag{3.10}$$

where $H_{\text{int}}(t) = e^{iH_0 t}$, $\rho(t) = e^{iH_0 t}\rho(t)e^{-iH_0 t}$, and $H_0 = H_s + H_E$. The formal solution of the integral is given as follows:

$$\rho(t) = \rho(0) - i\int_{t_0}^{t} [H_{\text{int}}(s), \rho(s)]ds. \tag{3.11}$$

By inserting the expression from Eq. 3.11 into Eq. 3.10 and subsequently taking the partial trace over the environment, we obtain:

$$\frac{d\rho_s(t)}{dt} = -\int_0^t ds\, \text{Tr}_E[H_{\text{int}}(s), [\rho(s), H_{\text{int}}(t)]]. \tag{3.12}$$

Here, we assume that $\text{Tr}_E[H_{\text{int}}(t), \rho(0)] = 0$. Equation 3.12 describes the general dynamics of an open system.

In this section, we will not provide the details of the derivation, but our objective is to summarize the key approximations that determine a dynamic quantum semigroup. The first crucial assumption we introduce is the Born approximation, which assumes that the coupling between the system and the environment is weak, meaning that the environment is not significantly influenced by the system during its evolution. Thus, the total state can be approximated and written as $\rho(t) \simeq \rho_S \otimes \rho_E(0)$. This assumption allows us to obtain the following form of the equation:

$$\frac{d\rho_s(t)}{dt} = -\int_0^t ds\, \mathrm{Tr}_E[H_{\text{int}}(t), [H_{\text{int}}(s), \rho_s(s) \otimes \rho_E(0)]]. \tag{3.13}$$

The expression of this equation (3.13) can be simplified by the Markov approximation, which substitutes the given state at the delayed time $\rho_S(s)$ with $\rho_S(t)$ at the current time. The equation of motion can then be given in the form of local time:

$$\frac{d\rho_s(t)}{dt} = -\int_0^t ds\, \mathrm{Tr}_E[H_{\text{int}}(t), [H_{\text{int}}(s), \rho_s(s) \otimes \rho_E(0)]]. \tag{3.14}$$

This equation (3.14) is called the Redfield equation. It is not always Markovian as it depends on the choice of the initial preparation at $t = 0$. In order to obtain a Markovian master equation, we need to consider the timescales of the system under study. Let $\tau_E$ be the timescale on which the environmental correlation functions decay and $\tau_R$ be the timescale on which the system relaxes to a stable state. If $\tau_R \geq \tau_E$, the integrand in equation (3.14) quickly vanishes for $s \geq \tau_E$. To satisfy the semigroup property, we replace the time variable $(s)$ with $(t - s)$ and extend the integration to infinity. We then obtain:

$$\frac{d\rho_s(t)}{dt} = -\int_0^\infty ds\, \mathrm{Tr}_E[H_{\text{int}}(t), [H_{\text{int}}(t-s), \rho_s(t) \otimes \rho_E(0)]]. \tag{3.15}$$

The equation defined above (3.15) characterizes the dynamics on a coarse-grained timescale, where we eliminate $\tau_E$ and focus solely on the dynamics of the relaxation timescale $\tau_R$. However, it does not take the form of a Markovian equation, which is why another approximation must be implemented. This is known as the "secular" approximation. This approximation is valid when the timescale of the system's free evolution $\tau_s$ is much smaller than $\tau_R$. As a result, we obtain an equation that takes the form of a Markovian equation, and in this case, the evolution is given by a dynamical semigroup.

### 3.1.3 Non-Markovian master equations

The semi-group property is a very restrictive assumption in the quantum process. In fact, the approximations made when we microscopically derive the master Markovian equation are often not valid. Furthermore, the dynamics of the open system can often be non-stationary and non-Markovian at the same time. Moreover, for a general quantum process, a reasonable description of the generators does not exist. In this regard, considerable effort has been made to obtain a generalized master equation for the non-Markovian regime.

#### Master equation of the memory kernel

The master equation of the memory kernel aims to generalize the Markovian master equation by introducing a temporal integration of the system state starting from $t = 0$. This has been phenomenologically considered as a cause of non-Markovian effects (memory effects). The dynamic is expressed by the following formula:

$$\dot{\rho} = \frac{d\rho_s(t)}{dt} = -\int_0^t K(t-s)\rho_s(s)ds, \tag{3.16}$$

where the Markovian master equation is obtained for the memory kernel $k(t - s) = \delta(t - s)L$. The general form of the memory kernel $k(t, s)$ can yield results that have no physical significance [144]. Moreover, even for physically relevant equations, researchers have shown that sometimes these equations can fail to describe non-Markovian effects [145].

However, certain forms ensuring the physical significance of certain memory kernel equations have been derived. In this regard, Lidar and his colleagues [146] derived the so-called post-Markovian master equation, which interpolates between the interpretation of continuous measurement of Markovian dynamics and the generalized interpretation of the exact sum measurement of the Kraus operator. The resulting master equation is analytically solvable, and the region of physically relevant parameters can be identified. Furthermore, Daffer and his colleagues have shown that the kernel function $k(t,s)$, which is extracted from a reservoir model based on a random telegraph process, is assumed to be the product of a scalar function with a semi-group generator $\Phi$. This model will be examined and discussed later in the third chapter.

**Temporal-local master equations**

Non-Markovian temporal-local master equations have been widely used to study non-Markovian dynamics. On the one hand, these equations are characterized by providing a relatively simple method to describe memory effects. On the other hand, they generalize the Markovian equation. Due to the necessity of preserving Hermiticity ($L(t)A^\dagger = L(t)A^\dagger$) and trace ($\mathrm{Tr}(L(t)A) = 0$), the generator of this type of equation must always be expressed as follows:

$$L(t)\rho_s = -i[H,\rho_s] + \sum_i \gamma_i(t)(A_i(t)\rho_s A_i^\dagger(t) - \frac{1}{2}A_i(t)A_i^\dagger,\rho_s). \tag{3.17}$$

The time-dependent coefficients $\gamma_i(t)$ in the memory kernel master equation can temporarily take negative values. When the correlation time of the environment becomes comparable to the relaxation time scale of the system, negative decay rates can arise from the microscopic derivation. It is important to note that the negativity of $\gamma_i(t)$ does not imply a straightforward reversal of the process direction, but rather encodes the history of the evolution, allowing for memory effects [147].
The memory kernel master equation in the form (3.16) can be transformed, under general assumptions, into the time-convolutionless form of Eq. (3.17). Despite the fact that the time-local description has been established for over 40 years and has been successfully applied to numerous non-Markovian problems, there have been misconceptions regarding the applicability of these equations [147]. Similar to the memory kernel equations, there is no theorem specifying the form of the generator in Eq. (3.17) to ensure complete positivity of the quantum dynamical map. However, if the rates $\gamma_i(t)$ are non-negative for all times, $\gamma_i(t) \geq 0$, the resulting dynamics is indeed completely positive, as the generator is then in Lindblad form for each fixed $t \geq 0$.

Now, let us briefly demonstrate the expression of Eq. (3.17) for a finite-dimensional open system Hilbert space with dimension $\dim(\mathcal{H}_S) = N$. Consider a fixed time $t$ and a fixed complete set of operators $\{F_i\}$ on $\mathcal{H}_S$, where $i = 1, 2, ..., N^2$, and these operators are orthonormal with respect to the Hilbert-Schmidt scalar product. Specifically, we have,

$$(F_i, F_j) = Tr_S(F_i^\dagger F_j) = \delta_{ij}. \tag{3.18}$$

For convenience, we choose one of the basis operators to be proportional to the identity, i.e., $F_N^2 = \frac{1}{\sqrt{N}} I_S$, while the other basis operators are traceless, i.e., $Tr_S(F_i) = 0$.
Equation (3.17) can be expressed in the following form, [148],

$$L(t)\rho_S = -i[H_S,\rho_S] + \frac{1}{2}\sum_{ij}^{N^2-1} c_{ij}(t)([F_i(t),\rho_S F_j^\dagger(t)] + [F_i(t)\rho_S, F_j^\dagger(t)]), \tag{3.19}$$

where $H_S(t) = H_S^\dagger(t)$, and $c_{ij}$ is a complex positive semidefinite matrix that can be diagonalized using a unitary matrix $u(t) = u_{ij}(t)$, such that,

$$u(t)c_{ij}(t)u^\dagger(t) = \text{diag}(\gamma_1(t), \gamma_2(t), ..., \gamma_{N^2-1}(t)).$$

Where the eigenvalues $\gamma_i$ are non-negative. Introducing the new operators,

$$A_i(t) = \sum_{j=1}^{N^2-1} u_{ij}^*(t)F_j, \tag{3.20}$$

we obtain then the equation (3.17) form of the generator.

### 3.1.4 Non-Markovian quantum dynamics and information flow

In recent years, there has been a lack of consensus in defining and quantifying quantum non-Markovianity due to the challenges in formulating a clear condition for Markovian dynamics. The understanding of memory effects in open quantum systems has often relied on inaccurate arguments about the features of the master equation describing the process. The presence of a memory kernel or the occurrence of negative decay rates and revivals in the dynamics has been associated with non-Markovianity. The crucial question is how to rigorously define and quantify quantum non-Markovianity in a manner independent of the specific formalism used to derive the master equation.

One approach to quantifying quantum non-Markovianity is based on the observation that memory effects in the dynamics of open systems are connected to the exchange of information between the system and its environment [149]. In a Markovian regime (without memory), the system continuously loses information to the environment. However, in a non-Markovian regime (with memory), information flows back into the system from the environment. Quantum non-Markovianity can be understood in terms of quantum memory, where information that has been transmitted to the environment is subsequently recovered by the system. The exchange of information is quantified by employing the trace distance as a measure of the difference between quantum states.

#### Trace distance and distinguishability:

The non-Markovianity measure is based on evaluating the distance between a pair of states represented by density operators $\rho_1$ and $\rho_2$. This distance is determined using the trace distance, which is defined as:

$$D(\rho 1, \rho 2) = \frac{1}{2}\|\rho_1 - \rho_2\| = \frac{1}{2}\text{Tr}|\rho_1 - \rho_2|, \tag{3.21}$$

where $||X|| = Tr\sqrt{|X|} = Tr\sqrt{XX^\dagger}$ denotes the trace norm.

Consider a scenario where a quantum system can exist in two states, $\rho_1$ and $\rho_2$, each with a probability of $P1 = P2 = \frac{1}{2}$. If the goal is to determine which state the system is in, the quantity $P = \frac{1}{2}(1 + D(\rho 1, \rho 2))$ provides the optimal probability for successfully identifying the system's state. For instance, if the states $\rho_1$ and $\rho_2$ are orthogonal, they can be distinguished with certainty, i.e., $D(\rho 1, \rho 2) = 1$. Conversely, if $\rho_1 = \rho_2$, no information about the state can be obtained through measurements, yielding $D(\rho 1, \rho 2) = 0$. Hence, the trace distance between any pair of states satisfies the condition $0 \leq D(\rho 1, \rho 2) \leq 1$.

An important property of the trace distance is that completely positive and trace-preserving maps, denoted as $\Phi$, contract the trace distance. In other words, for any such map, the inequality $D(\Phi(\rho 1), \Phi(\rho 2)) \leq D(\rho 1, \rho 2)$ holds. This implies that a trace-preserving quantum operation cannot increase the distinguishability between two quantum states. Additionally, the trace distance remains invariant under unitary transformations U, meaning that $D(U\rho 1U^{\dagger}, U\rho 2U^{\dagger}) = D(\rho 1, \rho 2)$. It is worth noting that the distinguishability between states for closed systems remains constant over time.

## 3.2 Contribution 2:Quantum correlations dynamics in two coupled semiconductor InAs quantum dots

### 3.2.1 Introduction

We investigate the dynamics of both quantum discord and concurrence within two excitonic qubits embedded in two coupled semiconductor quantum dots independently interacting with dephasing reservoirs. Their behavior in both Markovian and non-Markovian environments is explored against dimensionless time and temperature. Moreover, the effects of the external electric field on these correlations as well as the effects related to the Förster interaction are extensively analyzed. We show that the non-Markovian behavior of quantum correlations is always preserved under the variation of the electric field and the Förster interaction, regardless of the strong influence of these two parameters on the amount of quantum correlations. Furthermore, we show that nonzero discord can still be observed for large values of temperature and dimensionless time, unlike concurrence which vanishes in this regime.
Over the past decade, an increasing number of studies focused on investigating coupled semiconductor quantum dots [150, 151, 152], mainly because of the relevance of their electro-optical properties[153, 154]. Many different parameters are candidates for the study of these properties, among them, the exciton-exciton interaction is one of the most interesting parameters. This type of interaction in first neighbors dots will enable to carry out of a scheme for quantum information processing on semiconductor quantum dots [155]. So much effort has been taken to address the quantum correlation dynamics of the coupled semiconductor quantum dots. Along this direction, Fanchini et al investigated the quantum correlation dynamics of two coupled double semiconductor quantum dots with the interaction between the qubits of the thermal bath [156]. In real quantum systems which are easily affected by their environments [157], decoherence destroys the quantumness of the system and decreases the useful quantum correlations between the different components of the system. This decoherence is the main obstacle for the implementation of quantum information processing. It is worth noting that many studies have dealt with the dynamical behavior of quantum correlations under the effect of decoherence. Particularly the study of the quantum correlations under the influence of both Markovian and non-Markovian environments has attracted a lot of attention [158, 159].
In This paper, we investigate quantum correlations between two excitonic qubits inside two coupled semiconductor quantum dots that independently interact with dephasing reservoirs. The excitonic qubits are modeled by dipoles in each quantum dot. The variation of the quantum correlations is processed as a function of temperature and the dimensionless time in both Markovian and non-Markovian environments. Our main purpose is to analyze the external electric field and the Förster interaction effect on the amount of entanglement and quantum discord measured in our system as well as on their dynamical behavior. Indeed, we show that, although the quantum correlations amount is influenced by the variation of the electric field and the Förster interaction, their non-Markovian behavior is still preserved under the

effects of these two parameters. Moreover, we show that for large values of temperature and time, quantum discord still survives while entanglement vanishes.

### 3.2.2 The model of InAs quantum dots

In order to address the quantum correlations properties of optically driven semiconductor quantum dots, we use a model sample in which we consider a series of InAs coupled semiconductor quantum dots with small equal spacing between them along the axis. Our work constitutes a theoretical study of the model of two coupled double quantum dots. It was shown in references [160, 161] that this system can be described by the model described below. The latter can be experimentally implemented using an array of InAs coupled quantum dots. We assumed the energy parameter $\hbar\Omega$, $\hbar\omega$ and $\hbar J_z$ to be of the order of meV, which is consistent with experimental observations.

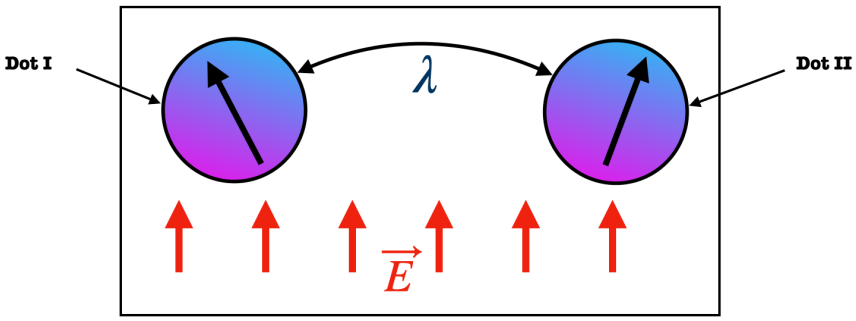


FIGURE 3.2: schematic representation of two coupled semiconductor InAs quantum dots.

In this model, to explain the energy transfer between semiconductor quantum dots through dipolar interaction between the excitons we rely on the Förster mechanism [162]. In this case, the qubits are the excitonic electric dipole moments located in each quantum dot which can only orient along ($|0\rangle$) or against ($|1\rangle$) the external electric fields.

The Hamiltonian of the system in the presence of an external electric field ($\vec{E}$) is given by,

$$H = \hbar\sum_{i=1}^{n}\omega_i[S_z^i+\frac{1}{2}]+\hbar\sum_{i=1}^{n}\Omega_i S_z^i+\hbar\sum_{\substack{i,j=1\\ i\neq j}}^{n}J_z[S_z^i+\frac{1}{2}][S_z^j+\frac{1}{2}]+\frac{1}{2}\sum_{\substack{i,j=1\\ i\neq j}}^{n}\lambda[S_+^iS_-^j+S_-^jS_+^i], \tag{3.22}$$

with n is the number of coupled quantum dots, $S_+^i = \begin{pmatrix}0 & 0\\ 1 & 0\end{pmatrix}$, $S_-^i = \begin{pmatrix}0 & 1\\ 0 & 0\end{pmatrix}$ and $S_z^i = \frac{1}{2}\begin{pmatrix}1 & 0\\ 0 & -1\end{pmatrix}$.

In equation (3.22), $\omega_i$ denotes the frequency of the excitons in the semiconductor quantum dots, and $\Omega_i$ the frequency related to the excitonic dipole moment that is a function of the dipole moment and the external electric field ($\vec{E}$) at the quantum dot number $i$,

$$\hbar\Omega_i = |\vec{d}.\vec{E}|, \tag{3.23}$$

with $\vec{d}$ being the electric dipole moment associated with the exciton; it is supposed to be the same for each quantum dot. $\lambda$ is the Förster interaction which transfers an exciton from one

quantum dot to another, and $J_z$ is the exciton-exciton dipolar interaction energy. For two dipoles $i$ and $j$, along the $z$-axis and separated by a distance $r_{ij}$, it is given by

$$\hbar J_z = \frac{\vec{d^2}(1 - 3\cos\theta)}{\vec{r_{ij}^3}}. \tag{3.24}$$

Or $\theta$ is the angle between the dipoles.
The state of the system, when under canonical thermal equilibrium, at temperature $T$ is described by the density matrix

$$\rho = \frac{1}{Z} exp[-\beta H], \tag{3.25}$$

where $\beta = (k_B T)^{-1}$, $k_B$ being the Boltmann constant and $T$ the temperature. The partition function $Z$ is given by

$$Z(T) = Tr(exp[-\beta H]), \tag{3.26}$$

$$= \sum_{i=1}^{N} g_i e^{-\beta E_i}. \tag{3.27}$$

$E_i$ being the eigenvalues of the Hamiltonian, and $g_i$ is the degeneracy.

In order to evaluate the time and temperature-dependent quantum correlation, we define the non-Markovian dephasing model, introduced by Daffer et al. [163]. This model has been widely used recently for the study of quantum correlations dynamics [136, 164, 165]. In this work, we use it to address quantum correlations dynamics in double semiconductor quantum dots. We consider a colored noise dephasing model with dynamics described by the following master equation [163, 136]

$$\dot{\rho}(T) = K\mathcal{L}\rho(T), \tag{3.28}$$

where the dot denotes the time derivative and $K$ is a time-dependent operator given by

$$K\phi = \int_0^t k(t - \acute{t})\phi(\acute{t})d\acute{t}, \tag{3.29}$$

where the kernel $k(t - \acute{t})$ is related to the memory type existing in the environment while $\mathcal{L}$ denotes the Lindblad super-operator describing the open system dynamics.

In our case, we consider a two-level system interacting with an environment having the properties of random telegraph signal noise, which can be implemented using the time-dependent Hamiltonian [163, 136],

$$H(t) = \hbar \sum_{k=1}^{3} \Gamma_k(t)\sigma_k, \tag{3.30}$$

where $\sigma_k$ are the Pauli matrices and $\Gamma_k$ (t) are independent random variables that obey random telegraph signal statistics. These random variables can be taken in the form $\Gamma_k(t) = a_k n_k(t)$, where $n_k(t)$ has a Poissonian distribution with a mean equal to $\frac{t}{2\tau_k}$ and $a_k$ is an independent random variable, which with an abuse of notation, we say that it takes the values $\pm a_k$.

Solving the von Neumann equation of motion of the density operator

$$\dot{\rho}(T) = -(i/\hbar)[H, \rho(T)] = -i \sum_k \Gamma_k(t)[\sigma_k, \rho(T)],$$

Yields the solution

$$\rho(t,T) = \rho(0,T) - i \int_0^t \sum_k \Gamma_k(s)[\sigma_k, \rho(s,T)]ds. \tag{3.31}$$

Substituting it back into the von Neumann equation and performing a stochastic average, leads to

$$\dot{\rho}(t,T) = -\int_0^t \sum_k \exp(-\left|t-\acute{t}\right|/\tau_k) a_k^2 [\sigma_k, [\sigma_k, \rho(\acute{t},T)]]d\acute{t}, \tag{3.32}$$

where $< \Gamma_j(t)\Gamma_k(\acute{t}) >= a_k^2 \exp(-\left|t-\acute{t}\right|/\tau_k)\delta_{jk}$ is the memory kernel obtained from the correlation functions of a random telegraph signal.
The conditions in which the dynamical evolution created by Eq. 3.30 is wholly non-negative have been analyzed by Daffer et al. [163] and it was shown that complete positivity is preserved only when two of the $a_k$'s are zero. Physically this corresponds to the case where the noise acts in one direction only. In particular choosing the conditions $a_1 = a_2 = 0$, and $a_3 = a$, describes a system in which the dynamics are that of a dephasing channel with colored noise. Hence, the Kraus super-operators that describe the dynamics of the two-level system are given by [163, 136],

$$M_1 = \sqrt{\frac{1+\Lambda(\nu)}{2}} I_2, \tag{3.33}$$

$$M_2 = \sqrt{\frac{1-\Lambda(\nu)}{2}} \sigma_3, \tag{3.34}$$

where $I_2$ is the $(2 \times 2)$ identity matrix. It is easy to check that the Kraus operators satisfy the condition $M_i(t)$ satisfy $\sum_i M_i^\dagger(t) M_i(t) = I$. In (3.33) and (3.34) $\Lambda(\nu) = e^{-\nu}[\cos(\mu\nu) + \sin(\mu\nu)/\mu]$, with $\mu = \sqrt{(4a\tau)^2 - 1}$ and $\nu = \frac{t}{2\tau}$ is the dimensionless time.
We note that the function $\Lambda(\nu)$ has two regimes fluctuate by changing the parameter $a\tau$, when $0 \leq a\tau < 1/4$, the frequency $\mu$ is purely imaginary, so the solution is represented by pure damping, for $a\tau = 1/4$, $\Lambda(\nu)$ is equal unity at the initial time and zero when time approaches infinity. On the other hand, when $a\tau > 1/4$, the frequency $\mu$ is real so the solution is represented by damped oscillations.
Since we intend to study the dynamics of a two, two-level quantum system (two quantum dots), the time evolution of an initial density operator, $\rho_{AB}(0,T)$, can be expressed as

$$\rho_{AB}(t,T) = \sum_{i,j} (M_i^A \otimes M_j^B) \rho_{AB}(0,T) (M_i^A \otimes M_j^B)^\dagger \tag{3.35}$$

where the Kraus operators $M_i^A$ and $M_i^B$ act, respectively, on the first and the second qubit.

The time and temperature-dependent density matrix is then expressed on the basis of the eigenvectors of the Hamiltonian as

$$\rho_{AB}(t,T) = \begin{pmatrix} \rho_{11} & 0 & 0 & 0 \\ 0 & \rho_{22} & \rho_{23} & 0 \\ 0 & \rho_{32} & \rho_{33} & 0 \\ 0 & 0 & 0 & \rho_{44} \end{pmatrix}.$$

With,

$$\rho_{11} = \frac{1}{e^{\beta(-\lambda+2\hbar Jz+\hbar\omega+\hbar\Omega)} + e^{\beta(\lambda+2\hbar Jz+\hbar\omega+\hbar\Omega)} + e^{2\beta(\hbar Jz+\hbar\omega+\hbar\Omega)} + 1},$$

$$\rho_{22} = \frac{\left(e^{2\beta\lambda}+1\right) e^{\beta(-\lambda+2\hbar Jz+\hbar\omega+\hbar\Omega)}}{2\left(e^{\beta(-\lambda+2\hbar Jz+\hbar\omega+\hbar\Omega)} + e^{\beta(\lambda+2\hbar Jz+\hbar\omega+\hbar\Omega)} + e^{2\beta(\hbar Jz+\hbar\omega+\hbar\Omega)} + 1\right)},$$

$$\rho_{33} = \frac{\left(e^{2\beta\lambda}+1\right) e^{\beta(-\lambda+2\hbar Jz+\hbar\omega+\hbar\Omega)}}{2\left(e^{\beta(-\lambda+2\hbar Jz+\hbar\omega+\hbar\Omega)} + e^{\beta(\lambda+2\hbar Jz+\hbar\omega+\hbar\Omega)} + e^{2\beta(\hbar Jz+\hbar\omega+\hbar\Omega)} + 1\right)},$$

$$\rho_{44} = \frac{e^{2\beta(\hbar Jz+\hbar\omega+\hbar\Omega)}}{e^{\beta(-\lambda+2\hbar Jz+\hbar\omega+\hbar\Omega)} + e^{\beta(\lambda+2\hbar Jz+\hbar\omega+\hbar\Omega)} + e^{2\beta(\hbar Jz+\hbar\omega+\hbar\Omega)} + 1},$$

$$\rho_{23} = -\frac{\left(e^{2\beta\lambda}-1\right)\left(\sqrt{16a^2\tau^2-1}\sin\left(2\nu\sqrt{16a^2\tau^2-1}\right) + \left(8a^2\tau^2-1\right)\cos\left(2\nu\sqrt{16a^2\tau^2-1}\right) + 8a^2\tau^2\right) e^{\beta(-\lambda+2\hbar Jz+\hbar\omega+\hbar\Omega)-2\nu}}{2\left(16a^2\tau^2-1\right)\left(e^{\beta(-\lambda+2\hbar Jz+\hbar\omega+\hbar\Omega)} + e^{\beta(\lambda+2\hbar Jz+\hbar\omega+\hbar\Omega)} + e^{2\beta(\hbar Jz+\hbar\omega+\hbar\Omega)} + 1\right)},$$

and

$$\rho_{32} = -\frac{\left(e^{2\beta\lambda}-1\right)\left(\sqrt{16a^2\tau^2-1}\sin\left(2\nu\sqrt{16a^2\tau^2-1}\right) + \left(8a^2\tau^2-1\right)\cos\left(2\nu\sqrt{16a^2\tau^2-1}\right) + 8a^2\tau^2\right) e^{\beta(-\lambda+2\hbar Jz+\hbar\omega+\hbar\Omega)-2\nu}}{2\left(16a^2\tau^2-1\right)\left(e^{\beta(-\lambda+2\hbar Jz+\hbar\omega+\hbar\Omega)} + e^{\beta(\lambda+2\hbar Jz+\hbar\omega+\hbar\Omega)} + e^{2\beta(\hbar Jz+\hbar\omega+\hbar\Omega)} + 1\right)}.$$

### 3.2.3 Results and discussions

We investigate the behavior of the quantum correlations present in two coupled semiconductor quantum dots independently interacting with dephasing reservoirs. In figure 3.3 we plotted the evolution of both concurrence and discord for different values of $\tau$ against the parameter $\frac{t}{2\tau}$ when the electric field is zero (fig.3.3 (a, b,d,e)) and also when the electric field is on $(E = 20 \times 10^6 V/m)$, that coincide to the value of $\hbar\Omega = 2.5\, meV$ (fig.3.3 (c,f)). Moreover, in order to process the effects of Förster interaction on the correlations present in our system we plotted in figure 3.4 their dynamical behavior for different values of this parameter in a non-Markovian regime.

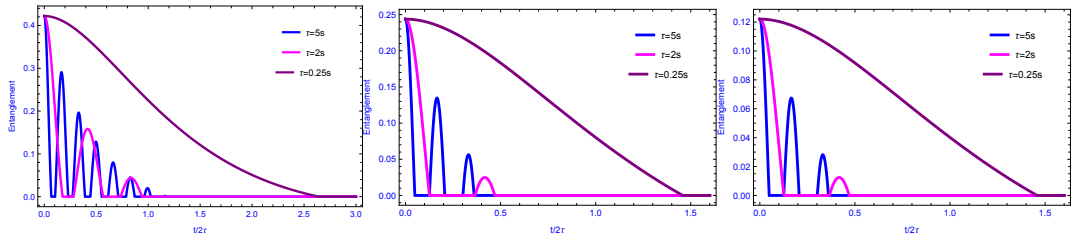


(A) $\hbar\Omega = 0\,meV$ and $T = 15K$.

(B) $\hbar\Omega = 0\,meV$ and $T = 25K$.

(C) $\hbar\Omega = 2.5\,meV$ and $T = 25K$.

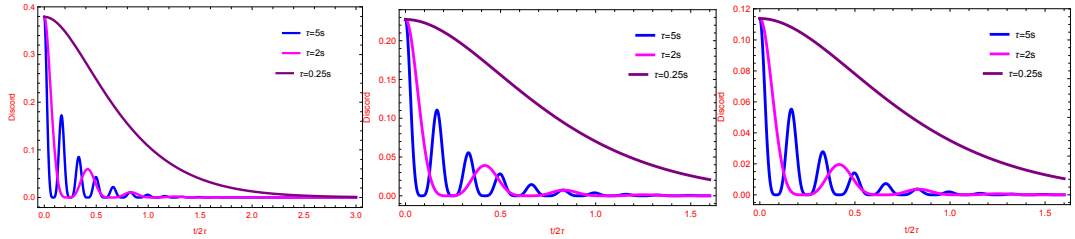


(D) $\hbar\Omega = 0\,meV$ and $T = 15K$.

(E) $\hbar\Omega = 0\,meV$ and $T = 25K$.

(F) $\hbar\Omega = 2.5\,meV$ and $T = 25K$.

FIGURE 3.3: Entanglement and Discord as a function of $\frac{t}{2\tau}$ for different values of $\tau$ with $\lambda = 2\,meV$, $J_z = \hbar\omega = 2meV$, and $a = 0.95s$.

Figures 3.3a, 3.3b, 3.3d, and 3.3e show how quantum correlations behave against the dimensionless time for two different values of temperatures when the electric field is absent. For the non-Markovian regime ($\tau = 2s$ and $\tau = 5$), one can observe that the quantum correlations (both entanglement and quantum discord) exhibit death and revival with a continuous damped amplitude. This is due to the environmental memory effects which lead to increased information back-flow. While for the Markovian regime (i.e. $\tau = 0.25$), correlations are decreasing asymptotically to zero with increasing time without any revival. This behavior is explained by the fact that the quantum information will very quickly outflow from the system to the environment because of the weak system-environment coupling and the memoryless transfer of information. Moreover, for the non-Markovian regime, one can observe that whenever the degree of non-Markovianity $\tau$ decreases, the frequency of the oscillations in the correlation function is also decreased and delayed, as well as the amplitude of this correlation function.

In the Markovian case, a change in the parameter $\tau$ doesn't affect much the behavior of quantum correlations. The change that occurs when $\tau$ is decreased is due to the fact that information lasts in the system for a longer period of time. For this reason only one curve is plotted in this case. Furthermore, it is seen that, the amount of quantum correlations decreases as we increase the temperature (Figures 3.3b and 3.3e). Additionally, one can remark from (Figures 3.3a and 3.3b ) that the temperature does affect the life time of quantum entanglement. For instance, when $T = 15k$ the entanglement persists for a longer period of time compared to when $T = 25K$, where it vanishes quickly. On the other hand, the life time of quantum discord doesn't change much with temperature (Figures 3.3d and 3.3e ). One can also notice that for large values of dimensionless time and higher temperature $(T = 25K)$ nonzero discord can still be observed, unlike concurrence which vanishes. This shows the

resistance of quantum discord in comparison to entanglement.

On the other hand, Figures 3.3c and 3.3f show that when the applied electric field is on, quantum correlations behave in a similar manner, however with smaller amplitudes, as the plots of Figures 3.3b and 3.3e, obtained when the electric field is off. This is due to the tendency of all dipoles to align in one direction when the external electric field is applied. this results in an increasing dipole-dipole repulsive interaction that forthwith causes the reduction of Coulomb-induced correlations.

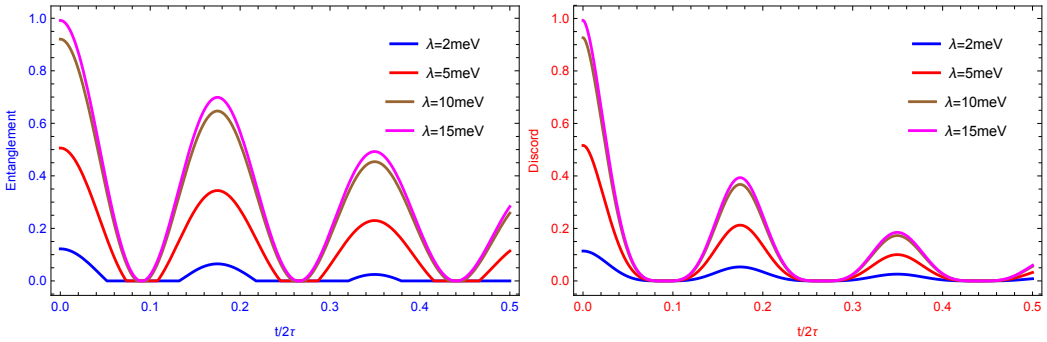


FIGURE 3.4: Entanglement and Discord as a function of $\frac{t}{2\tau}$ for different values of $\lambda$, described by the parameters $\tau = 5s$, $T = 20K$, $\hbar\omega = J_z = 2meV$, $a = 0.95s$ and $\hbar\Omega = 2.5meV$

In Figure 3.4 which displays the dynamics of quantum correlations for different values of Förster interaction $\lambda$ when the electric field is on, one can observe that the amount of quantum correlations increases with $\lambda$. This increase can be resulted from the increasing excitonic interaction. It is worthwhile noting that the quantum correlations preserve their non-Markovian behavior under the Förster interaction effects and the electric field effects as obsereved in Figure 3.3.

Now, in order to study the evolution of quantum correlations more rigorously, we plotted their 3D dynamical behavior against the dimensionless time $\frac{t}{2\tau}$ and the temperature $T$ in Fig. 3.5, as well as against the Förster interaction $\lambda$ and $\hbar\Omega$ in Fig. 3.6 in the non-Markovian case; $\tau = 5s$ and $a = 0.9s$.

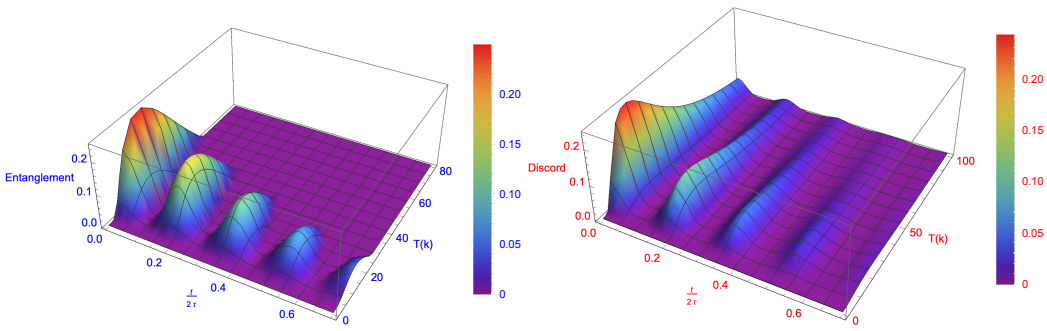


FIGURE 3.5: Entanglement and Discord with respect to $T$ and $\frac{t}{2\tau}$, for $\tau = 5s$, $\lambda = 3\,meV$, $\hbar\omega = J_z = 2meV$ and $\hbar\Omega = 2.5\,meV$.

It is clearly seen that both concurrence and discord decay with temperature and dimensionless time while exhibiting death and revival. This decay is due to the thermal relaxation effects and environment effects, respectively. For smaller temperatures, one can remark that both quantum discord and concurrence increase until reaching their maximum values then

decrease gradually with temperature without any revival as expected. However, one can remark that for higher values of temperature discord still survives while concurrence vanishes. As a matter of fact, one can again assert that quantum discord is more robust than concurrence against temperature. On the other hand, As it is seen in Figure 3.3 one can observe that quantum correlations behavior against time presents some collapses and revivals because of the environment memory effects.

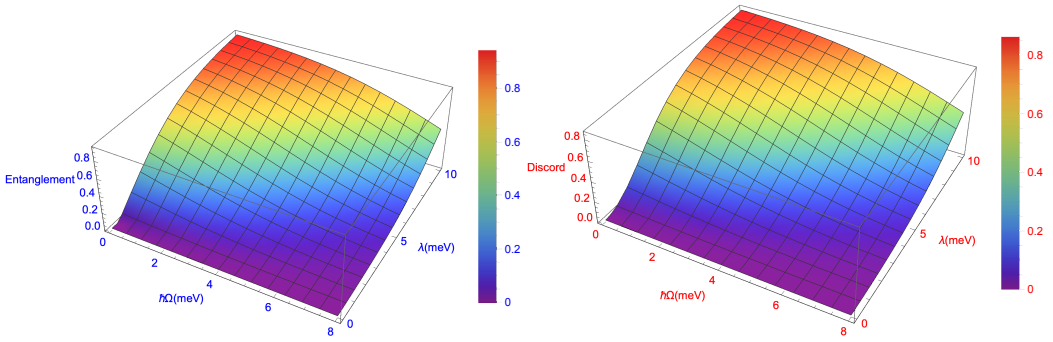


FIGURE 3.6: Entanglement and Discord as a function of $\lambda$ and $\hbar\Omega$, for $\tau = 5s$, $T = 25K$ and $\frac{t}{2\tau} = 0.01$.

The plots in Figure 3.6 show that whenever we increase the parameter $\hbar\Omega$ the amount of both quantum discord and concurrence decreases. This decrease can be explained in terms of the increasing dipolar repulsive interaction as all the dipoles become parallel under effect of the electric field. Moreover, the figures show that for larger values of $\hbar\Omega$ these correlations increase slowly with the Förster interaction, otherwise for smaller values of $\hbar\Omega$ these correlations increase rapidly with the Förster interaction, In fact, one can state that increasing the electric field perturbs the effect of Förster interactions on quantum correlations.

### 3.2.4 Conclusion

In this work, we have investigated the variation of quantum discord and entanglement in the array of two optically driven coupled semiconductor quantum dots independently interacting with dephasing reservoirs. Each quantum dot has an exciton that can be modeled by an electric dipole.

We have shown that the amount of quantum correlations increases upon increasing the Förster interaction and diminishes whenever we switch the electric field on. Moreover, we have shown that this amount increases and reaches its maximal value at very low temperatures and dimensionless time regions then decreases and decays with increasing these two parameters due to the thermal relaxation effects and environmental effects. However, we have observed that despite the fact that concurrence vanishes for large values of temperature and dimensionless time quantum discord still survives, which is consistent with the fact that discord quantifies quantum correlations beyond entanglement. In this direction, we have concluded that, although the quantum correlations amount is influenced by the electric field effects and the Förster interaction effects, their non-Markovian behavior is still preserved under these two effects.

## 3.3 Contribution 3: Wigner Function as a Detector of Entanglement in Open Two Coupled InAs Semiconductor Quantum Dots

In this section, We tested the ability of the Wigner function to reveal and capture the quantum entanglement present in two coupled semiconductor InAs quantum dots that independently interact with dephasing reservoirs. In this respect, we analyze their evolution against the temperature parameter as well as against the dimensionless time in both Markovian and non-Markovian environments. Further, we compare their amounts and their behaviors under the Forster interaction effect. In particular, we show that for large values of dimensionless time and at higher temperatures, unlike the full disappearance of entanglement, the positive part of the Wigner function still survives. Moreover, we show that the Wigner function volume is influenced by the variation of the Forster interaction, the temperature, and the non-Markovianity degree. Nevertheless, its ability to reveal the quantum entanglement present inside two coupled semiconductor quantum dots is still kept.

### 3.3.1 Wigner function

Wigner function is regarded as a natural signature of the quantumness of single mode states Furthermore, its negativity is considered as a measure of quantum entanglement in both closed and open systems In this work, our purpose is to check whether the Wigner function detects the existence of quantum entanglement present in optically driven semiconductor quantum dots. For a system described by the density matrix $\rho$, the Wigner function is defined by

$$W(q,p) = \frac{1}{2\pi}\int_{-\infty}^{\infty} dy\ \mathrm{e}^{-ipy}\langle q+\frac{y}{2}|\rho|q-\frac{y}{2}\rangle, \tag{3.36}$$

or with the appropriate change of variables as:

$$W(q,p) = \frac{1}{\pi}\int_{-\infty}^{\infty} dy\ \mathrm{e}^{2ipy}\langle q-y|\rho|q+y\rangle. \tag{3.37}$$

It satisfies the normalization condition,

$$\int\int W(q,p)dqdp = 1. \tag{3.38}$$

Generally, according to the references, the Wigner function of two-mode state is obvious and yields:

$$W(q_1,p_1,q_2,p_2) = W(q_1,p_1)\ W(q_2,p_2), \tag{3.39}$$

The Wigner function $W_i$ for the two mode states ;
$|+,+\rangle\langle+,+|\ ,|+,-\rangle\langle+,-|\ ,|-,+\rangle\langle+,-|\ ,|+,-\rangle\langle-,+|\ ,|-,+\rangle\langle-,+|\ ,and|-,-\rangle\langle-,-|$,
are respectively given by,

$$W_1 = W_{(++)_\alpha}(q_1,p_1)W_{(++)_\alpha}(q_2,p_2), \tag{3.40}$$
$$W_2 = W_{(+-)_\alpha}(q_1,p_1)W_{(+-)_\alpha}(q_2,p_2), \tag{3.41}$$
$$W_3 = W_{(-+)_\alpha}(q_1,p_1)W_{(+-)_\alpha}(q_2,p_2), \tag{3.42}$$
$$W_4 = W_{(+-)_\alpha}(q_1,p_1)W_{(-+)_\alpha}(q_2,p_2), \tag{3.43}$$
$$W_5 = W_{(-+)_\alpha}(q_1,p_1)W_{(-+)_\alpha}(q_2,p_2), \tag{3.44}$$
$$W_6 = W_{(--)_\alpha}(q_1,p_1)W_{(--)_\alpha}(q_2,p_2). \tag{3.45}$$

It is interesting to notice that the coherent states are not mutually orthogonal and they become so for very large values of the coherent amplitude $\alpha$. Indeed, For $\alpha >>> 2$ we have $(|\pm\rangle = |\pm\alpha\rangle)$ where the normalization constants $N_\alpha^\pm \longrightarrow 1$. Hence, $W_i$ defined in equations ((3.40) - (3.45)) can be rewritten as,

$$\begin{aligned}
W_1(q_1,p_1,q_2,p_2) &= W_{\alpha\,\alpha}(q_1,p_1)W_{\alpha\,\alpha}(q_2,p_2), && (3.46)\\
W_2(q_1,p_1,q_2,p_2) &= W_{\alpha\,\alpha}(q_1,p_1)W_{-\alpha\,-\alpha}(q_2,p_2), && (3.47)\\
W_3(q_1,p_1,q_2,p_2) &= W_{-\alpha\,\alpha}(q_1,p_1)W_{\alpha\,-\alpha}(q_2,p_2), && (3.48)\\
W_4(q_1,p_1,q_2,p_2) &= W_{\alpha\,-\alpha}(q_1,p_1)W_{-\alpha\,\alpha}(q_2,p_2), && (3.49)\\
W_5(q_1,p_1,q_2,p_2) &= W_{-\alpha\,-\alpha}(q_1,p_1)W_{\alpha\,\alpha}(q_2,p_2), && (3.50)\\
W_6(q_1,p_1,q_2,p_2) &= W_{-\alpha\,-\alpha}(q_1,p_1)W_{-\alpha\,-\alpha}(q_2,p_2). && (3.51)
\end{aligned}$$

Where,

$$W_{ij}(q,p) = \sqrt{\pi}\exp\Big[-(p^2)+(I\sqrt{2}p(\alpha_j-\alpha_i^*))-(\frac{1}{2}(|\alpha_i|^2+|\alpha_j|^2))-q^2+(\sqrt{2}q(\alpha_j+\alpha_i^*))-(\alpha_i^*\alpha_j)\Big]. \tag{3.52}$$

We note that $q$ and $p$ are position and momentum respectively.

Indeed, the thermal Wigner function $W(\rho(T))$ and the time and temperature dependent Wigner function $W(\rho(t,T))$ are expressed respectively as:

$$\begin{aligned}
W(\rho(T)) = \rho_{11}W_1(q_1,p_1,q_2,p_2) + \rho_{22}W_2(q_1,p_1,q_2,p_2) + \rho_{23}W_3(q_1,p_1,q_2,p_2)\\
+\rho_{32}W_4(q_1,p_1,q_2,p_2) + \rho_{33}W_5(q_1,p_1,q_2,p_2) + \rho_{44}W_6(q_1,p_1,q_2,p_2).
\end{aligned} \tag{3.53}$$

$$\begin{aligned}
W(\rho(t,T)) = \gamma_{11}W_1(q_1,p_1,q_2,p_2) + \gamma_{22}W_2(q_1,p_1,q_2,p_2) + \gamma_{23}W_3(q_1,p_1,q_2,p_2)\\
+\gamma_{32}W_4(q_1,p_1,q_2,p_2) + \gamma_{33}W_5(q_1,p_1,q_2,p_2) + \gamma_{44}W_6(q_1,p_1,q_2,p_2).
\end{aligned} \tag{3.54}$$

### 3.3.2 Comparison of Wigner function and entanglement in time and temperature dependent system

We investigate comparatively entanglement of formation (E) and Wigner function (W) between two excitonic qubits placed inside two coupled semiconductor quantum dots independently interacting with dephasing reservoirs. In Figure 2, we plotted their behavior for the thermal state against the temperature T for different values of Förster parameter $\lambda$. Then, in order to address the evolution of the entanglement and Wigner function for time and temperature-dependent states in both Markovian and non-Markovian environments, we plot in Figure 3 the dynamical behavior of the entanglement and the Wigner function as a function of the dimensionless time $t/2\tau$ for different values of non-Markovian parameter $\tau$ and Förster interaction parameter $\lambda$. We note that $\hbar\Omega = \hbar\omega = 2.5meV$, $J_z = 2.3meV$ and $a = 0.9\,GHz$.

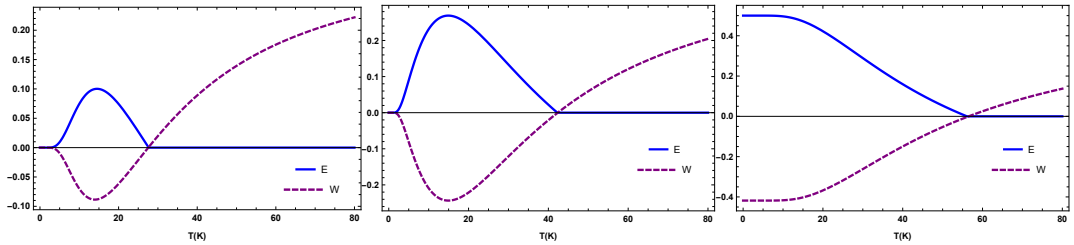


(A) $\lambda$=0 meV (B) $\lambda$=5 meV (C) $\lambda$=15 meV

FIGURE 3.7: Entanglement and Wigner function as a function of $T$ for different values of $\lambda$.

Figures 3.7a, 3.7b and 3.7c show that at very low temperatures entanglement of formation increases until taking their maximum values, then decrease gradually to zero, this is in accord with the fact that quantum correlations decay with temperature due to the thermal effects. Moreover, it is shown from these plots that both the amount of entanglement and the negative volume of the Wigner function increase monotonically once we increase the Förster parameter $\lambda$. This increase can be resulted from the increasing excitonic interaction. Furthermore, it is seen from these plots that, when $\lambda = 0meV$, both the entanglement and the negative volume of the Wigner function are hypersensitive to temperature for this fact one can remark that they last for a shorter period of time, while, when $\lambda = 5meV$ and $\lambda = 15meV$, they last for a longer period of time. As a matter of fact, one can state that the temperatures affect the lifetime of both quantum entanglement and Wigner function, however, the effect of this parameter on these two quantities is perturbed by higher Förster interaction. On the other hand, these figures show that the Wigner function $(W)$ for the thermal density matrix starts being positive exactly at the same point when the entanglement of formation vanishes and it becomes negative whenever this later appears in the system. Furthermore, one can observe that the negative volume of the Wigner function attains its maximum value whenever the amount of entanglement present in the system is maximal. In view of all these remarks, we concluded that the Wigner function can detect and capture the existence of quantum entanglement for temperature-dependent states.

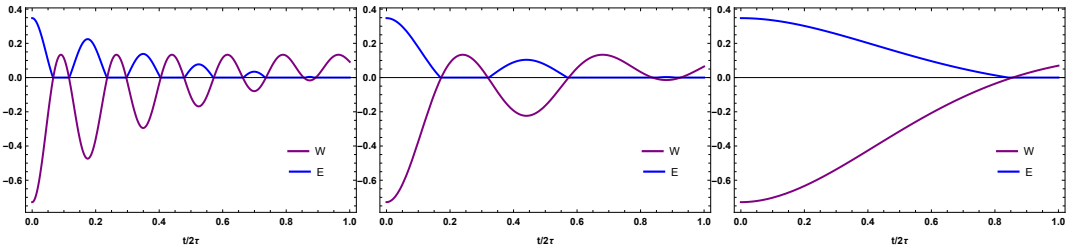


(A) $\lambda$=5 meV, $a = 0.9GHz$ and $\tau = 4ns$

(B) $\lambda$=5 meV, $a = 0.9GHz$ and $\tau = 1ns$

(C) $\lambda$=5 meV, $a = 0.9GHz$ and $\tau = 0.2ns$

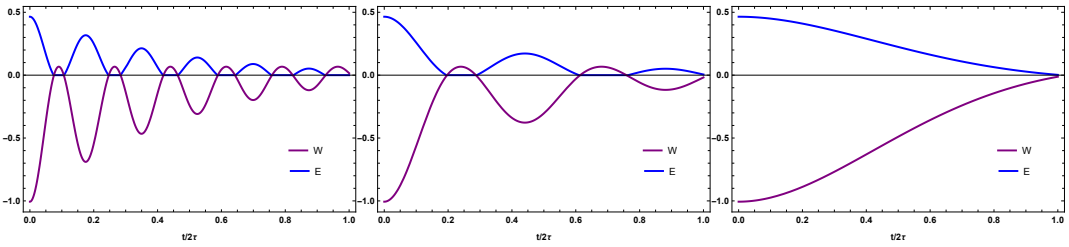


(D) $\lambda$=15 meV, $a = 0.9GHz$ and $\tau = 4ns$

(E) $\lambda$=15 meV, $a = 0.9GHz$ and $\tau = 1ns$

(F) $\lambda$=15 meV, $a = 0.9GHz$ and $\tau = 0.2ns$

FIGURE 3.8: Entanglement of formation and Wigner function as a function of $t/2\tau$ for different values of Förster interaction $\lambda$ and non Markovian parameter $\tau$ with $T = 20K$.

Figures 3.8a, 3.8b, 3.8d, and 3.8e show how quantum entanglement and Wigner function behave comparatively against the dimensionless time for different values of Förster interaction $\lambda$ and non-Markovian parameter $\tau$ . From these figures (i.e. the non-Markovian case), it is seen that both entanglement and Wigner function exhibit collapse and revival with a continuous damped amplitude. This is due to the environmental memory effects which lead to the increase in the information back-flow. On the other hand, from the plots of Figures 3,c, and 3,f (i.e. the Markovian case), it is seen that entanglement of formation is decreasing asymptotically to zero with increasing the dimensionless time without any revival due to the weak system-environment coupling and the memoryless transfer of information. Moreover, one can observe (figures 3.8c and 3.8f) that the negative volume of the Wigner function decreases with the decrease of entanglement until becoming positive when this latter becomes null. Besides, one can remark that whenever the degree of non-Markovianity $\tau$ decreases, the frequency and the amplitude of the oscillations of the entanglement and Wigner function are also decreased and delayed. Additionally, one can remark also that for large values of dimensionless time and at higher temperatures (figures 2 and 3) the positive part of the Wigner function can still be observed, unlike the entanglement of formation which vanishes completely. This indicates the robustness of the Wigner function under the exciton-exciton interaction effects inside two coupled semiconductor quantum dots and proves that its negative part disappears whenever entanglement disappears. Interestingly, it is seen from figure 3.8 that the entanglement of formation and Wigner function preserve their non-Markovian

behavior under the Förster interaction effect. It is seen also that this non-Markovian behavior does not affect the ability of the Wigner function to signal the presence of quantum entanglement for time and temperature-dependent states. Indeed, one can assert that the role of the Wigner function in studying quantum correlation is not influenced by the quantum effects of two coupled semiconductor quantum dots that independently interact with dephasing reservoirs.

### 3.3.3 Conclusion

In this report, we have tested the ability of the Wigner function to capture the quantum entanglement presents in two coupled semiconductor InAs quantum dots that independently interact with dephasing reservoirs. For this aim, we have explored their evolution against the temperature and the dimensionless time parameters. Moreover, we have analyzed comparatively the variation effect of Förster interaction and the non-Markovianity parameter on these two quantities. In this respect, we have shown that for large values of dimensionless time and at higher temperatures the positive part of the Wigner function still survives, unlike the entanglement of formation which vanishes completely. This indicates the robustness of the Wigner function under the exciton-exciton interaction effects inside two coupled semiconductor quantum dots and proves that its negative part disappears whenever entanglement disappears. Additionally, we have shown that despite the fact that the volume of negative and positive parts of the Wigner function is influenced by the variation of the Förster interaction, temperature, and non-Markovianity degree, the ability of this function to signal the existence of quantum entanglement for time and temperature dependent states is not perturbed under the effect of all these parameters. As a matter of fact, we have deduced that whether under the exciton-exciton interaction effects inside two coupled semiconductor quantum dots systems or under its surrounding environment effects, the major role of the Wigner function in studying quantum correlation is still kept.

## 3.4 Contribution 4: Robustness of Wigner function negativity under the exciton-exciton interaction effects inside two coupled semiconductor quantum dots

### 3.4.1 Negativity of Wigner function

We analyze theoretically the Wigner function negativity for thermal density matrix of analogous and equidistant two coupled semiconductor quantum dots at different temperatures. In this respect, we explore the quantum influences of the temperature, the external electric field, the Förster interaction and the exciton-exciton dipole interaction energy on its behavior. In particular, we show that the negativity of Wigner function still survives for large values of temperature ensuring that the non-classicality of the two coupled semiconductor quantum dots system does not get lost under thermal effect. Moreover, we show that this negativity is hypersensitive to the external electric field effect, nevertheless, its sensitivity to this effect is extensively perturbed for higher values of Förster interaction, temperature and exciton-exciton dipole interaction energy. Further, we show that increasing this latter enhances the quantumness of system as the negativity of Wigner function also increases.

The Wigner function, which depends on temperature, describes the state of the InAs coupled quantum dot system (Eq. 3.36) is given by,

$$\begin{aligned} W(\rho(T)) = \rho_{11}W_1(q_1,p_1,q_2,p_2) + \rho_{22}W_2(q_1,p_1,q_2,p_2) + \rho_{23}W_3(q_1,p_1,q_2,p_2) \\ +\rho_{32}W_4(q_1,p_1,q_2,p_2) + \rho_{33}W_5(q_1,p_1,q_2,p_2) + \rho_{44}W_6(q_1,p_1,q_2,p_2). \end{aligned} \tag{3.55}$$

The Wigner function negativity, the non-classicality parameter, between different quadratures of different modes $(p_1, q_2)$ is defined by,

$$\delta(\rho(T)) = \int\int (|W(\rho(T))| - W(\rho(T)))dp_1 dq_2. \tag{3.56}$$

### 3.4.2 Thermal behavior of Wigner function negativity

In this section, we investigate the evolution of the negativity of Wigner function (NW) for the thermal system and we explore the influences of external electric field, the Förster interaction and the exciton-exciton dipole interaction energy on this negativity. For this reason, we plotted its behavior when the electric field is absent (Fig. 1b) and also when it is on (Fig. 3.9 a, c and d ) as a function of temperature T for different values of Förster parameter $\lambda$ (Fig.3.9 a and b ) and as a function of the parameter $\hbar J_z$ for fixed values of temperature and Förster parameter ( Fig.3.9 c and d).

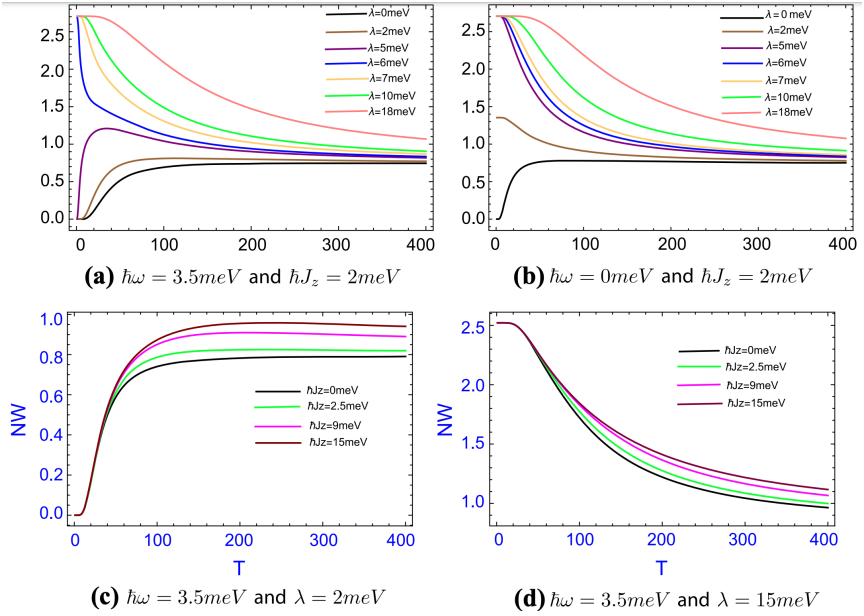


FIGURE 3.9: Negativity of Wigner function as a function of T for different values of $\lambda$ (fig.3.9 a and fig. 3.9 b) and for different values of the coupling $\hbar J_z$ (fig. 3.9 c and fig. 3.9 d).

In Fig. 1a, c and d, when the electric field is activated, it is seen that for weak Förster interaction, the Wigner function negativity increases until a stabilized value is reached for higher temperatures. While, for strong Förster interaction, it decreases progressively with increasing temperature until attained their minimum value. Moreover, one can observe that (Fig. 3.9 a ) for weak or vanish Förster interaction, the negativity vanishes whenever the temperatures is vanishes, nevertheless, for higher Förster inter- action, it takes a higher values even for vanishing temperature. Furthermore, it is seen that when we deactivate the electric field (Fig. 3.9 b ), the behavior of this negativity keeps unchanged for higher temperatures as well as for higher Förster interaction. Whereas, it is seen in Fig. 3.9 a and b that for very low temperatures and weak Förster interaction, it has a apparent effect on it. In this respect, we concluded that the temperature and Förster interaction effects cover up the electric field effect. On the other hand, Fig. 3.9 c and d show that the negativity of Wigner function increases with the increase of the exciton-exciton dipole interaction energy $\hbar J_z$, ; this causes the emergence of the interference pattern, which in turn enhance the amount of quantumness

of the system. It is worthwhile, in addition to all the previous remarks, one can remark from the plots in Fig. 3.9 that the Wigner function negativity still observed at higher temperatures ensuring that the non-classicality of the two coupled semiconductor quantum dots system does not get lost under thermal effect. As a matter of fact, this indicates the relevance and the robustness of Wigner function negativity in the face of all these quantum effects.

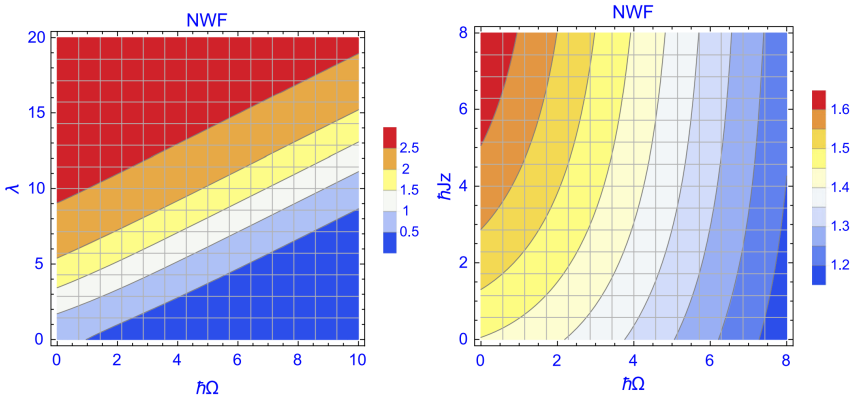


**(a)** $T = 30$ **(b)** $T = 100$

FIGURE 3.10: Negativity of Wigner function as a function of $\hbar\omega$, $\lambda$ and $\hbar J_z$.

With a view to process the effect of $\hbar\omega$, $\lambda$ and $\hbar J_z$ on this function more rigorously we plot its evolution in Fig. 3.10 for a fixed value of temperature against these three parameters. As a matter of fact, the plots of this figure show that the Wigner negativity decreases whenever we increase the parameter $\hbar\omega$. Physically, this decrease is due to the fact that all the dipoles become parallel under effect of the electric field leading to the increasing dipolar repulsive interaction. Besides, Fig. 3.10 b confirms that the increase of the coupling $\hbar J_z$ enhance the non-classicality of the system. Further, it shows that for smaller or vanish values of exciton-exciton dipole interaction energy the decrease of negativity is slowly with the increase of the electric filed, while for higher values of this parameter this decrease gets faster. From Figs. 3.9 and 3.10, one can deduce that the exciton-exciton dipole interaction energy, the Förster interaction and the temperature parameters perturb the electric field effect.

### 3.4.3 Conclusion

In this investigation, we have explored analytically the negativity of Wigner function between two excitonic qubits placed inside two coupled semiconductor quantum dots. In a way, we have tested the robustness of this negativity under effect of the temperature, the external electric field, the exciton-exciton dipole interaction energy and the Förster interaction. We have found that the negativity of Wigner function still survives for large values of temperature reflecting presence of interference patterns in the two coupled semiconductor quantum dots system. As a matter of fact, we have deduced that the non-classicality of this system does not get lost under thermal effect. Furthermore, we have shown that this negativity is hypersensitive to the external electric field effect, nevertheless, it is not sensitive to this effect for higher Förster interaction as well as for higher temperatures. Moreover, we have shown that increasing the exciton-exciton dipole interaction energy enhances the quantumness of system as the negativity of Wigner function also increases. In addition to this, we have found that the effects of exciton-exciton dipole interaction energy, Förster interaction and temperature perturb the electric field effect. This work allows us to describe the most important properties of Wigner function negativity for two coupled semiconductor quantum dots system, which

gives more efficiency in quantum information theory. Moreover, it does represent a major step forward in showing its behavior under the effect of the different physical parameters of this system. In this direction, in order to discover more rigorously the relevance of Wigner function in such type of systems, a new work is in progress. In this future work, we will address the possibility of using this function to detect the presence of quantum entanglement in two coupled quantum dots.

# Chapter 4

# Applications of quantum dots

## 4.1 Quantum dots Lasers

Lasers, originally derived from the acronym "Light Amplification by Stimulated Emission of Radiation," have been revolutionary technologies with profound impacts across diverse domains, including communications, manufacturing, and medicine. Lasers generate highly concentrated and coherent light beams with unique properties, making them indispensable tools in modern science and industry. When it comes to quantum dot lasers (QDLs) (Figure 4.1), we enter a cutting-edge realm of possibilities, as these devices unlock new potential by harnessing the properties of nanoscale semiconductor particles known as quantum dots. These QDLs achieve enhanced performance and flexibility unlike conventional lasers, and utilize one or several layers of quantum dots as the active medium, offering precise control over emitted photons, leading to highly monochromatic light emission and improved stability at varying temperatures. These lasers have already found practical applications in fields such as telecommunications, biological imaging, and quantum computing, underscoring their potential to revolutionize various industries [166]. The integration of laser technology and quantum dots synergistically drives innovation, propelling us toward a future where these advanced devices will take a central role in shaping modern technology and scientific exploration.

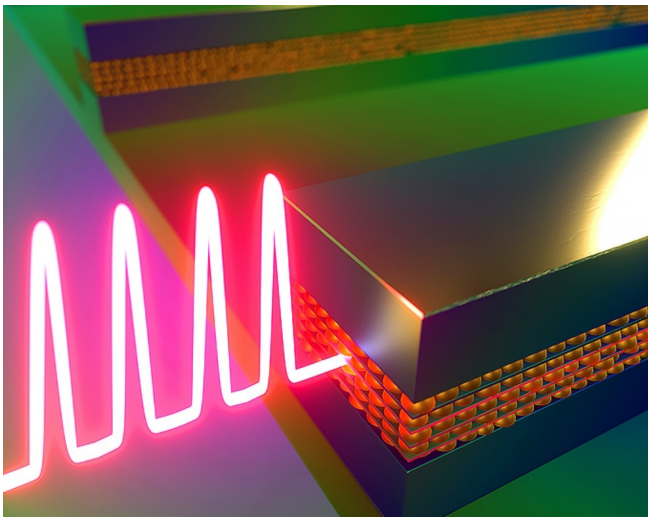

FIGURE 4.1: Quantum dots LASER [5].

In summary, lasers based on quantum dots represent an advanced evolution of classical heterojunction and double heterojunction devices, as well as an improved extension of quantum well lasers. However, some challenges must be addressed to fully harness the potential of

quantum dot lasers. One significant drawback is the size dispersion and the limited ability to precisely control the energy structure of the quantum dots. To achieve truly monochromatic emission, all quantum dots within the active region of the laser must be of the same size, as the energy structure directly influences the wavelength of the emitted photons. Hence, a thorough understanding of the relationship between the energy structure and the size of quantum dots is essential to tailor their size for specific applications. Despite these challenges, ongoing research and advancements in materials science and fabrication techniques continue to address the issues associated with quantum dot lasers. Improved control over quantum dot size and energy structure will pave the way for even more efficient and versatile laser devices. The prospect of lasers based on quantum dots holds promise for various applications, including communications, sensing, and quantum computing, where their unique properties can bring about groundbreaking innovations in the world of photonics and beyond. As researchers delve deeper into the intricacies of quantum dots and their behavior in laser systems, we can expect further breakthroughs that will solidify quantum dot lasers as indispensable tools in cutting-edge technology and scientific exploration. By leveraging the advantages and overcoming the challenges, the field of laser technology with quantum dot nanostructures is set to continue its remarkable journey of transformation and discovery.

## 4.2 Quantum dot memories

A quantum memory refers to a physical system with the capability to store the state of a qubit and return it for use later. It must retain the entire information contained within the qubit, including any entanglement with other qubits. Unlike classical methods that involve measuring and noting down information, an operational quantum memory cannot adopt such an approach, as it would lead to the destruction of the quantum nature of the encoded information and any existing entanglement with other qubits.

Quantum dot memories have opened up exciting new possibilities and hold potential for innovative computer memory designs. These memories offer long-term storage capabilities similar to flash memory, and the added advantage of electrons remaining trapped within the quantum dots until influenced by tunneling or thermal emission.

In terms of speed, quantum dot memories outshine advanced dynamic random access memory with significantly improved write speeds and the need for weaker electrical fields for writing and erasing. However, their current limitation lies in the maximum operating temperature, which restricts their applicability in specific environments.

Challenges remain in achieving stability and charge persistence against varying temperatures, although progress has been made toward achieving functionality at room temperature. Despite the existing challenges, the enormous potential of quantum dot memories justifies further research.

By developing memory devices with high durability comparable to flash memory and performance matching or exceeding RAM, quantum dot memories could revolutionize data storage. A comprehensive understanding of the intricate carrier exchange between quantum dots and the bulk is essential for grasping the functioning of these devices, particularly their temperature sensitivity and exchange frequency. Electrical space charge tests play a vital role in investigating the physics underlying quantum dot systems, emphasizing the need for a uniform distribution and size of quantum dots to improve measurement precision.

In the realm of quantum repeaters, quantum memories represent the next stage after entanglement-pair sources (EPS). Various approaches, such as solid-state atomic ensembles in rare-earth doped crystals, Nitrogen-vacancy centers in diamond [167], semiconductor quantum dots, and atomic gases at different temperatures, are explored for quantum memories.

The performance of quantum repeaters hinges on efficiency, fidelity, and storage time, with critical consideration given to bandwidth matching between the photon source and memory, particularly for hybrid quantum systems. Quantum memories based on electromagnetically induced transparency and atomic frequency combs have shown promising results, achieving high storage efficiencies and fidelity. However, challenges persist in addressing bandwidth mismatches and noise, which are crucial for effective interfacing with quantum light sources and building efficient, high-speed, and noise-free quantum repeaters. Efforts are ongoing to develop hybrid quantum memories and establish a seamless interface between quantum dots and quantum memory platforms, offering a promising path for advancements in quantum communication and computation.

## 4.3 QDs for Light-Emitting Diodes (LEDs) and Display Applications

Since the 1990s, there has been growing interest in the utilization of quantum dots as a potential lighting source. In the early stages of development, researchers employed quantum dots in light-emitting diodes (LEDs), infrared photodetectors, and single-color light-emitting circuits [94] for imaging applications. It was not until the 2000s that the potential of quantum dots as light sources and display materials was fully recognized [168]. Quantum dots exhibit two distinct emission mechanisms: photoluminescence, where they emit light after absorbing photons (electromagnetic radiation), and electroluminescence, This happens when a potent electric field or current flows through a material that emits light as a result, leading to optical emission.

Quantum dots possess characteristics that make them easily adaptable for use in innovative emissive display devices. Specifically, properly color-filtered quantum dots, known for creating predominantly monochromatic light, have demonstrated their effectiveness, particularly in contrast to traditional white lighting sources. Moreover, they enable the generation of exceptionally vibrant colors that closely align with the Rec.2020 color gamut. The Rec.2020 [20, 21] standard defines various aspects of ultra-high-definition television (UHDTV), including display resolution, frame rates, color depths, color primaries, and more. Display technologies that incorporate quantum-dot light-emitting diodes (QD-LEDs) are referred to as electro-emissive quantum dot displays. These devices share similarities with active-matrix organic light-emitting diodes (OLEDs) and MicroLED displays, as they enable each pixel to directly emit light by passing an electric current through inorganic nanostructured materials. According to proponents of this technology, QLED displays are exceptionally well-suited for applications such as flat-panel television screens, digital cameras, smartphones, and mobile gaming systems. They offer advantages like the ability to handle large, flexible displays and a slower degradation rate compared to OLEDs.

The first organic light-emitting diode structure incorporating quantum dots was explored in 1994, utilizing CdSe quantum dots and polymeric electron transport layers. However, this initial implementation of Quantum-dot LED (QLED) technology exhibited poor performance and required a high threshold voltage due to the limitations of organic semiconductors. Recent developments have introduced a novel colloidal quantum dot-based light-emitting diode with enhanced external quantum efficiencies, utilizing an organic CIM/LiF/Al cathode [169]. In contrast to conventional organic or molecular phosphors used in phosphor-converted LEDs [170], colloidal quantum dots have emerged as a promising emissive material for LEDs. CdSe and InP are among the primary quantum dot nanostructures employed in both industry and academia. Colloidal quantum dots offer several advantages, including narrow spectral

line widths (FWHM of approximately 20-30 nm), high luminescence quantum yield, excellent photostability, functional versatility, and cost-effectiveness. Their narrow spectral characteristics, aligned with the Rec.2020 color gamut criteria, enable the creation of rich and precise color schemes in high-resolution displays.
Quantum dots-based light-emitting diodes are regarded as the next generation of screen displays following organic light-emitting diodes, owing to their high color purity, brightness, and energy efficiency. In these devices, a layer of quantum dots is placed in front of a conventional LED backlight screen. Each tiny quantum dot emits a different color based on its size, typically ranging from two to ten nanometers.
The architecture of a quantum dot-based light-emitting diode device typically involves Indium Tin Oxide (ITO) on a glass or polymeric substrate, followed by a hole transporting layer (HTL), quantum dot deposition, and the subsequent addition of electrodes and an electron transporting layer (ETL). Materials like Ag, Au, and Al are commonly used to create electrodes via thermal evaporation [171, 172, 173, 174]. The emitted colors are primarily determined by the size of the quantum dots, which dictates the wavelength of the generated light.
Samsung asserts that quantum dots can generate more than a billion distinct colors (Figure 4.2), surpassing organic light-emitting diodes in terms of color variety and brightness levels. Quantum light-emitting diodes excel in maintaining color accuracy, even in areas of maximum luminance where organic light-emitting diodes may struggle, offering superior performance in these scenarios.

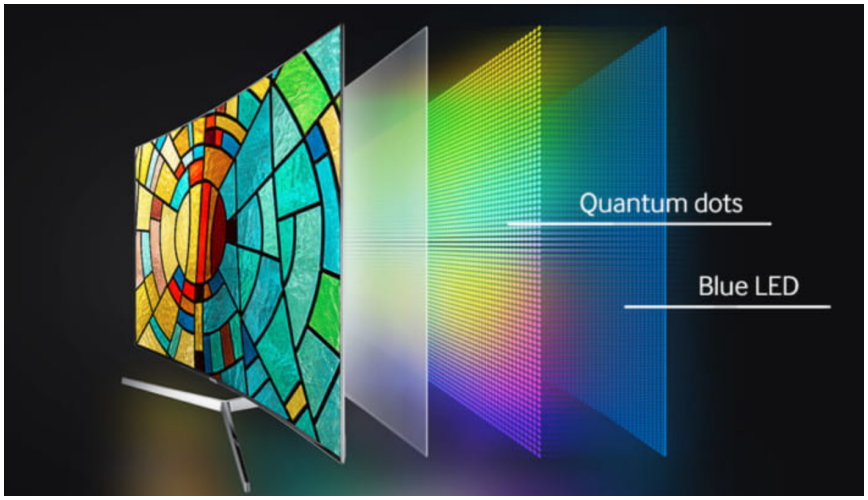


FIGURE 4.2: Quantum Dots Display.

## 4.4 Photovoltaics

Quantum dot solar cells operate similarly to traditional solar cells (Figure 4.3). The primary distinction is the use of quantum dots as the active photovoltaic material, replacing common materials because of their adjustable bandgaps based on size, paving the way for multijunction solar cells.

In standard solar cells, light is absorbed by a semiconductor, producing an electron-hole pair, commonly called an exciton. This pair is separated using an electrochemical potential found in p-n junctions or Schottky diodes. This separation leads to an electric current, driven by the movement of electrons and holes. To create a p-n junction, one side of a semiconductor

interface is doped with electron donors and the other with electron acceptors, leading to an internal electrochemical potential. For an electron-hole pair to be generated, a photon's energy must exceed the material's bandgap. Photons with energies below this threshold can't be absorbed, while those with higher energies, especially from the broad solar spectrum, often lose energy as heat, thereby reducing efficiency. This energy loss affects both current, due to photon absorption limitations, and voltage, due to thermalization. The compromise between voltage and current in semiconductor cells can be mitigated by using multiple junctions.

Quantum dots offer a unique ability to modify their bandgap, making them particularly suited for solar cell applications. In 1989, Burnham and Duggan first suggested using quantum dots to enhance solar cell efficiency [175]. According to the Shockley-Queisser limit, optimal solar conversion occurs in materials with a bandgap of 1.34 eV, considering the sun's photon distribution. However, materials with smaller bandgaps are better for converting low-energy photons to electricity, and vice versa. Lead sulfide (PbS) colloidal quantum dots can be tailored to bandgaps typically hard to achieve with traditional solar cells. Importantly, they can harness the abundant near-infrared solar energy that reaches Earth [176]. PbS quantum dots are especially intriguing for solar photovoltaics due to their wide Bohr exciton radius, which enables bandgap adjustments across the solar spectrum. This flexibility supports the development of multijunction solar cells using a single semiconductor material. In essence, PbS-based quantum dots can span a range of bandgaps. Commonly, a P-type PbS quantum dot film is sequentially layered onto ETL/ITO/glass substrate layers using spin coating [177, 178, 179]. Subsequent steps involve depositing the HTL and either Ag or Au top electrode through thermal or electron beam evaporation methods.

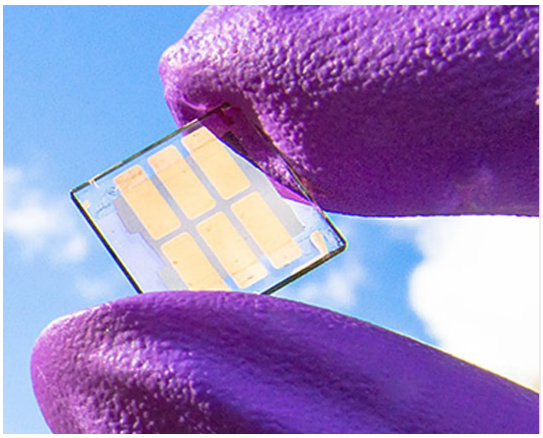

FIGURE 4.3: quantum dots solar cell.

## 4.5 Contribution 5: Quantum dots for quantum heat engines

Heat engines are considered a valuable resource for modern society. The development of these systems leads to the production of heat engines with high efficiency despite their small size, called quantum heat engines. Among these, the quantum Otto cycle which is considered a fundamental thermodynamic cycle in classical heat engines, has also found applications in the realm of quantum heat engines. In this paper, we consider three InAs quantum dots as a working substance, which allows the engine to operate at very small scales, in the presence of an electric field, and the Forster mechanism, which describes the transfer of energy between quantum dots and affects thus the engine's behavior. In this regard, we study the behavior

of the work performed by the engine and the entanglement in the system as the Forster parameter is varied. We find that the work performed by the engine is affected by the Forster interaction and the electric field and that the entanglement in the system also changed as the Forster parameter was changed. Finally, we study the influence of entanglement on the work performed by the engine. We find and discuss the intricate relation between the entanglement and the performance of the engine.

In the last decade, an increasing number of studies have focused on the realization and development of technologies at micro, nano, and atomic scales, using the quantum phenomena with applications in several areas, especially quantum information processing and quantum thermodynamics [180], and quantum technologies. Among these applications, heat engines are considered a valuable resource for modern society. The development of these engines leads to the production realization of heat engines with high efficiency despite their small size, called quantum heat engines [181, 182, 183, 184, 185, 186, 187, 188, 189, 190]. In a quantum heat engine, one can produce work from the heat flow of the system between the hot and the cold thermal bath. Quantum mechanics can describe the operating mechanism of the engine and quantum thermodynamics laws using the quantum version of Carnot, Otto, Stirling, and Diesel Cycles [191, 192, 193, 194]. The choice of the thermodynamic cycle and the working substance is very important to increase the efficiency and the work performed by the engine.

In this paper, we propose three InAs quantum dots in the presence of an external electric field as a working substance of a quantum heat engine. The motivation for this choice is the possibility of realizing it experimentally, and also its high electron mobility [195, 196], which means that electrons can move quickly and efficiently through the material. This is an important feature in nano-scale devices as it allows for fast and accurate controlling. InAs also have a direct band gap [197], which means that they can efficiently absorb and emit light. In addition InAs double quantum dots exhibit a strong Coulomb blockade effect[198], in which the flow of electrons through the quantum dots is strongly suppressed at low temperatures. This can be used to control the flow of electrons to perform quantum operations. Also, the energy levels of InAs can be precisely controlled using electrical gates, allowing for precise manipulation of the quantum system. Since InAs can be easily integrated with other materials, such as GaAs and Si, which are commonly used in electronics, this makes it possible to incorporate InAs quantum dots into a variety of devices.

In this work, we assume that the engine operates following a quantum Otto cycle [199, 200, 201], this latter is a thermodynamic process that converts heat into useful work, just like a classical Otto cycle used in the internal combustion engine. However, the quantum nature of the system allows for the possibility of more efficient and powerful engines. Our objective is to examine the work performed by the heat engine by changing the external electric field in the adiabatic stages, and to study the engine's behavior against the Forster mechanism effects [162]. We also investigate the effect of the temperature of the baths on the efficiency of the quantum heat engine.

### 4.5.1 MODEL AND THE QUANTUM OTTO ENGINE

#### Working substance and thermalization

We propose a quantum system composed of three coupled semiconductors InAs quantum dots with a small space between them [30, 202], as a working substance for the quantum Otto engine (see Figure 4.5). We use the excitonic electric dipole moments as a qubit in each quantum dot, under an external electric field $\vec{E}$, and rely on the Forster mechanism between the excitons to explain the energy transfer between the qubits [162].

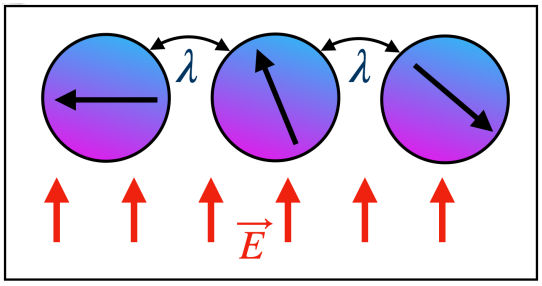


FIGURE 4.4: Schematic of the three quantum dots.

The Hamiltonian of the system, when an electric field $\vec{E}$ is applied, is given by,

$$H = \sum_{i=1}^{3} \hbar\omega_i [S_z^i + \frac{1}{2}] + \sum_{i=1}^{3} \hbar\Omega_i S_z^i + \sum_{\substack{i,j=1 \\ i\neq j}}^{3} \hbar J_z [S_z^i + \frac{1}{2}][S_z^j + \frac{1}{2}] + \frac{1}{2} \sum_{\substack{i,j=1 \\ i\neq j}}^{3} \lambda [S_+^i S_-^j + S_-^j S_+^i], \tag{4.1}$$

with, $S_+^i = (|+\rangle\langle -|)_i$, $S_-^i = (|-\rangle\langle +|)_i$, and $S_z^i = \frac{1}{2}(|+\rangle\langle +| - |-\rangle\langle -|)_i$.

In equation (4.1), $\omega_i$ is the exciton frequency in each quantum dot $i$, $\Omega_i$ is the excitonic dipoles moments frequency which depends on the external electric field ($\vec{E}$), $\lambda$ denote the Forster interaction [203] i.e. resonant energy transfer between the excitons, and $\hbar J_z$ is the static exciton-exciton dipolar interaction energy. When we introduce into our system thermal fluctuations, the state of the system under thermal equilibrium is given by the reduced density matrix,

$$\rho(T) = \frac{1}{Z(T)} e^{-\beta H} = \sum_{i=1}^{4} P_n(T) |\psi_n\rangle\langle\psi_n|, \tag{4.2}$$

Where $P_n(T) = e^{-\beta E_n}/Z(T)$ are the occupation probabilities of the eigenstates $|\Psi_n\rangle$, and $Z(T) = \sum_{i=1}^{n} e^{-\beta E_n}$ is the partition function, with $\beta = \frac{1}{K_B T}$, $K_B$ being the Boltzman constant.

### Quantum Otto cycle

In the following section, we describe the quantum Otto engine cycle, operating in four steps.
**Step 1**: Quantum isochoric process [204]
The working substance with $\Omega = \Omega_H$ is in the initial state $\rho_1$ and is put in contact with a hot bath at temperature $T = T_H$ until it reaches thermal equilibrium. During this step, the system absorbs an amount of heat from the hot bath ($Q_H > 0$). At the end of the process, only the occupation probabilities change to $P_n(T_H)$ while the energy level remains invariant.
**Step 2**: Quantum adiabatic process [204, 205]
The working substance is isolated from the hot bath and the frequency related to the excitonic dipole moment changes from $\Omega_H$ to $\Omega_C$, (with $\Omega_H > \Omega_C$), to satisfy the quantum adiabatic theorem[206, 207]. During this step, the system releases an amount of work, without changing the heat.
**Step 3**: Quantum isochoric process
The working substance with $\Omega = \Omega_C$ now is in contact with a cold bath at temperature $T = T_C$, and after the thermalization of the system, a quantity of heat is released to the cold bath without a change of work, the occupation probabilities change to $P_n(T_C)$.
**Step 4**: Quantum adiabatic process
The working substance is isolated from the cold bath, and the frequency related to the excitonic dipole moment changes from $\Omega_C$ to $\Omega_H$. During this step, an amount of work is done,

but no heat is exchanged. At the end of this step, the working substance returns to the initial condition and is ready for another cycle.

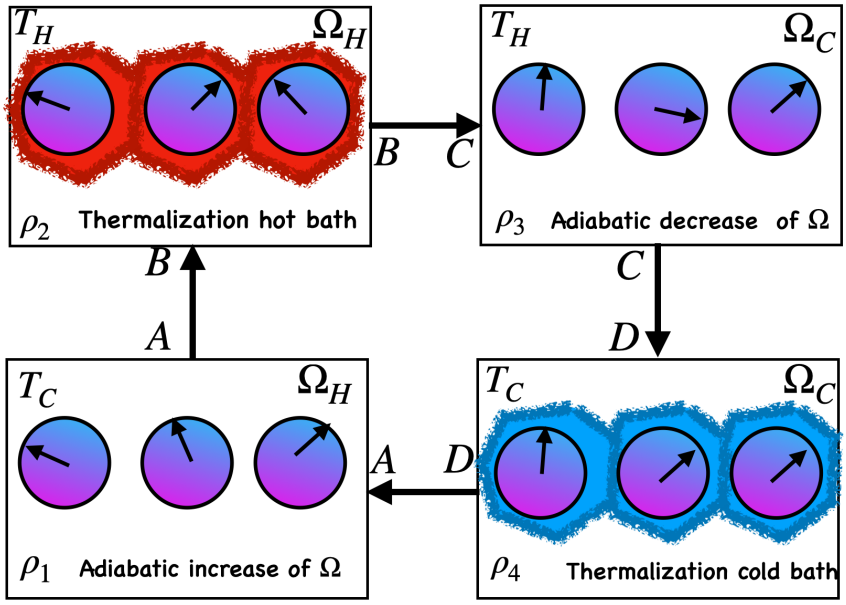


FIGURE 4.5: Schematic diagram of the quantum Otto cycle.

At each step of the described Otto cycle, the state and the energy of the system are given by,

$$\rho_2 = \frac{e^{-\beta_1 H_1}}{Z_1}, \qquad E_2 = Tr\rho_2 H_1, \tag{4.3}$$

$$\rho_3 = U\rho_2 U^+, \qquad E_3 = Tr\rho_3 H_2, \tag{4.4}$$

$$\rho_4 = \frac{e^{-\beta_2 H_2}}{Z_2}, \qquad E_4 = Tr\rho_4 H_2, \tag{4.5}$$

$$\rho_1 = \tilde{U}\rho_4 \tilde{U}^+, \qquad E_1 = Tr\rho_1 H_1, \tag{4.6}$$

where $H_i = H(\Omega_i)$, $Z_i = Tre^{-\beta_i H_i}$, $i = 1, 2$, $U$ and $\tilde{U}$ are unitary operators associated with the second and the fourth steps respectively.

### 4.5.2 Theory

#### The Work performed

In order to describe the work performed and the heat transfer at the quantum level we use the quantum version of the first law of thermodynamics[204, 205],

$$dU = dQ + dW = \sum_n (E_n\, dP_n + P_n\, dE_n). \tag{4.7}$$

In this formula, the heat transfer is related to the change of occupation probabilities, with $dQ = \sum_n E_n\, dP_n$, and the work done is related to the change in energy levels $dW = \sum_n P_n\, dE_n$.

For the engine described in section 2, the heat absorbed during the first step $Q_H$, the heat liberated during the third step $Q_C$, and $'W'$ the net work performed by the engine are defined

by the following expressions:

$$Q_H = \sum_n E_n^H [P_n(T_H) - P_n(T_L)], \tag{4.8}$$

$$Q_C = \sum_n E_n^L [P_n(T_L) - P_n(T_H)], \tag{4.9}$$

$$W = Q_H + Q_C = \sum_n [E_n^H - E_n^L][P_n(T_H) - P_n(T_L)]. \tag{4.10}$$

The energy levels ($E_n^H$ and $E_n^L$) are obtained by replacing $\Omega$ by $\Omega_H$ and $\Omega_C$ during the first and the third steps respectively. We note that the engine can operate in four modes depending on the signs of W, $Q_H$, and $Q_C$[208]:
$[E]$: $Q_H \geq 0$, $Q_C \leq 0$, and $W \geq 0$, in which the machine operates as a quantum heat engine.
$[R]$: $Q_H \leq 0$, $Q_C \geq 0$, and $W \leq 0$, in which the machine operates as a refrigerator.
$[A]$: $Q_H \geq 0$, $Q_C \leq 0$, and $W \leq 0$, in which the machine operates as a thermal accelerator.
$[H]$: $Q_H \leq 0$, $Q_C \leq 0$, and $W \leq 0$, in which the machine operates as a heater.

**Quantum entanglement**

Quantum entanglement was introduced as the most striking phenomenon in quantum physics with no counterpart in classical physics[90]. It is considered a precious resource in several areas of quantum information, quantum computation, quantum communication[23], and their effects in quantum heat engines were established [209, 210, 211, 212, 213, 214]. It is hard to find an exact expression of this quantity for each quantum system, because the type and the classes of entanglement change with changing the dimension of the quantum systems, and the exact expression is available for a few quantum systems. In this regard, many studies focused on the development of general measures of entanglement.

**Concurrence**

For a general two-qubits system, concurrence [215] is a frequently used measure of entanglement. It is defined by,

$$C(\rho) = Max[0, \nu_1 - \nu_2 - \nu_3 - \nu_4], \tag{4.11}$$

where $\nu_i$'s are the square roots of the positive eigenvalues of the matrix $\rho.\tilde{\rho}$ in decreasing order, with $\tilde{\rho}$ being a spin flipped of $\rho$, i.e. $\tilde{\rho} = (\sigma_y \otimes \sigma_y)\rho^*(\sigma_y \otimes \sigma_y)$, $\sigma_y$ and $\rho^*$ being the Pauli matrix and the complex conjugate of $\rho$ respectively.

**Lower bound**

For an arbitrary mixed state of three qubits, the lower bound of concurrence [216] is defined as

$$\tau_3 = \frac{1}{3}\sum_{\alpha}^{6}[(C_\alpha^{12/3})^2 + (C_\alpha^{13/2})^2 + (C_\alpha^{23/1})^2], \tag{4.12}$$

with,

$$C_\alpha^p = max\{0, \lambda(1)_\alpha^p - \lambda(2)_\alpha^p - \lambda(3)_\alpha^p - \lambda(4)_\alpha^p\}, \tag{4.13}$$

in which $\lambda(i)_\alpha^p$ are the square roots of the four nonzero eigenvalues, in decreasing order, of the non-Hermitian matrix $\sqrt{\rho\tilde{\rho}_\alpha}$, with $\tilde{\rho}_\alpha = (L_\alpha \otimes \sigma_y)\rho^*(L_\alpha \otimes \sigma_y)$, and $L_\alpha$ being the generators of $SO(4)$.

$\tau_3$ also characterizes genuine tripartite entanglement that cannot be described by $C(\rho)$ mentioned in 4.11, such that, if $\tau_3 = 0$, it indicates the absence of any entanglement which means that the state is fully separable. Thus, the lower bound $\tau_3 = 0$ can serve as a criterion for detecting and recognizing multipartite entanglement.

### 4.5.3 Results and discussion

In this section, we investigate the behavior of the quantum Otto heat engine, for our system where the energy related to the external electric field $\vec{E}$ changes between $\hbar\Omega_C$ and $\hbar\Omega_H$ ($\hbar\Omega_H > \hbar\Omega_C$) in the adiabatic processes. Furthermore, we study the effect of the excitons frequency in each quantum dot $\hbar\omega$ and the Forster interaction $\lambda$ on the amount of work performed by the engine. Moreover, we study the relation between the work performed and quantum entanglement between the quantum dot's qubits

#### Work and heat exchange

The behaviors of the work performed, the heat liberated $Q_C$, and the heat absorbed $Q_H$ by the engine against the Forster interaction energy $\lambda$ depicted in Figure 4.6a. In figure 4.6b we show the effect of the temperature of the hot bath and the energy related to the external electric field $\hbar\Omega_H$ on the work performed by the engine. We note for this model that the energy parameters $\hbar\Omega$, $\hbar\omega$, and $\hbar J_z$ are assumed to be in the order of $meV$ which is coherent with experimental observations [217, 218].

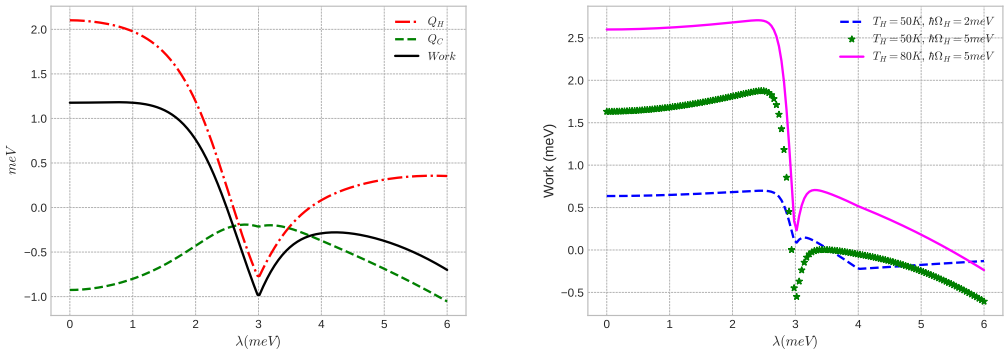


(A) (B)

FIGURE 4.6: A: The work performed, heat liberated $Q_C$ and heat absorbed $Q_H$, with $\hbar\omega_i = 2meV$, $J_z = 2.5meV$, $T_C = 1K$, $T_H = 40K$, $\hbar\Omega_H = 5meV$, and $\hbar\Omega_C = 1meV$. B: The work performed for $\hbar\omega_i = 2meV$, $J_z = 2.5meV$, $T_C = 1K$, and $\hbar\Omega_C = 1meV$.

Figure 4.6a clearly shows distinct regions of the working substance with respect to the Forster interaction energy $\lambda$. In the first region, characterized by smaller values of $\lambda$, positive work is absorbed, indicating that the system functions as a heat engine, this engine absorbs heat from the hot bath ($Q_H > 0$) and transfers it to the cold bath ($Q_C < 0$) while producing useful work. We note that the work is decreased slowly with increasing of the Forster interaction $\lambda$ until a critical value of this parameter after which, the engine requires a negative work ($W < 0$) to extract heat from the hot reservoir to the cold reservoir, i.e. the machine works as a heater and the engine cannot produce work. We observe also for a strong Forster interaction, that the heat absorbed $Q_H$ by the engine becomes again positive, but the work and the heat liberated from the engine are still negative. This means that the engine works as

a thermal accelerator where the engine transfers heat from the hot reservoir to the cold one, without producing work. These results show that we can switch from one regime to the other by simply increasing a single parameter, the Forster interaction $\lambda$. Figure 4.6*b* shows that the temperature of the hot bath $T_H$ doesn't affect the general behavior (shape) of the work performed but affects only the amount of this work. This amount increases with increasing temperature of the hot bath because the heat absorbed from the hot bath increases. Moreover, the amount of work increases with the excitonic dipoles moments energy $\hbar\Omega$. This is due to the larger difference between $\hbar\Omega_H$ and $\hbar\Omega_C$ under the quantum adiabatic process, which makes the engine convert a lot of energy to work. In order to investigate the effect of the frequency of the excitons in each quantum dot on the work performed by the engine, we present the behaviors of the work performed in figures 4.7a and 4.7b.

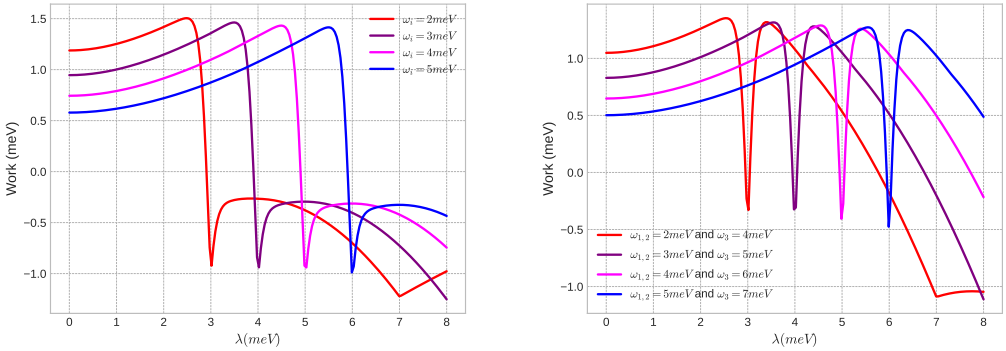


(A) (B)

FIGURE 4.7: (A): Variation of Work with $\lambda$ for equal values of $\hbar\omega_i$; $\omega_1 = \omega_2 = \omega_2 = \omega_3 = \omega_i$. (B): Variation of Work with $\lambda$ for different values of $\hbar\omega_i$.

Figure 4.7a illustrates the behavior of the work done for different values of the exciton frequency $(\hbar\omega_i)$ as a function of the Foster interaction. In this situation, where the $w_i$'s are equal, we observe, for lower Foster interaction energies, that the work is positive, indicating that the machine operates as a heat engine. However, for stronger Foster interactions, the work becomes negative, rendering the engine incapable of producing any work. Additionally, the critical value of $\lambda$ at which the work turns negative varies with the exciton energy $(\hbar\omega_i)$. This suggests that the work is more resilient against the Foster energy for higher exciton energy values, and its behavior remains consistent. Moreover, the amount of the work decreases as $\hbar\omega_i$ increases for smaller values of $\lambda$. Moving on to Figure 4.7b, we observe a similar pattern to Figure 4.7a. However, in this case, the $\omega_i$ values differ among the three quantum dots. Either two values are the same while the third one is different, or all three values are distinct. Before reaching the critical values of $\lambda$, the work exhibits similar behavior as before. However, as $\lambda$ increases, the work performed undergoes death and revival, indicating that the engine fails to produce work at certain critical values of $\lambda$. After these critical values, the engine can produce work and can be considered as a heat engine. Now, the question arises as to why the work done transitions from positive to negative values and why the work exhibits revival when the system lacks symmetry.

### Work and entanglement

To understand the reason behind the decrease and subsequent revival of the work at a critical value of $\lambda$ observed in figures 4.6 and 4.7, we analyze its behavior in comparison to the behavior of several entanglements shared between the quantum dots of the system with different values of the exciton frequency in each quantum dot. We can gain insights into the underlying mechanisms driving this phenomenon by examining the relationship between these two aspects. The decrease and revival of the work refer to a pattern where the work initially declines, then undergoes a resurgence at a specific value of $\lambda$. This behavior can be attributed to the interplay between $\lambda$ and the system's entanglement. By comparing the behavior of the work with the behavior of entanglement, we can observe a correlation between their patterns. The decrease in work is often accompanied by an increase in entanglement, indicating a connection between these phenomena

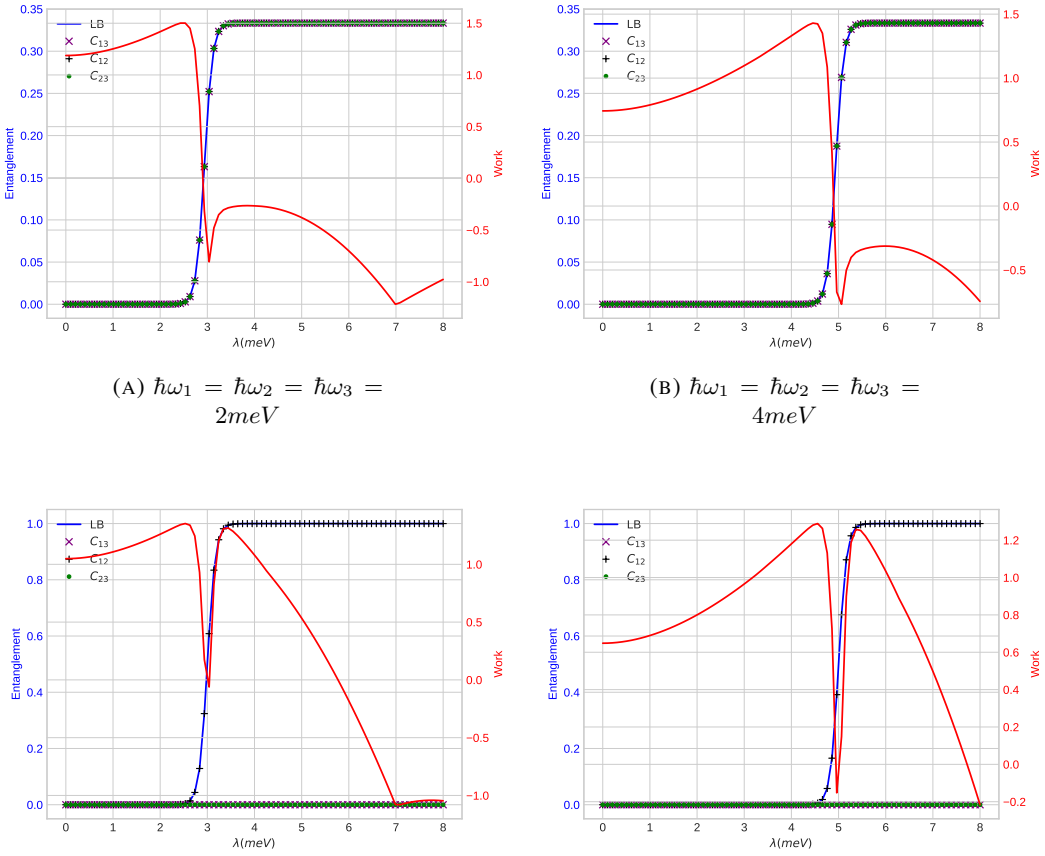


(A) $\hbar\omega_1 = \hbar\omega_2 = \hbar\omega_3 = 2meV$

(B) $\hbar\omega_1 = \hbar\omega_2 = \hbar\omega_3 = 4meV$

(C) $\hbar\omega_{1,2} = 2meV$ and $\hbar\omega_3 = 4meV$

(D) $\hbar\omega_{1,2} = 4meV$ and $\hbar\omega_3 = 6meV$

FIGURE 4.8: Entanglement and Work versus the Förster interaction $\lambda$ for different values of the exciton frequencies $\hbar\omega_i$.

It is well known that the entanglement between two quantum systems depends on the strength of the interaction between them. In our case, this interaction can be characterized by a Förster (or dipole-dipole) interaction $\lambda$, which describes the energy transfer between two quantum dots due to their mutual electric dipole moments. The stronger the Förster interaction is the stronger the entanglement between the two quantum dots will be. Indeed, the Förster interaction can lead to the exchange of energy and information between the dots,

which can facilitate the establishment of entanglement. However, it is important to note that the presence of the Förster interaction alone does not guarantee the presence of entanglement. Other factors, such as the initial state of the quantum systems and the presence of external noise or decoherence, can also influence the strength of entanglement. Furthermore, in addition to the influence of the exciton frequency in each quantum dot on the critical value of $\lambda$ observed in Figure 4.7, this frequency plays a significant role in entanglement distribution. The monogamous properties of entanglement dictate that the entanglement between two quantum dots is mutually exclusive. As one quantum dot becomes more entangled with another, its entanglement with other quantum dots diminishes. This monogamous nature of entanglement implies that the frequency of each quantum dot can profoundly impact how entanglement is distributed among the quantum dots in the system.

Figure 4.8 shows that entanglement is absent for small values of $\lambda$ and appears at some critical value $\lambda_c$, which depends on the exciton frequency in each quantum dot; $\lambda_c$ becoming larger for larger values of $\hbar\omega$. For example in Figures 4.8a and 4.8b, we have $\lambda_c = 3meV$ and $\lambda_c = 6meV$ for $\hbar\omega_i = 2meV$ and $\hbar\omega_i = 4meV$ respectively. After $\lambda_c$ we observe that the entanglement increases and reaches its maximum $\frac{1}{3}$. This indicates that the entanglement is evenly distributed among the three quantum dots and is achieved by assigning the same frequency value to each of them. However in Figures 4.8c and 4.8d (when $\hbar\omega_1 = \hbar\omega_2 \neq \hbar\omega_3$), we observe that only the two quantum dots with identical frequencies exhibit entanglement, reaching its maximum value 1 when lambda is larger. This means that these two quantum dots are maximally entangled, while the other pairs remain separated for all values of $\lambda$. Another observation can be drawn is that the critical value of $\lambda$ depends on the frequency of the entangled pairs, and does not depend on the frequency of the other subsystems.
Note that at the critical value of $\lambda$, entanglement appears, and the work performed by the engine disappears. However, work exhibits revival when the system lacks symmetry, and entanglement is shared only between two quantum dots. This implies that the revival of work performed after the decline is due to the third quantum dot.
Moreover, we can observe that the entanglement at the end of the cycle is detrimental to the work, and the work cannot be obtained if the entanglement is large enough. Our engine cannot produce work if it becomes entangled at the end of its contact with the cold bath. We can conclude that the influence of entanglement on the work performed by a quantum heat engine can be significant, as entanglement can affect the way that energy is distributed within the system. In a quantum heat engine, entanglement can lead to correlations between the energy levels of the system, which can, in turn, affect the efficiency of the engine. For example, if the system is in a highly entangled state, it may be more difficult to extract work from the system, as the energy levels may be more closely correlated and thus more difficult to manipulate. However, if the system is in a less entangled state, it may be easier to extract work from the system, as the energy levels may be less correlated and thus more easily manipulated. Physically, the increase of the excitonic dipoles moments energy $\hbar\Omega$ is due to the increase of the electric field $\vec{E}$, which makes all dipoles parallel, leading to an increase in the repulsive interaction between dipoles, due to the decrease of entanglement between the double quantum dots at the end of the cycle and the increase of the work performed. Based on the description provided, we can conclude that the system consumes energy in order to create entanglement and then recovers a small quantity after the entanglement is established. This phenomenon can be compared to starting a car, where a relatively significant amount of energy is required to initiate the engine. In this process, various components of the car's system, including the ignition system and fuel pump, are activated. However, certain non-essential functions are temporarily disabled to conserve and concentrate the available energy specifically for starting

the engine. This strategic approach ensures that the system can channel its resources effectively and concentrate its energy on the primary objective of entanglement creation; this can lead to an entanglement cost, approach study, based on these types of heat engines.

### 4.5.4 Conclusion

This paper delved into the intricate world of quantum heat engines, focusing on the quantum Otto cycle with the working substance consisting of three InAs quantum dots. These engines can operate at extremely small scales, offering promising prospects for efficient energy conversion. We have studied their behavior under the influence of external electric field and Forster interaction parameters, shedding light on the fascinating interplay between these parameters and the engine's performance. We find that the work performed by the quantum heat engine is strongly influenced by the Forster interaction energy ($\lambda$) and the temperature of the baths. We have identified distinct regions of operation based on the Forster energy, ranging from a heat engine that absorbs heat and produces work to a thermal accelerator that transfers heat without producing work. Temperature variations in the hot bath directly impact the amount of work extracted, with higher temperatures leading to increased work production. Additionally, the energy of excitonic dipoles ($\hbar\Omega$) plays a significant role, with larger differences between $\hbar\Omega_H$ and $\hbar\Omega_C$ yielding more work.
The study also explored the connection between the work performed by the engine and quantum entanglement among the quantum dots. As the Forster interaction increased, work initially decreased and then revived at critical values of $\lambda$. This pattern is closely correlated with changes in quantum entanglement. Higher entanglement was associated with decreased work, emphasizing the significance of entanglement in influencing engine performance. Then, the work highlighted that the presence of the Förster interaction contributes to entanglement between quantum dots, which can affect the energy distribution and the efficiency of the engine. The entanglement properties are intricately related to the exciton frequency in each quantum dot, with certain frequency configurations favoring maximal entanglement. Importantly, the presence of entanglement at the end of the cycle can inhibit work production, demonstrating the substantial impact of entanglement on quantum heat engine behavior. Finally, The study suggests that the system incurs an energy cost to establish entanglement. Resources are strategically allocated to initiate the entanglement process, with non-essential functions temporarily disabled. This approach ensures efficient energy utilization, leading to the establishment of entanglement.

In summary, this research unveils the intricate relationship between the Forster interaction, entanglement, and the performance of quantum heat engines. The findings underscore the potential of quantum heat engines as a viable energy conversion technology, while also highlighting the importance of managing entanglement in optimizing their efficiency. Further exploration of these phenomena could pave the way for the development of highly efficient quantum heat engines, contributing to the ever-evolving landscape of energy technology.

# Conclusion and Perspectives

The field of quantum dots had a rapid evolution, transitioning from the theoretical world to the practical applications, culminating in the award of the Nobel Prize in chemistry in 2023. This precious award came as a result not only of scientific progress but also of the crucial role that quantum dots play in various technologies. These nano-materials present unique properties, among them, their discrete energy levels and size-tunable optical and electronic properties, indicating a future where their integration into diverse technologies is not just predicted but unavoidable. These are labeled as artificial atoms because of their unique properties and behavior, which closely resemble those of individual atoms, where the carriers' motion is quantized in all the spatial directions. The ability to manipulate their size allows for precise self-emission to exhibit precise and diverse colors across a wide range of light intensities, making them ideal for next-generation large-scale displays. This utility of quantum dots is the key foundation for building new-age technologies in several areas.

In the field of photovoltaics, quantum dot solar cells take advantage of the tunable gap to improve the efficiency of photovoltaic devices. This is because of their unique light absorption and conversion capabilities, as well as their adjustable bandgaps across a wide range of energy levels by changing their size. As we transition to a more visually dominated world, the application of quantum dots in display technologies leads to the development of QD-enhanced liquid crystal displays (LCDs), enhancing color purity and energy efficiency. Their size-dependent emission spectra enable displays to boast a more dynamic color range and sharper resolution, all while optimizing energy consumption. Lastly, the impact of quantum dots extends also into the realm of quantum computing, where they are expected to play a crucial role in developing quantum bits (Qubits). The coherence and control over quantum states that quantum dots offer promise to overcome some of the most challenging obstacles in quantum computation, potentially leading to development in processing power and cryptographic security that are currently beyond our reach. The acknowledgment by the Nobel Committee sheds light on a pivotal turning point in our research and technologies, where the word of quantum mechanics meets the word of technological innovation. The quantum dots are expected to serve as a pivot for this transformation, marking the beginning of an era where quantum phenomena are not only studied but harnessed in different technologies.

Throughout this thesis, we have pushed the boundaries of our knowledge, delving deeper into the quantum correlations in two double quantum dots AlGaAs/GaAs. Our aim was to understand the behaviors of these correlations against the influence of temperature and electromagnetic fields. We have investigated the impact of the energy offset of each double quantum dot and the tunneling coupling energy on these correlations. Our results indicate that the variations in entanglement of formation, standard discord, and global quantum discord are significantly influenced by the energy offset and tunneling coupling energy. Our findings offer valuable insights into the interaction between quantum correlations and environmental parameters, with significant implications for the advancement of quantum technologies.

In our investigation into the robustness of quantum correlations, particularly quantum entanglement, and quantum discord, against environmental noise, in the array of two optically driven coupled semiconductor quantum dots independently interacting with dephasing reservoirs. We find that the quantum correlations exhibit an increase with the rise of Förster interaction, diminishing when the electric field is activated. Additionally, we observed that this increase attains its maximum at extremely low temperatures and dimensionless time periods, followed by a decrease and decay as these parameters increase. This behavior is attributed to the influences of thermal relaxation effects and environmental factors. However, our observations reveal that, even as entanglement disappears for elevated values of temperature and dimensionless time, quantum discord survives. This robustness shows the capacity of discord to quantify quantum correlations beyond entanglement. Through our investigation, we have deduced that, despite the influences of electric field effects and Förster interaction effects, the non-Markovian behavior of quantum correlations remains intact under these two influences.

Our exploration of the Wigner function's role in this context has brought new understanding to its application in signaling entanglement within quantum dot systems. The existence of negative regions in the Wigner distribution serves as a reliable indicator of quantum entanglement and has extensive implications for quantum computation and cryptography. This function's sensitivity to the quantum state of a system allows for a deeper insight into the quantum mechanical phenomena at play within quantum dots, solidifying their position as a critical element in the quantum computing toolkit.

Moreover, we have investigated the field of quantum thermodynamics, showcasing how quantum dots could be utilized in cutting-edge quantum heat engines. The relationship between entanglement and the work performed by the heat engine provides a fascinating intersection between quantum mechanics and thermodynamics, which may revolutionize how we approach energy conversion at the nanoscale.

In summary, this thesis presents the different behaviors of quantum dots. By extending our knowledge of how quantum correlations within quantum dots can be harnessed and controlled. this work has opened a window onto the landscape of quantum technology where quantum dots stand as an instrument of innovation.

As we look ahead, the application of quantum dots spans various fields due to their unique optical and electronic characteristics. Particularly the application of these nanomaterials in quantum batteries. The promise of quantum dots in this application lies in their ability to facilitate ultra-fast charging processes due to their quantum properties, potentially revolutionizing energy storage technologies. My future research aims to delve into the practicalities of integrating quantum dots into quantum battery systems, exploring their efficiency and stability to pave the way for a new generation of energy solutions.

Another exciting direction is the investigation of quantum correlations in multipartite systems, which are systems consisting of more than two interacting quantum entities. Quantum dots provide a unique platform for studying these complex systems due to their highly controllable interaction parameters. By measuring and manipulating the quantum correlations in such systems, we can uncover new aspects of quantum entanglement and coherence. This knowledge is not merely academic; it is essential for the realization of sophisticated quantum networks and advanced computational algorithms.

Furthermore, the application of quantum dots extends to the development of quantum heat engines, which may operate under alternative thermodynamic cycles. My goal is to explore these quantum systems in different thermodynamic cycles beyond the conventional ones, like Carnot or other types, to identify more efficient ways to convert quantum heat into work. This could lead to the development of new thermal machines that operate at the boundaries of quantum and classical physics, potentially transforming our approach to energy consumption and recovery in microscopic regimes.

Each of these perspectives represents a substantial contribution to the future of quantum technologies. In aligning my research with these ambitious goals, I want to push the boundaries of what is possible with quantum dots. The journey is as thrilling as the destination is promising, and as we harness the full potential of quantum dots, we stand on the precipice of a new era in quantum science and technology.

# Bibliography


[1] KM Cha, K Shibata, and K Hirakawa. Single electron transport through site-controlled inas quantum dots. *Applied Physics Letters*, 101(22), 2012.

[2] Ronald Hanson and David D Awschalom. Coherent manipulation of single spins in semiconductors. *Nature*, 453(7198):1043–1049, 2008.

[3] Lianhe Li, Gilles Patriarche, Nicolas Chauvin, Philipp Ridha, Marco Rossetti, Janusz Andrzejewski, Grzegorz Sek, Jan Misiewicz, and Andrea Fiore. Controlling the aspect ratio of quantum dots: From columnar dots to quantum rods. *IEEE Journal of Selected Topics in Quantum Electronics*, 14(4):1204–1213, 2008.

[4] Dmitri V Talapin, Jong-Soo Lee, Maksym V Kovalenko, and Elena V Shevchenko. Prospects of colloidal nanocrystals for electronic and optoelectronic applications. *Chemical reviews*, 110(1):389–458, 2010.

[5] Justin C Norman, Daehwan Jung, Yating Wan, and John E Bowers. Perspective: The future of quantum dot photonic integrated circuits. *APL photonics*, 3(3), 2018.

[6] David J Barber and Rodney Loudon. *An introduction to the properties of condensed matter*. CUP Archive, 1989.

[7] Gert R Strobl. *Condensed matter physics: crystals, liquids, liquid crystals, and polymers*. Springer Science & Business Media, 2012.

[8] Michael De Podesta. *Understanding the properties of matter*. CRC Press, 2020.

[9] Franz Schwabl. *Quantum mechanics*. Springer Science & Business Media, 2007.

[10] Felix Bloch. Quantum mechanics of electrons in crystal lattices. *Z. Phys*, 52:555–600, 1928.

[11] William Shockley. The theory of p-n junctions in semiconductors and p-n junction transistors. *Bell system technical journal*, 28(3):435–489, 1949.

[12] John Bardeen and Walter Hauser Brattain. The transistor, a semi-conductor triode. *Physical Review*, 74(2):230, 1948.

[13] Andrea Frova and Paul Handler. Franz-keldysh effect in the space-charge region of a germanium p- n junction. *Physical Review*, 137(6A):A1857, 1965.

[14] JP Auton. Infrared transmission polarizers by photolithography. *Applied optics*, 6(6):1023–1027, 1967.

[15] Gordon Moore. Moore's law. *Electronics Magazine*, 38(8):114, 1965.

[16] Paul Harrison and Alex Valavanis. *Quantum wells, wires and dots: theoretical and computational physics of semiconductor nanostructures*. John Wiley & Sons, 2016.

[17] AA Ekimov AI, Onushchenko. Quantum size effect in three-dimensional microcrystals of semiconductors. *Letters to the Journal of Experimental and Theoretical Physics*, 34(6):363–366, 1981.

[18] Louis E Brus. Electron–electron and electron-hole interactions in small semiconductor crystallites: The size dependence of the lowest excited electronic state. *The Journal of chemical physics*, 80(9):4403–4409, 1984.

[19] Moungi G Bawendi, Michael L Steigerwald, and Louis E Brus. The quantum mechanics of larger semiconductor clusters (" quantum dots"). *Annual Review of Physical Chemistry*, 41(1):477–496, 1990.

[20] Jesse R Manders, Lei Qian, Alexandre Titov, Jake Hyvonen, Jean Tokarz-Scott, Jiangeng Xue, and Paul H Holloway. 8.3: Distinguished paper: Next-generation display technology: Quantum-dot leds. In *SID Symposium Digest of Technical Papers*, pages 73–75. Wiley Online Library, 2015.

[21] LeeAnn Kim, Polina O Anikeeva, Seth A Coe-Sullivan, Jonathan S Steckel, Moungi G Bawendi, and Vladimir Bulovic. Contact printing of quantum dot light-emitting devices. *Nano letters*, 8(12):4513–4517, 2008.

[22] David Deutsch. Quantum theory, the church–turing principle and the universal quantum computer. *Proceedings of the Royal Society of London. A. Mathematical and Physical Sciences*, 400(1818):97–117, 1985.

[23] Michael A Nielsen and Isaac Chuang. Quantum computation and quantum information, 2002.

[24] Albert Einstein and Francis A Davis. *The principle of relativity*. Courier Corporation, 2013.

[25] A. Einstein, B. Podolsky, and N. Rosen. Can quantum-mechanical description of physical reality be considered complete? *Phys. Rev.*, 47:777–780, May 1935.

[26] Wojciech Hubert Zurek. Decoherence, einselection, and the quantum origins of the classical. *Reviews of modern physics*, 75(3):715, 2003.

[27] Alain Aspect, Jean Dalibard, and Gérard Roger. Experimental test of bell's inequalities using time-varying analyzers. *Physical review letters*, 49(25):1804, 1982.

[28] Hicham Ait Mansour, Mustapha Faqir, and Morad El Baz. Global quantum discord and entanglement in two coupled double quantum dots algaas/gaas. *International Journal of Theoretical Physics*, 62(3):58, 2023.

[29] H Ait Mansour, FZ Siyouri, M Faqir, and M El Baz. Quantum correlations dynamics in two coupled semiconductor inas quantum dots. *Physica Scripta*, 95(9):095101, 2020.

[30] H Ait Mansour and FZ Siyouri. Wigner function as a detector of entanglement in open two coupled inas semiconductor quantum dots. *International Journal of Theoretical Physics*, 61(4):118, 2022.

[31] Fatima-Zahra Siyouri and Hicham Ait Mansour. Robustness of wigner function negativity under the exciton-exciton interaction effects inside two coupled semiconductor quantum dots. *Quantum Information Processing*, 20:1–10, 2021.

[32] H Ait Mansour, F El Ayachi, M Faqir, and M Elbaz. Inas three quantum dots as working substance for quantum heat engine. *arXiv preprint arXiv:2309.10958*, 2023.

[33] Andrew Mills and Stephen Le Hunte. An overview of semiconductor photocatalysis. *Journal of photochemistry and photobiology A: Chemistry*, 108(1):1–35, 1997.

[34] Frederik Hetsch, Ni Zhao, Stephen V Kershaw, and Andrey L Rogach. Quantum dot field effect transistors. *Materials Today*, 16(9):312–325, 2013.

[35] Yanchao Zhang, Zhimin Yang, Xin Zhang, Bihong Lin, Guoxing Lin, and Jincan Chen. Coulomb-coupled quantum-dot thermal transistors. *Europhysics Letters*, 122(1):17002, 2018.

[36] Hung-Chia Wang, Zhen Bao, Hsin-Yu Tsai, An-Cih Tang, and Ru-Shi Liu. Perovskite quantum dots and their application in light-emitting diodes. *Small*, 14(1):1702433, 2018.

[37] Hyungsuk Moon, Changmin Lee, Woosuk Lee, Jungwoo Kim, and Heeyeop Chae. Stability of quantum dots, quantum dot films, and quantum dot light-emitting diodes for display applications. *Advanced Materials*, 31(34):1804294, 2019.

[38] Tae-Ho Kim, Dae-Young Chung, JiYeon Ku, Inyong Song, Soohwan Sul, Dae-Hyeong Kim, Kyung-Sang Cho, Byoung Lyong Choi, Jong Min Kim, Sungwoo Hwang, et al. Heterogeneous stacking of nanodot monolayers by dry pick-and-place transfer and its applications in quantum dot light-emitting diodes. *nature communications*, 4(1):2637, 2013.

[39] Chi-Hsiu Chang and Yuh-Lang Lee. Chemical bath deposition of cds quantum dots onto mesoscopic ti o 2 films for application in quantum-dot-sensitized solar cells. *Applied Physics Letters*, 91(5):053503, 2007.

[40] Quanxin Zhang, Yiduo Zhang, Shuqing Huang, Xiaoming Huang, Yanhong Luo, Qingbo Meng, and Dongmei Li. Application of carbon counterelectrode on cds quantum dot-sensitized solar cells (qdsscs). *Electrochemistry Communications*, 12(2):327–330, 2010.

[41] Ningxiao Gao, Libing Huang, Tianya Li, Jinghui Song, Hengwei Hu, Yong Liu, and Seeram Ramakrishna. Application of carbon dots in dye-sensitized solar cells: a review. *Journal of Applied Polymer Science*, 137(10):48443, 2020.

[42] Katherine Bourzac et al. Quantum dots go on display. *Nature*, 493(7432):283, 2013.

[43] Seth Coe-Sullivan, Wenhao Liu, Peter Allen, and Jonathan S Steckel. Quantum dots for led downconversion in display applications. *ECS Journal of Solid State Science and Technology*, 2(2):R3026, 2012.

[44] E Jang. Environmentally friendly quantum dots for display applications. In *2018 IEEE International Electron Devices Meeting (IEDM)*, pages 38–2. IEEE, 2018.

[45] Debasis Bera, Lei Qian, Teng-Kuan Tseng, and Paul H Holloway. Quantum dots and their multimodal applications: a review. *Materials*, 3(4):2260–2345, 2010.

[46] John W Leech. *Classical mechanics:(Methuen's monographs on physical subjects)*. Springer, 1970.

[47] Robert M Eisberg. Fundamentals of modern physics. *American Journal of Physics*, 30(12):937–938, 1962.

[48] Michael J Kelly. *Low-dimensional semiconductors: materials, physics, technology, devices*, volume 3. Clarendon Press, 1995.

[49] L.I.Schiff. *Quantum Mechanics*. McGraw-Hill, NewYork, 1968.

[50] S Shanmugam. *Nanotechnology*. MJP Publisher, 2019.

[51] Arvind Kumar, Steven E Laux, and Frank Stern. Electron states in a gaas quantum dot in a magnetic field. *Physical Review B*, 42(8):5166, 1990.

[52] PM Petroff and SP DenBaars. Mbe and mocvd growth and properties of self-assembling quantum dot arrays in iii-v semiconductor structures. *Superlattices and microstructures*, 15(1):15, 1994.

[53] Dieter Bimberg, Marius Grundmann, and Nikolai N Ledentsov. *Quantum dot heterostructures*. John Wiley & Sons, 1999.

[54] Al Y Cho and JR Arthur. Molecular beam epitaxy. *Progress in solid state chemistry*, 10:157–191, 1975.

[55] Kyu Man Cha, Isao Horiuchi, Kenji Shibata, and Kazuhiko Hirakawa. Size-limiting effect of site-controlled inas quantum dots grown at high temperatures by molecular beam epitaxy. *Applied physics express*, 5(8):085501, 2012.

[56] A Paul Alivisatos. Semiconductor clusters, nanocrystals, and quantum dots. *science*, 271(5251):933–937, 1996.

[57] Edson Roberto Leite and Caue Ribeiro. *Crystallization and growth of colloidal nanocrystals*. Springer Science & Business Media, 2011.

[58] Stephanie M Reimann and Matti Manninen. Electronic structure of quantum dots. *Reviews of modern physics*, 74(4):1283, 2002.

[59] Wilfred G Van der Wiel, Silvano De Franceschi, Jeroen M Elzerman, Toshimasa Fujisawa, Seigo Tarucha, and Leo P Kouwenhoven. Electron transport through double quantum dots. *Reviews of modern physics*, 75(1):1, 2002.

[60] Daniel Loss and David P DiVincenzo. Quantum computation with quantum dots. *Physical Review A*, 57(1):120, 1998.

[61] Frank HL Koppens, Christo Buizert, Klaas-Jan Tielrooij, Ivo T Vink, Katja C Nowack, Tristan Meunier, LP Kouwenhoven, and LMK Vandersypen. Driven coherent oscillations of a single electron spin in a quantum dot. *Nature*, 442(7104):766–771, 2006.

[62] Jason R Petta, Alexander Comstock Johnson, Jacob M Taylor, Edward A Laird, Amir Yacoby, Mikhail D Lukin, Charles M Marcus, Micah P Hanson, and Arthur C Gossard. Coherent manipulation of coupled electron spins in semiconductor quantum dots. *Science*, 309(5744):2180–2184, 2005.

[63] Sv Fafard, ZR Wasilewski, C Ni Allen, D Picard, M Spanner, JP McCaffrey, and PG Piva. Manipulating the energy levels of semiconductor quantum dots. *Physical Review B*, 59(23):15368, 1999.

[64] S Fafard and C Nı Allen. Intermixing in quantum-dot ensembles with sharp adjustable shells. *Applied physics letters*, 75(16):2374–2376, 1999.

[65] EA Zibik, WH Ng, LR Wilson, MS Skolnick, JW Cockburn, M Gutierrez, MJ Steer, and M Hopkinson. Effects of alloy intermixing on the lateral confinement potential in inas/ gaas self-assembled quantum dots probed by intersublevel absorption spectroscopy. *Applied physics letters*, 90(16), 2007.

[66] Julian Stangl, Vàclav Holỳ, and Guenther Bauer. Structural properties of self-organized semiconductor nanostructures. *Reviews of modern physics*, 76(3):725, 2004.

[67] Jun He, Hubert J Krenner, C Pryor, JP Zhang, Y Wu, DG Allen, CM Morris, MS Sherwin, and Pierre M Petroff. Growth, structural, and optical properties of self-assembled (in, ga) as quantum posts on gaas. *Nano letters*, 7(3):802–806, 2007.

[68] M Motyka, G Sęk, K Ryczko, J Andrzejewski, J Misiewicz, LH Li, A Fiore, and G Patriarche. Optical and electronic properties of gaas-based structures with columnar quantum dots. *Applied physics letters*, 90(18), 2007.

[69] LH Li, G Patriarche, EH Linfield, SP Khanna, and AG Davies. Effects of using as2 and as4 on the optical properties of ingaas quantum rods grown by molecular beam epitaxy. *Journal of Applied Physics*, 108(10), 2010.

[70] R Nedzinskas, B Čechavičius, V Karpus, J Kavaliauskas, G Valušis, LH Li, SP Khanna, and EH Linfield. Photoreflectance and photoluminescence studies of epitaxial ingaas quantum rods grown with as2 and as4 sources. *Journal of Applied Physics*, 109(12), 2011.

[71] Axel Lorke Johannes Luyken, Jorge M Garcia, and Pierre M Petroff. Growth and electronic properties of self-organized quantum rings. *Japanese Journal of Applied Physics*, 40(3S):1857, 2001.

[72] Daniel Granados and Jorge M Garcia. In (ga) as self-assembled quantum ring formation by molecular beam epitaxy. *Applied physics letters*, 82(15):2401–2403, 2003.

[73] S Bhowmick, G Huang, W Guo, CS Lee, P Bhattacharya, G Ariyawansa, and AGU Perera. High-performance quantum ring detector for the 1–3 terahertz range. *Applied Physics Letters*, 96(23), 2010.

[74] JM Garcia, T Mankad, PO Holtz, PJ Wellman, and PM Petroff. Electronic states tuning of inas self-assembled quantum dots. *Applied Physics Letters*, 72(24):3172–3174, 1998.

[75] Xiaogang Peng, Michael C Schlamp, Andreas V Kadavanich, and A Paul Alivisatos. Epitaxial growth of highly luminescent cdse/cds core/shell nanocrystals with photostability and electronic accessibility. *Journal of the American Chemical Society*, 119(30):7019–7029, 1997.

[76] CB Murray, CR Kagan, and MG Bawendi. Self-organization of cdse nanocrystallites into three-dimensional quantum dot superlattices. *Science*, 270(5240):1335–1338, 1995.

[77] Aarnoud L Roest, John J Kelly, and Daniel Vanmaekelbergh. Coulomb blockade of electron transport in a zno quantum-dot solid. *Applied physics letters*, 83(26):5530–5532, 2003.

[78] Philippe Guyot-Sionnest. Electrical transport in colloidal quantum dot films. *The Journal of Physical Chemistry Letters*, 3(9):1169–1175, 2012.

[79] John von Neumann. Mathematische grundlagen der quantenmechanik (berlin: Julius springer). *English translation (revised by the author): Mathematical Foundations of Quantum Mechanics*, 1955.

[80] Matteo GA Paris. The modern tools of quantum mechanics: a tutorial on quantum states, measurements, and operations. *The European Physical Journal Special Topics*, 203(1):61–86, 2012.

[81] E. Wigner. On the quantum correction for thermodynamic equilibrium. *Phys. Rev.*, 40:749–759, Jun 1932.

[82] Benjamin Schumacher. Quantum coding. *Physical Review A*, 51(4):2738, 1995.

[83] Claude Elwood Shannon. A mathematical theory of communication. *The Bell system technical journal*, 27(3):379–423, 1948.

[84] Thaddeus D Ladd, Fedor Jelezko, Raymond Laflamme, Yasunobu Nakamura, Christopher Monroe, and Jeremy Lloyd O'Brien. Quantum computers. *nature*, 464(7285):45–53, 2010.

[85] Gerardo Adesso, Thomas R Bromley, and Marco Cianciaruso. Measures and applications of quantum correlations. *Journal of Physics A: Mathematical and Theoretical*, 49(47):473001, 2016.

[86] Zhong-Xiao Man, Yun-Jie Xia, and Rosario Lo Franco. Cavity-based architecture to preserve quantum coherence and entanglement. *Scientific reports*, 5(1):13843, 2015.

[87] Irénée Frérot, Matteo Fadel, and Maciej Lewenstein. Probing quantum correlations in many-body systems: a review of scalable methods. *arXiv preprint arXiv:2302.00640*, 2023.

[88] Zhen-Peng Xu, Satoya Imai, and Otfried Gühne. Fate of multiparticle entanglement when one particle becomes classical. *Physical Review A*, 107(4):L040401, 2023.

[89] Leah Henderson and Vlatko Vedral. Classical, quantum and total correlations. *Journal of physics A: mathematical and general*, 34(35):6899, 2001.

[90] Albert Einstein, Boris Podolsky, and Nathan Rosen. Can quantum-mechanical description of physical reality be considered complete? *Physical review*, 47(10):777, 1935.

[91] Erwin Schrödinger. Die gegenwärtige situation in der quantenmechanik. *Naturwissenschaften*, 23(50):844–849, 1935.

[92] Rosario Lo Franco and Giuseppe Compagno. Quantum entanglement of identical particles by standard information-theoretic notions. *Scientific reports*, 6(1):1–10, 2016.

[93] Ryszard Horodecki, Paweł Horodecki, Michał Horodecki, and Karol Horodecki. Quantum entanglement. *Reviews of modern physics*, 81(2):865, 2009.

[94] Luigi Amico, Rosario Fazio, Andreas Osterloh, and Vlatko Vedral. Entanglement in many-body systems. *Reviews of modern physics*, 80(2):517, 2008.

[95] Leandro Aolita, Fernando De Melo, and Luiz Davidovich. Open-system dynamics of entanglement: a key issues review. *Reports on Progress in Physics*, 78(4):042001, 2015.

[96] Harold Ollivier and Wojciech H Zurek. Quantum discord: a measure of the quantumness of correlations. *Physical review letters*, 88(1):017901, 2001.

[97] Wojciech Hubert Zurek. Decoherence, einselection, and the quantum origins of the classical. *Reviews of modern physics*, 75(3):715, 2003.

[98] William K Wootters. Entanglement of formation of an arbitrary state of two qubits. *Physical Review Letters*, 80(10):2245, 1998.

[99] William K Wootters. Entanglement of formation and concurrence. *Quantum Inf. Comput.*, 1(1):27–44, 2001.

[100] Armin Uhlmann. Fidelity and concurrence of conjugated states. *Physical Review A*, 62(3):032307, 2000.

[101] Ting Yu and JH Eberly. Sudden death of entanglement. *Science*, 323(5914):598–601, 2009.

[102] Charles H Bennett, Herbert J Bernstein, Sandu Popescu, and Benjamin Schumacher. Concentrating partial entanglement by local operations. *Physical Review A*, 53(4):2046, 1996.

[103] Sandu Popescu and Daniel Rohrlich. Thermodynamics and the measure of entanglement. *Physical Review A*, 56(5):R3319, 1997.

[104] Karol Życzkowski, Paweł Horodecki, Anna Sanpera, and Maciej Lewenstein. Volume of the set of separable states. *Physical Review A*, 58(2):883, 1998.

[105] Guifré Vidal and Reinhard F Werner. Computable measure of entanglement. *Physical Review A*, 65(3):032314, 2002.

[106] Carlos Sabín and Guillermo García-Alcaine. A classification of entanglement in three-qubit systems. *The european physical journal D*, 48:435–442, 2008.

[107] Jiang-Tao Cai and Ahmad Abliz. Tripartite correlations in a heisenberg xxz spin ring in thermal equilibrium. *Physica A: Statistical Mechanics and its Applications*, 392(10):2607–2614, 2013.

[108] Florian Mintert, Marek Kuś, and Andreas Buchleitner. Concurrence of mixed bipartite quantum states in arbitrary dimensions. *Phys. Rev. Lett.*, 92:167902, Apr 2004.

[109] Kai Chen, Sergio Albeverio, and Shao-Ming Fei. Entanglement of formation of bipartite quantum states. *Phys. Rev. Lett.*, 95:210501, Nov 2005.

[110] Kai Chen, Sergio Albeverio, and Shao-Ming Fei. Concurrence of arbitrary dimensional bipartite quantum states. *Phys. Rev. Lett.*, 95:040504, Jul 2005.

[111] Heinz-Peter Breuer. Separability criteria and bounds for entanglement measures. *Journal of Physics A: Mathematical and General*, 39(38):11847, 2006.

[112] Yong-Cheng Ou, Heng Fan, and Shao-Ming Fei. Proper monogamy inequality for arbitrary pure quantum states. *Phys. Rev. A*, 78:012311, Jul 2008.

[113] Julio I. de Vicente. Lower bounds on concurrence and separability conditions. *Phys. Rev. A*, 75:052320, May 2007.

[114] Ming Li, Shao-Ming Fei, and Zhi-Xi Wang. A lower bound of concurrence for multipartite quantum states. *Journal of Physics A: Mathematical and Theoretical*, 42(14):145303, 2009.

[115] F El Ayachi and M El Baz. General classification of entanglement using machine learning. *arXiv preprint arXiv:2210.07711*, 2022.

[116] Leah Henderson and Vlatko Vedral. Classical, quantum and total correlations. *Journal of physics A: mathematical and general*, 34(35):6899, 2001.

[117] Mazhar Ali, A. R. P. Rau, and G. Alber. Quantum discord for two-qubit x states. *Phys. Rev. A*, 81:042105, 2010.

[118] Gou Shinkai, Toshiaki Hayashi, Takeshi Ota, and Toshimasa Fujisawa. Correlated coherent oscillations in coupled semiconductor charge qubits. *Physical review letters*, 103(5):056802, 2009.

[119] A. Einstein, B. Podolsky, and N. Rosen. Can quantum-mechanical description of physical reality be considered complete? *Phys. Rev.*, 47:777–780, 1935.

[120] Luigi Amico, Rosario Fazio, Andreas Osterloh, and Vlatko Vedral. Entanglement in many-body systems. *Reviews of modern physics*, 80(2):517, 2008.

[121] Leah Henderson and Vlatko Vedral. Classical, quantum and total correlations. *Journal of physics A: mathematical and general*, 34(35):6899, 2001.

[122] Wojciech H Zurek. Einselection and decoherence from an information theory perspective. *Annalen der Physik*, 9(11-12):855–864, 2000.

[123] Harold Ollivier and Wojciech H Zurek. Quantum discord: a measure of the quantumness of correlations. *Physical review letters*, 88(1):017901, 2001.

[124] Gerardo Adesso, Thomas R Bromley, and Marco Cianciaruso. Measures and applications of quantum correlations. *Journal of Physics A: Mathematical and Theoretical*, 49(47):473001, 2016.

[125] Animesh Datta, Anil Shaji, and Carlton M Caves. Quantum discord and the power of one qubit. *Physical review letters*, 100(5):050502, 2008.

[126] BP Lanyon, M Barbieri, MP Almeida, and AG White. Experimental quantum computing without entanglement. *Physical review letters*, 101(20):200501, 2008.

[127] MP Almeida, Mile Gu, Alessandro Fedrizzi, Matthew A Broome, Timothy C Ralph, and Andrew G White. Entanglement-free certification of entangling gates. *Physical Review A*, 89(4):042323, 2014.

[128] Stefano Pirandola. Quantum discord as a resource for quantum cryptography. *Scientific reports*, 4:6956, 2014.

[129] Indranil Chakrabarty, Pankaj Agrawal, and Arun K Pati. Quantum dissension: generalizing quantum discord for three-qubit states. *The European Physical Journal D*, 65(3):605–612, 2011.

[130] Malgorzata Okrasa and Zbigniew Walczak. Quantum discord and multipartite correlations. *EPL (Europhysics Letters)*, 96(6):60003, 2011.

[131] Laura Mazzola, Jyrki Piilo, and Sabrina Maniscalco. Sudden transition between classical and quantum decoherence. *Physical review letters*, 104(20):200401, 2010.

[132] Gian Luca Giorgi, Bruno Bellomo, Fernando Galve, and Roberta Zambrini. Genuine quantum and classical correlations in multipartite systems. *Physical review letters*, 107(19):190501, 2011.

[133] CC Rulli and MS Sarandy. Global quantum discord in multipartite systems. *Physical Review A*, 84(4):042109, 2011.

[134] Bruce E Kane. A silicon-based nuclear spin quantum computer. *nature*, 393(6681):133–137, 1998.

[135] Daniel Loss and David P DiVincenzo. Quantum computation with quantum dots. *Physical Review A*, 57(1):120, 1998.

[136] FF Fanchini, LK Castelano, and AO Caldeira. Entanglement versus quantum discord in two coupled double quantum dots. *New Journal of Physics*, 12(7):073009, 2010.

[137] Abhishek Mukherjee, Yumi Shim, and Joon Myong Song. Quantum dot as probe for disease diagnosis and monitoring. *Biotechnology journal*, 11(1):31–42, 2016.

[138] Wen-Hui Zhang, Wei Ma, and Yi-Tao Long. Redox-mediated indirect fluorescence immunoassay for the detection of disease biomarkers using dopamine-functionalized quantum dots. *Analytical chemistry*, 88(10):5131–5136, 2016.

[139] Sandra J Rosenthal, Jerry C Chang, Oleg Kovtun, James R McBride, and Ian D Tomlinson. Biocompatible quantum dots for biological applications. *Chemistry & biology*, 18(1):10–24, 2011.

[140] Tsuyoshi Yamamoto, Yu A Pashkin, Oleg Astafiev, Yasunobu Nakamura, and Jaw-Shen Tsai. Demonstration of conditional gate operation using superconducting charge qubits. *Nature*, 425(6961):941–944, 2003.

[141] Simon Fölling, Stefan Trotzky, Patrick Cheinet, Michael Feld, Robert Saers, Artur Widera, Torben Müller, and Immanuel Bloch. Direct observation of second-order atom tunnelling. *Nature*, 448(7157):1029–1032, 2007.

[142] Marco Anderlini, Patricia J Lee, Benjamin L Brown, Jennifer Sebby-Strabley, William D Phillips, and James V Porto. Controlled exchange interaction between pairs of neutral atoms in an optical lattice. *Nature*, 448(7152):452–456, 2007.

[143] Edward Brian Davies. Quantum theory of open systems. *(No Title)*, 1976.

[144] Stephen M Barnett and Stig Stenholm. Hazards of reservoir memory. *Physical Review A*, 64(3):033808, 2001.

[145] Laura Mazzola, E-M Laine, H-P Breuer, Sabrina Maniscalco, and Jyrki Piilo. Phenomenological memory-kernel master equations and time-dependent markovian processes. *Physical Review A*, 81(6):062120, 2010.

[146] Alireza Shabani and Daniel A Lidar. Completely positive post-markovian master equation via a measurement approach. *Physical Review A*, 71(2):020101, 2005.

[147] EM Laine, K Luoma, and J Piilo. Local-in-time master equations with memory effects: applicability and interpretation. *Journal of Physics B: Atomic, Molecular and Optical Physics*, 45(15):154004, 2012.

[148] Vittorio Gorini, Andrzej Kossakowski, and Ennackal Chandy George Sudarshan. Completely positive dynamical semigroups of n-level systems. *Journal of Mathematical Physics*, 17(5):821–825, 1976.

[149] Heinz-Peter Breuer, Elsi-Mari Laine, and Jyrki Piilo. Measure for the degree of non-markovian behavior of quantum processes in open systems. *Physical review letters*, 103(21):210401, 2009.

[150] Kristiaan De Greve, Leo Yu, Peter L McMahon, Jason S Pelc, Chandra M Natarajan, Na Young Kim, Eisuke Abe, Sebastian Maier, Christian Schneider, Martin Kamp, et al. Quantum-dot spin–photon entanglement via frequency downconversion to telecom wavelength. *Nature*, 491(7424):421–425, 2012.

[151] MV Rakhlin, KG Belyaev, GV Klimko, IS Mukhin, DA Kirilenko, TV Shubina, SV Ivanov, and AA Toropov. Inas/algaas quantum dots for single-photon emission in a red spectral range. *Scientific Reports*, 8(1):5299, 2018.

[152] Fabian Olbrich, Jonatan Höschele, Matthias Paul, Jan Kettler, Simone L Portalupi, Michael Jetter, and Peter Michler. Single-photon and polarization-entangled photon emission from inas quantum dots in the telecom c-band. In *Nanophotonics VII*, volume 10672, pages 51–57. SPIE, 2018.

[153] Gou Shinkai, Toshiaki Hayashi, Takeshi Ota, and Toshimasa Fujisawa. Correlated coherent oscillations in coupled semiconductor charge qubits. *Physical Review Letters*, 103(5):056802, 2009.

[154] Ahsan Nazir, Brendon W Lovett, Sean D Barrett, John H Reina, and G Andrew D Briggs. Anticrossings in förster coupled quantum dots. *Physical review B*, 71(4):045334, 2005.

[155] Gang Chen, NH Bonadeo, D Gammon Steel, † D Gammon, DS Katzer, D Park, and LJ Sham. Optically induced entanglement of excitons in a single quantum dot. *Science*, 289(5486):1906–1909, 2000.

[156] FF Fanchini, LK Castelano, and AO Caldeira. Entanglement versus quantum discord in two coupled double quantum dots. *New Journal of Physics*, 12(7):073009, 2010.

[157] Heinz-Peter Breuer, Francesco Petruccione, et al. *The theory of open quantum systems*. Oxford University Press on Demand, 2002.

[158] Nguyen Ba An, Jaewan Kim, and Kisik Kim. Nonperturbative analysis of entanglement dynamics and control for three qubits in a common lossy cavity. *Physical Review A*, 82(3):032316, 2010.

[159] Joao PG Pinto, Göktuğ Karpat, and Felipe F Fanchini. Sudden change of quantum discord for a system of two qubits. *Physical Review A*, 88(3):034304, 2013.

[160] K Nishibayashi, T Kawazoe, M Ohtsu, K Akahane, and N Yamamoto. Observation of interdot energy transfer between inas quantum dots. *Applied Physics Letters*, 93(4):042101, 2008.

[161] Chun-Hua Yuan, Ka-Di Zhu, and Xiao-Zhong Yuan. Exciton entanglement in coupled quantum dots in a microcavity. *Physical Review A*, 75(6):062309, 2007.

[162] Th Förster. Zwischenmolekulare energiewanderung und fluoreszenz. *Annalen der physik*, 437(1-2):55–75, 1948.

[163] Sonja Daffer, Krzysztof Wódkiewicz, James D Cresser, and John K McIver. Depolarizing channel as a completely positive map with memory. *Physical Review A*, 70(1):010304, 2004.

[164] Mazhar Ali. Dynamics of genuine multipartite entanglement under local non-markovian dephasing. *Physics Letters A*, 378(30-31):2048–2053, 2014.

[165] F Siyouri, M El Baz, S Rfifi, and Y Hassouni. Dynamics of super quantum correlations and quantum correlations for a system of three qubits. *Communications in Theoretical Physics*, 65(4):447, 2016.

[166] Mohammad Hasan Yavari, Vahid Ahmadi, and Peyman Rafiee. Modulation characteristics of self-assembled inas-gaas quantum dot laser considering phonon bottleneck, carrier relaxation and homogeneous broadening. In *2009 3rd ICTON Mediterranean Winter Conference (ICTON-MW)*, pages 1–4. IEEE, 2009.

[167] Julia Neuwirth, Francesco Basso Basset, Michele B Rota, Emanuele Roccia, Christian Schimpf, Klaus D Jöns, Armando Rastelli, and Rinaldo Trotta. Quantum dot technology for quantum repeaters: from entangled photon generation toward the integration with quantum memories. *Materials for Quantum Technology*, 1(4):043001, 2021.

[168] Polina O Anikeeva, Jonathan E Halpert, Moungi G Bawendi, and Vladimir Bulovic. Quantum dot light-emitting devices with electroluminescence tunable over the entire visible spectrum. *Nano letters*, 9(7):2532–2536, 2009.

[169] Tao Ding, Xuyong Yang, Lin Ke, Yanjun Liu, Wan-Yi Tan, Ning Wang, Xu-Hui Zhu, and Xiao Wei Sun. Improved quantum dot light-emitting diodes with a cathode interfacial layer. *Organic Electronics*, 32:89–93, 2016.

[170] Sofie Abe, Jonas J Joos, Lisa IDJ Martin, Zeger Hens, and Philippe F Smet. Hybrid remote quantum dot/powder phosphor designs for display backlights. *Light: Science & Applications*, 6(6):e16271–e16271, 2017.

[171] Geoffrey J Supran, Katherine W Song, Gyu Weon Hwang, Raoul E Correa, Jennifer Scherer, Eric A Dauler, Yasuhiro Shirasaki, Moungi G Bawendi, and Vladimir Bulović. High-performance shortwave-infrared light-emitting devices using core–shell (pbs–cds) colloidal quantum dots. *Advanced Materials*, 27(8):1437–1442, 2015.

[172] Sjoerd A Veldhuis, Pablo P Boix, Natalia Yantara, Mingjie Li, Tze Chien Sum, Nripan Mathews, and Subodh G Mhaisalkar. Perovskite materials for light-emitting diodes and lasers. *Advanced materials*, 28(32):6804–6834, 2016.

[173] Jizhong Song, Jianhai Li, Xiaoming Li, Leimeng Xu, Yuhui Dong, and Haibo Zeng. Quantum dot light-emitting diodes based on inorganic perovskite cesium lead halides (cspbx3). *Advanced materials*, 27(44):7162–7167, 2015.

[174] Xiwen Gong, Zhenyu Yang, Grant Walters, Riccardo Comin, Zhijun Ning, Eric Beauregard, Valerio Adinolfi, Oleksandr Voznyy, and Edward H Sargent. Highly efficient quantum dot near-infrared light-emitting diodes. *Nature Photonics*, 10(4):253–257, 2016.

[175] KWJ Barnham and G Duggan. A new approach to high-efficiency multi-band-gap solar cells. *Journal of Applied Physics*, 67(7):3490–3493, 1990.

[176] E H. Sargent. Infrared quantum dots. *Advanced Materials*, 17(5):515–522, 2005.

[177] Xinzheng Lan, Oleksandr Voznyy, Amirreza Kiani, F Pelayo García de Arquer, Abdullah Saud Abbas, Gi-Hwan Kim, Mengxia Liu, Zhenyu Yang, Grant Walters, Jixian Xu, et al. Passivation using molecular halides increases quantum dot solar cell performance. *Advanced Materials*, 28(2):299–304, 2016.

[178] Jun Pan, Ala'a O El-Ballouli, Lisa Rollny, Oleksandr Voznyy, Victor M Burlakov, Alain Goriely, Edward H Sargent, and Osman M Bakr. Automated synthesis of photovoltaic-quality colloidal quantum dots using separate nucleation and growth stages. *ACS nano*, 7(11):10158–10166, 2013.

[179] Chia-Hao M Chuang, Patrick R Brown, Vladimir Bulović, and Moungi G Bawendi. Improved performance and stability in quantum dot solar cells through band alignment engineering. *Nature materials*, 13(8):796–801, 2014.

[180] Ronnie Kosloff. Quantum thermodynamics: A dynamical viewpoint. *Entropy*, 15(6):2100–2128, 2013.

[181] Koji Maruyama, Franco Nori, and Vlatko Vedral. Colloquium: The physics of maxwell's demon and information. *Rev. Mod. Phys.*, 81:1–23, Jan 2009.

[182] Marlan O. Scully. Quantum photocell: Using quantum coherence to reduce radiative recombination and increase efficiency. *Phys. Rev. Lett.*, 104:207701, May 2010.

[183] Friedemann Tonner and Günter Mahler. Autonomous quantum thermodynamic machines. *Phys. Rev. E*, 72:066118, Dec 2005.

[184] Himangshu Prabal Goswami and Upendra Harbola. Thermodynamics of quantum heat engines. *Phys. Rev. A*, 88:013842, Jul 2013.

[185] A. E. Allahverdyan, R. Serral Gracià, and Th. M. Nieuwenhuizen. Work extraction in the spin-boson model. *Phys. Rev. E*, 71:046106, Apr 2005.

[186] Jianhui Wang, Zhaoqi Wu, and Jizhou He. Quantum otto engine of a two-level atom with single-mode fields. *Phys. Rev. E*, 85:041148, Apr 2012.

[187] Tien D. Kieu. The second law, maxwell's demon, and work derivable from quantum heat engines. *Phys. Rev. Lett.*, 93:140403, Sep 2004.

[188] H. T. Quan, Yu-xi Liu, C. P. Sun, and Franco Nori. Quantum thermodynamic cycles and quantum heat engines. *Phys. Rev. E*, 76:031105, Sep 2007.

[189] X. L. Huang, Tao Wang, and X. X. Yi. Effects of reservoir squeezing on quantum systems and work extraction. *Phys. Rev. E*, 86:051105, Nov 2012.

[190] Hao Wang, Sanqiu Liu, and Jizhou He. Thermal entanglement in two-atom cavity qed and the entangled quantum otto engine. *Phys. Rev. E*, 79:041113, Apr 2009.

[191] John E Shaw. Comparing carnot, stirling, otto, brayton and diesel cycles. *Transactions of the Missouri Academy of Science*, 42(2008):1–6, 2008.

[192] Tova Feldmann, Eitan Geva, Ronnie Kosloff, and Peter Salamon. Heat engines in finite time governed by master equations. *American Journal of Physics*, 64(4):485–492, 1996.

[193] Tova Feldmann and Ronnie Kosloff. Characteristics of the limit cycle of a reciprocating quantum heat engine. *Physical Review E*, 70(4):046110, 2004.

[194] Yair Rezek and Ronnie Kosloff. Irreversible performance of a quantum harmonic heat engine. *New Journal of Physics*, 8(5):83, 2006.

[195] Shadi A Dayeh, David PR Aplin, Xiaotian Zhou, Paul KL Yu, Edward T Yu, and Deli Wang. High electron mobility inas nanowire field-effect transistors. *small*, 3(2):326–332, 2007.

[196] Edward-Yi Chang, Chien-I Kuo, Heng-Tung Hsu, Che-Yang Chiang, and Yasuyuki Miyamoto. Inas thin-channel high-electron-mobility transistors with very high current-gain cutoff frequency for emerging submillimeter-wave applications. *Applied Physics Express*, 6(3):034001, 2013.

[197] S Massidda, A Continenza, AJ Freeman, TM De Pascale, F Meloni, and M Serra. Structural and electronic properties of narrow-band-gap semiconductors: Inp, inas, and insb. *Physical Review B*, 41(17):12079, 1990.

[198] Christopher Mittag, Jonne V Koski, Matija Karalic, Candice Thomas, Aymeric Tuaz, Anthony T Hatke, Geoffrey C Gardner, Michael J Manfra, Jeroen Danon, Thomas Ihn, et al. Few-electron single and double quantum dots in an in as two-dimensional electron gas. *PRX Quantum*, 2(1):010321, 2021.

[199] Michael Mozurkewich and R Stephen Berry. Optimal paths for thermodynamic systems: the ideal otto cycle. *Journal of Applied Physics*, 53(1):34–42, 1982.

[200] George Thomas and Ramandeep S Johal. Coupled quantum otto cycle. *Physical Review E*, 83(3):031135, 2011.

[201] Florian Ion Petrescu and Relly Victoria Petrescu. An otto engine dynamic model. *Independent Journal of Management & Production (IJM&P)*, 7(1), 2016.

[202] K Nishibayashi, T Kawazoe, M Ohtsu, K Akahane, and N Yamamoto. Observation of interdot energy transfer between inas quantum dots. *Applied Physics Letters*, 93(4):042101, 2008.

[203] Th Förster. Zwischenmolekulare energiewanderung und fluoreszenz. *Annalen der physik*, 437(1-2):55–75, 1948.

[204] Hai-Tao Quan, Yu-xi Liu, Chang-Pu Sun, and Franco Nori. Quantum thermodynamic cycles and quantum heat engines. *Physical Review E*, 76(3):031105, 2007.

[205] Tien D Kieu. The second law, maxwell's demon, and work derivable from quantum heat engines. *Physical review letters*, 93(14):140403, 2004.

[206] Max Born and Vladimir Fock. Beweis des adiabatensatzes. *Zeitschrift für Physik*, 51(3):165–180, 1928.

[207] A Messiah. Quantum mechanics, vol. 2, chapter 17, 1958.

[208] Lorenzo Buffoni, Andrea Solfanelli, Paola Verrucchi, Alessandro Cuccoli, and Michele Campisi. Quantum measurement cooling. *Physical review letters*, 122(7):070603, 2019.

[209] X. L. Huang, Tao Wang, and X. X. Yi. Effects of reservoir squeezing on quantum systems and work extraction. *Phys. Rev. E*, 86:051105, Nov 2012.

[210] Hao Wang, Sanqiu Liu, and Jizhou He. Thermal entanglement in two-atom cavity qed and the entangled quantum otto engine. *Phys. Rev. E*, 79:041113, Apr 2009.

[211] Ting Zhang, Wei-Tao Liu, Ping-Xing Chen, and Cheng-Zu Li. Four-level entangled quantum heat engines. *Physical Review A*, 75(6):062102, 2007.

[212] Karen V Hovhannisyan, Martí Perarnau-Llobet, Marcus Huber, and Antonio Acín. Entanglement generation is not necessary for optimal work extraction. *Physical review letters*, 111(24):240401, 2013.

[213] Nicolas Brunner, Marcus Huber, Noah Linden, Sandu Popescu, Ralph Silva, and Paul Skrzypczyk. Entanglement enhances cooling in microscopic quantum refrigerators. *Physical Review E*, 89(3):032115, 2014.

[214] Robert Alicki and Mark Fannes. Entanglement boost for extractable work from ensembles of quantum batteries. *Physical Review E*, 87(4):042123, 2013.

[215] William K. Wootters. Entanglement of formation of an arbitrary state of two qubits. *Phys. Rev. Lett.*, 80:2245–2248, Mar 1998.

[216] Ming Li, Shao-Ming Fei, and Zhi-Xi Wang. A lower bound of concurrence for multipartite quantum states. *Journal of Physics A: Mathematical and Theoretical*, 42(14):145303, 2009.

[217] Chun-Hua Yuan, Ka-Di Zhu, and Xiao-Zhong Yuan. Exciton entanglement in coupled quantum dots in a microcavity. *Physical Review A*, 75(6):062309, 2007.

[218] H Ait Mansour, FZ Siyouri, M Faqir, and M El Baz. Quantum correlations dynamics in two coupled semiconductor inas quantum dots. *Physica Scripta*, 95(9):095101, 2020.

***Résumé***

Dans cette thèse, nous nous concentrons sur l'étude de la dynamique des corrélations quantiques au sein de deux qubits excitoniques intégrés dans deux boîtes quantiques semi-conductrices InAs couplées, interagissant indépendamment avec des réservoirs de déphasage. Nous explorons leur comportement dans des environnements markoviens et non markoviens en fonction du temps et de la température. De plus, nous analysons les effets d'un champ électrique externe sur ces corrélations ainsi que les effets liés à l'interaction de Förster. Nous étudions aussi le comportement du discord quantique global et de l'intrication dans deux boîtes quantiques doubles couplées composées de AlGaAs/GaAs en fonction de la température. Nous étudions également le comportement du discord quantique global et de l'intrication dans deux boites quantiques doubles couplés composés de AlGaAs/GaAs en fonction de la température. Nous utilisons chaque pair de boites quantiques comme un qubit, où l'électron peut occuper soit la boite à droite, soit la boite à gauche. L'objectif de notre enquête est de comprendre l'impact du décalage énergétique de chaque qubit et de l'énergie de couplage tunnel sur les corrélations quantiques. Enfin, l'objectif est d'utiliser les trois boites quantiques InAs comme substance de travail d'un moteur thermique quantique, permettant au moteur de fonctionner à des échelles très réduites, en présence d'un champ électrique, et du mécanisme de Forster, qui décrit le transfert d'énergie entre les boites quantiques et affecte ainsi le comportement du moteur. À cet égard, nous étudions le comportement du travail effectué par le moteur et l'intrication dans le système lorsque le paramètre de Forster varie.
**Mots-clés:** Boites quantiques, Intrication quantique, Thermodynamique, machine thermique, Fonction de Wigner, Discorde.

***Abstract***

In this thesis, we focus our attention on investigating the dynamics of quantum correlations within two excitonic qubits embedded in two coupled semiconductor InAs quantum dots independently interacting with dephasing reservoirs. Their behavior in both Markovian and non-Markovian environments is explored against dimensionless time and temperature. Moreover, the effects of the external electric field on these correlations as well as the effects related to the Förster interaction are extensively analyzed. Also, we will study the behavior of global quantum discord and entanglement in two coupled double quantum dots made of AlGaAs/GaAs as a function of temperature. We use each double quantum dot as a qubit, where the electron can occupy either the right or left dot. The goal of our investigation is to understand the impact of the energy offset of each qubit and the tunneling coupling energy on quantum correlations. Finally, is to use the three InAs quantum dots as a working substance of a quantum heat engine, which allows the engine to operate at very small scales, in the presence of an electric field, and the Forster mechanism, which describes the transfer of energy between quantum dots and affects thus the engine's behavior. In this regard, we study the behavior of the work performed by the engine and the entanglement in the system as the Forster parameter is varied.
**Keywords:** Quantum Dots, Quantum Entanglement, Thermodynamics, Heat Engines, Wigner Function, Discord.